SPIN DEPENDENT TRANSPORT STUDIES IN MAGNETIC, NON-MAGNETIC, ANTIFERROMAGNETIC, AND HALF METALS.

By

Rakhi Acharyya

A DISSERTATION

Submitted to
Michigan State University
in partial fulfillment of the requirements
for the degree of

DOCTOR OF PHILOSOPHY

Physics

2012

ABSTRACT

SPIN DEPENDENT TRANSPORT STUDIES IN MAGNETIC, NON-MAGNETIC, ANTIFERROMAGNETIC, AND HALF METALS.

By

Rakhi Acharyya

This thesis consists of three studies of Current-Perpendicular-to-the-Planes (CPP) Magnetoresistance (MR) of sputtered ferromagnetic/non-magnetic (F/N) multilayers. (a) The first study involves a double-blind comparison of our measurements of the interface specific resistance AR (area A through which the CPP current flows times the CPP resistance R) of Pd/Ir interfaces with no-free-parameter calculations. (b) The second study is of spin-relaxation within the antiferromagnets (AF) IrMn and FeMn and at their interfaces with Cu. (c) The third study is of the MR of multilayers involving a nominal half-metal Heusler alloy, $Co_2Fe(Al_{0.5}Si_{0.5})$ (CFAS). A true half-metal should give an especially large CPP-MR. This study involves a different sample geometry, combining optical lithography and ion-beam etching, with epitaxial sputtering at elevated temperatures.

(a) For four pairs of lattice-matched metals (Ag/Au, Co/Cu, Fe/Cr, and Pt/Pd) having the same crystal structure and the same lattice parameter to within $\sim 1\%$, no-free-parameter calculations of 2AR, twice the interface specific resistance AR have agreed with measured values to within mutual uncertainties. For three pairs, the measured values were known when the calculations were made. For the fourth pair, Pt/Pd, they were not. In contrast, calculations for non-matched pairs, where the lattice parameters differed by 5% or more, disagreed with measured values. In this thesis we study a fifth pair, Pd and Ir, where the lattice parameter mismatch is intermediate, 1.3%. The project was done double-blind with theory

collaborators Wang and Xia, with experiment and calculations shared only after both groups settled on their separate values. The values for Pd/Ir calculated with the same assumptions used previously were just outside of uncertainty of the measured ones. An improved calculation gave agreement between the two values.

(b) Antiferromagnets (AFs) play important roles in CPP-MR devices as sources of pinning for F-layers in exchange-biased spin-valves (EBSVs), and are also part of a burgeoning field of AF spintronics. For both structures, it is important to understand spin-relaxation within sputtered AFs and at AF/N interfaces. A prior study of spin-relaxation in sputtered FeMn found strong spin-flipping at FeMn/Cu interfaces, but was unable to determine the size of spin-flipping within the FeMn itself. In this thesis we find strong spin-flipping at IrMn/Cu interfaces and confirm strong spin-flipping at FeMn/Cu interfaces. We also discovered an interesting new phenomenon, a weak magnetic dependence of AR in Py, that makes us unable to put a tight bound on the bulk spin-diffusion lengths in sputtered IrMn or FeMn. But these lengths are probably short.

(c) The CPP-MR of an F/N multilayer will be enhanced by an F-metal with high spin-scattering asymmetry, making such a multilayer more competitive for devices. Half-metallic ferromagnetic metals, such as Heusler alloys, are predicted to have high asymmetry. Experiments with the Heusler alloy CFAS have shown both large Tunneling Magnetoresistance (TMR) and large CPP-MR for multilayers with non-superconducting electrodes sputtered at room temperature and then post-annealed to 500^0C. In this thesis we attempt to optimize epitaxial growth using high temperature sputtering to produce highly ordered Heusler alloys grown on superconducting electrodes. We are able to grow CFAS epitaxially, but have obtained maximum CPP MR only about one-third (40%) as large as we expected.

To
Ma, Baba, Dada, Mou, Dido, Pochi
Eric, Divya, Sharmistha, Arunima
Susmita and Sayak
For Being There For Me Always.

ACKNOWLEDGMENTS

I would like to acknowledge the individuals who supported me in my research at Michigan State University. I would like to start with my advisers, Prof. Jack Bass and Prof. William P. Pratt Jr. whose incredible guidance and support provided me with the right tools to complete this dissertation.

I would like to extend special thanks to Dr. Reza Loloee for training and helping me out in experiments using the sputtering system and other equipment, and lending advice from his years of experience with metal growth and characterization. His support and help has been a crucial ingredient in the completion of this dissertation.

I would like to thank Dr. Baokang Bi for training and advice with Keck Microfabrication Facility equipment.

My special thanks to Dr. Hoang Yen Nguyen who has made numerous difficult situations easier with her support. I would like to thank my collaborators, Dr.Xia and Dr.Wang at Beijing University and NSF and Seagate for funding my research.

Last but not the least, I would like to thank my friends and colleagues, in and outside MSU, and my family for making this difficult and challenging journey a wonderful experience.

TABLE OF CONTENTS

LIST OF TABLES

LIST OF FIGURES

Chapter 1

Introduction

1.1 Introduction and Overview

For decades, semiconductor devices have been an integral part of the Information Technology (IT) industry. Electron transport in standard semiconducting devices, based on only the electron charge, is conventionally known as Electronics. Now there is great interest in devices based upon both the electron's charge and its magnetic moment (spin). The study of electron transport based on both electron charge and electron spin is called Spintronics, an acronym for Spin Transfer Electronics. Spintronics, which is the basis of the present thesis, involves transport of conduction electrons through samples containing ferromagnetic (F) metals. Below a characteristic Curie Temperature, F-metals become magnetically ordered, i.e., once magnetized by an external field, they stay magnetized when the field is removed. In 1936, Mott proposed that electrons passing through an F-metal become spin-polarized. This spin polarization arises from asymmetric scattering of the electrons, depending on the relative orientation of their magnetic moment (spin) and that of the F-metal. Scattering is

usually strongest when the electron moment is anti-parallel to the F-moment, and weakest when it is parallel[1].

The genesis of the Spintronics revolution came in 1988, when Fert [2] and Grunberg [3] discovered, independently, that the resistances of Fe/Cr multilayers with Cr thicknesses chosen to give antiferromagnetic coupling between adjacent Fe layers, decreased substantially at both room temperature and 4.2K as a magnetic field was increased to overcome the antiferromagnetic coupling. The largest reduction, 50% at 4.2K, led to the name "Giant" Magnetoresistance (GMR). Figure 1.1 shows a schematic of R(H) as seen in [2], where the resistance of the as-grown antiferromagnetically coupled F layers, in the Antiparallel (AP) state, is highest. An applied field that overcomes the antiferromagnetic coupling of the F layers gives a parallel (P) state. For both this discovery, and the relatively rapid development of large scale uses of GMR multilayers for devices, Grunberg and Fert shared the 2007 Nobel Prize.

The GMR that Fert and Grunberg discovered, and that rapidly led to device development, is called the CIP-MR,i.e.,MR with Current-flow In the layer Planes (CIP). The overall resistance of CIP samples is $\sim$ Ohms since their lateral dimensions are much larger than their thicknesses. Thus, CIP measurements are easily made with standard voltmeters, and CIP-MR is easily incorporated into devices. However the current-density in the CIP-MR is not uniform, flowing more strongly in the layer with lower resistance. This non-uniformity makes it difficult to separate contributions from individual layers and interfaces. In 1991, Zhang and Levy [4] predicted that the MR could be considerably larger if the current flows perpendicular to the plane of the layers (CPP geometry) (See Figure 1.2). In the same year, Pratt et al [5] showed that the CPP-MR of Co/Ag multilayers was indeed much larger at

4.2K than the CIP-MR [5] (Figure 1.3). However, the CPP resistance (R) ($\sim 10^{-8}\Omega$) of a multilayer with standard CIP dimensions is much smaller than the CIP resistance ($\sim \Omega$), as the CPP thickness ($t\sim$nm) is much smaller than the corresponding width ($w\sim$mm) and length (l ~mm). Measuring the CPP-R thus requires a sophisticated measuring technique (Section 3.3.1). In addition to often yielding a larger MR than the CIP MR, a proper CPP geometry yields a uniform current density across the area A through which the current flows, which leads to the ability to separate bulk from interfacial contributions to both R and the CPP-MR, and thereby clarify the physics underlying GMR. The intrinsic property of the samples measured is the Specific Resistance AR= Area(A) times Resistance(R), where A($=l \times w$) is the area through which CPP current flows.

This thesis describes three projects intended to provide new information on CPP transport properties of (a) non-magnetic interfaces; (b) antiferromagnetic alloys; and (c) an epitaxial, nominal half metallic, alloy.

Chapter 1 is divided into the following Sections:

1.2 History of Magnetoresistance and its Applications: We provide a brief history of the relevant developments in the past years in the field of Spintronics.

1.3 Spin Dependent Transport: We describe a simple model for the essential part of Spintronics, ie, asymmetric conduction by electrons in F metals based on their spin.

1.4 Basic idea of GMR.

1.5 Sample geometries for Current Perpendicular to Plane Resistance (CPP R).

1.6 Control of Magnetic Ordering: We describe the experimental ways to control P and AP states.

1.7 Finally, we briefly describe the projects in this thesis.

1.2 History of Magnetoresistance and Applications

The study of electrical transport in F-metals has a long history [7]. In 1856, Lord Kelvin discovered that the resistance of a ferromagnetic metal changed as the angle between the applied field and the flowing current was changed. This effect is known as Anisotropic Magnetoresistance (AMR). AMR yielded a change of about 2% in Permalloy (Py) at room temperature and small fields, sufficient to lead to the use of Py films for the read heads in computer hard drives introduced in 1991 by IBM [8] [9]. In the 1960s, studies on N/F′/N junctions, where F′ is a ferromagnetic semiconductor and N is a non-magnet, showed that the I-V curves were affected by an applied magnetic field [10][11][12]. Experiments on F/I/S junctions, where I is an insulator and S a superconductor, done by Tedrow and Meservey in the 1970s [13], showed that current gets spin polarized upon passing through the F layer and remains so through the insulator. In 1975, Julliére [14] showed small magnetoresistive effects in F/I/F trilayers. Based on his results, plus the prior ones on F/I/S trilayers, he proposed a model for Tunnel Magnetoresistance (TMR). Julliére's model for TMR introduced the basic spin valve effect, in which the resistance of a device depends on the relative orientation of magnetizations of two F layers separated by a spacer layer [15].

The development in the early 1990s of metal pairs with characteristics better than Fe/Cr, led to CIP-MRs of several percent at room temperature. These were large enough so that, in 1997, IBM replaced AMR read heads with CIP-MR ones. CIP-MR also became used in the automotive industry and in medicine [16]. In 2005, CIP-MR read heads were replaced by

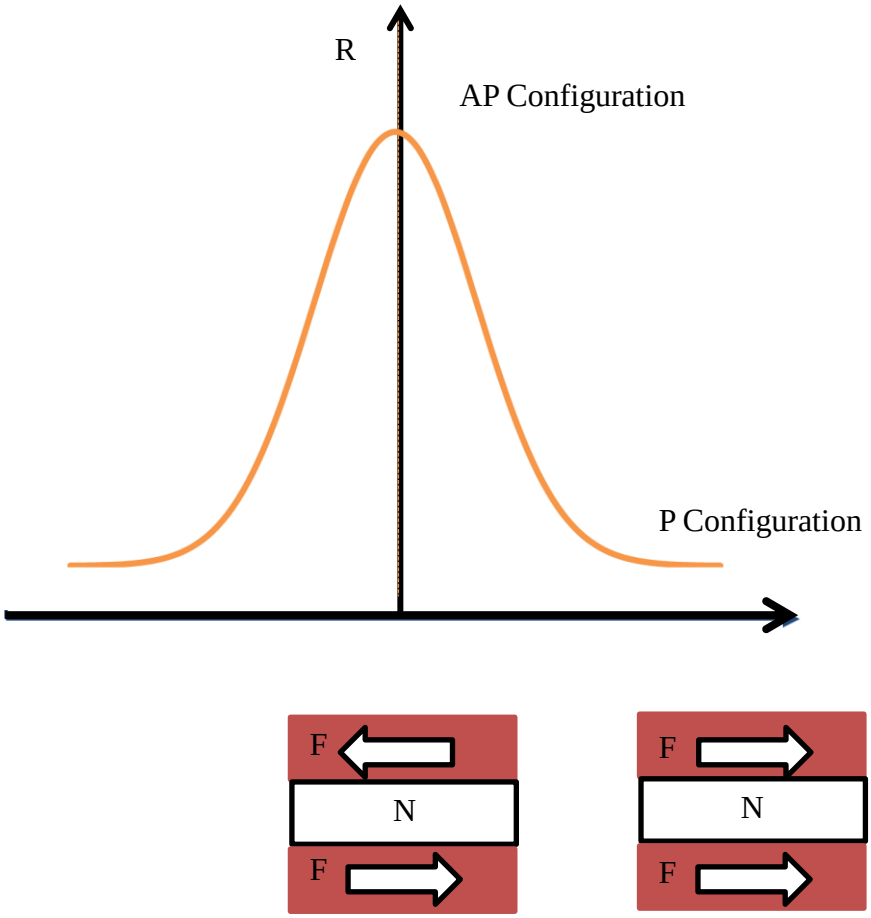

Figure 1.1: Schematic of the resistance R versus magnetic field H of an antiferromagnetically coupled Fe/Cr/Fe trilayer [After [6]]. In the as-prepared state, the magnetizations of the F layers are antiparallel to each other. The resistance drops from R(AP) to R(P). For interpretation of the references to color in this and all other figures, the reader is referred to the electronic version of this dissertation.

MgO based TMR devices by Seagate. TMR has allowed disk drive densities of 500GB/in^2. Present research in spintronics aims to achieve read heads to enable disk drive density exceeding 1TB/in^2. CPP-MR is one of the competitors for such next generation read heads [17].

GMR provides large magnetoresistive effects. In 1996, Spintronics saw the development of a complimentary phenomenon, called Spin Transfer Torque (STT), which allows the use of spin-polarized currents to manipulate the magnetizations of F-metal layers. STT was predicted by Berger [18] and Slonzcewski [19] and discovered by Tsoi et al. [20]. It is already being used in TMR-based Random Access Memory, providing scalability and low power consumption.

1.3 Spin Dependent Transport

Ferromagnetic metals are an integral part of the field of spintronics as they provide a medium to distinguish the transport of electrons based on the electron spin. F metals have an inherent property to scatter electrons asymmetrically based on the orientation of the electron spins with respect to the F magnetizations. This asymmetry gives rise to a polarization of the electron current transiting through a F metal. In this section we describe the model proposed by Mott to describe the origin of the spin dependent transport through a F metal [21][22][23].

Electrons have a spin quantum number $s = \frac{1}{2}$. The projection of the electron spin onto a chosen quantization axis is given by $s_z = \pm\frac{1}{2}$ with $s_z = +\frac{1}{2}$ representing a spin up state and $s_z = -\frac{1}{2}$ representing a spin down state. An electron with spin quantum number s has

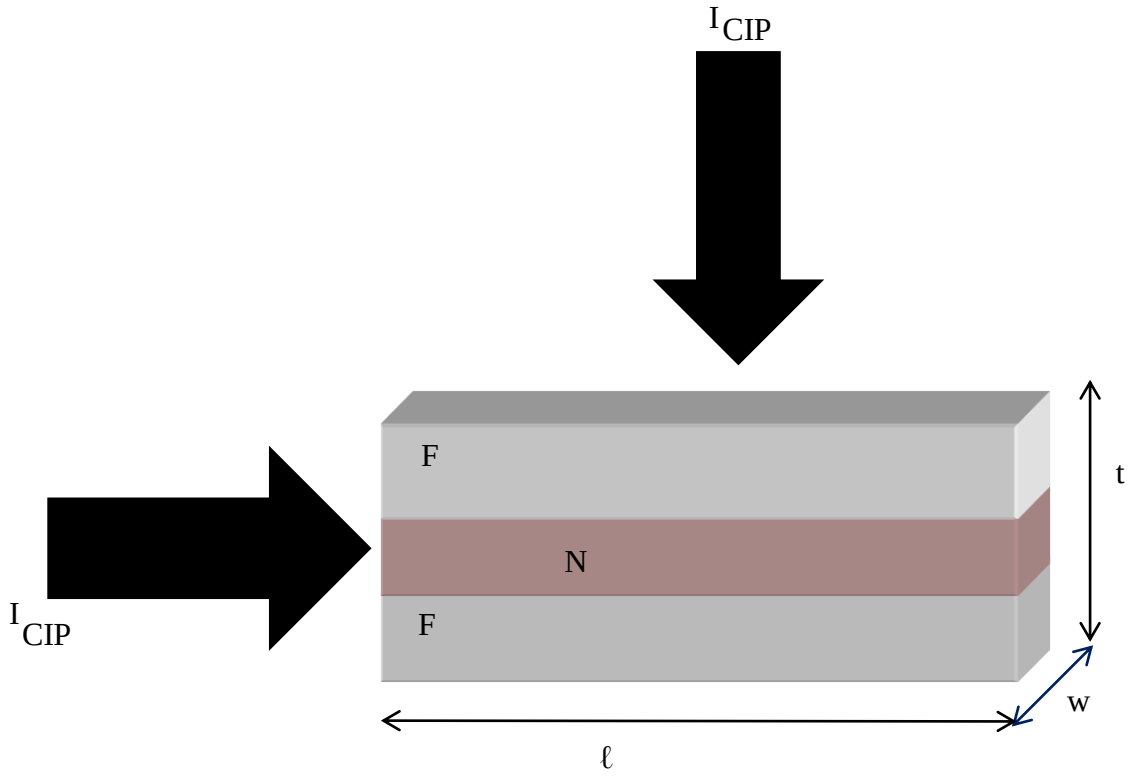

Figure 1.2: Current directions in a F/N/F trilayer. I_{CPP} flows perpendicular to the layers. I_{CIP} flows in the plane of the layers.

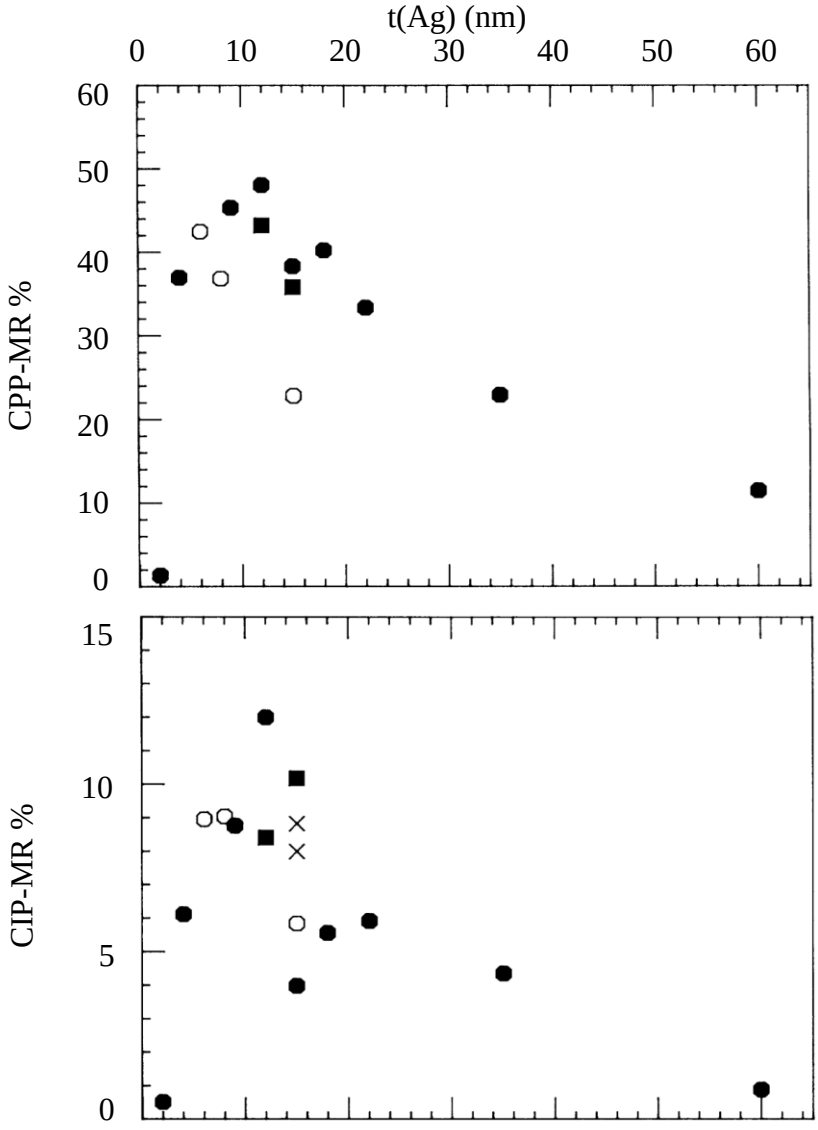

Figure 1.3: Comparison of CIP to CPP MR versus t_{Ag}(nm) for Co/Ag. Open circles are for equal thicknesses of Co/Ag multilayers. Filled circles and crosses are for Co(6nm)/Ag(t_{Ag}nm) multilayers [5].

a spin magnetic moment m_z given by

$$< m_z >= -(\frac{e}{2m_e})g < s_z > \tag{1.1}$$

$< m_z >$ and $< s_z >$ are the expectation values of the spin magnetic moment and the spin projection state. For an electron, g$\sim$2 and e and m_e are the electron charge and mass respectively. The spin magnetic moment is related to the spin state with a minus sign that implies that the spin magnetic moment is aligned opposite to the spin state. The spin state up is the same as a spin moment down and spin state down is the same as spin moment up. The focus in this thesis will be on the spin magnetic moment and not the spin state, unless mentioned otherwise.

Ferromagnetic behavior is found in transition metals with partially filled d atomic orbitals. In an isolated atom, the order of filling of atomic orbitals is set by Hund's rule. Hund's rule states that electrons in an isolated atom are partially filled in atomic orbitals to get the maximum spin moment (all electrons first filled with spins in same direction, followed by filling with spins in the opposite direction) and the gain in energy from such an arrangement is driven by the Pauli Exclusion Principle. The exclusion principle keeps electrons with the same spin farther apart, thereby reducing the Coulomb repulsion between them. The gain in energy by such an arrangement of electrons is called exchange energy. Each unpaired electron contributes a magnetic moment m_z. The magnetic moment of an isolated atom also includes a contribution from its orbital angular moment.

Unlike isolated atoms, in solids, hybridization between neighboring electron states occurs and leads to the formation of bands. Band formation leads to a reduction in orbital magnetic

moment by breaking the spherical symmetry around each atom. It also works against partial filling of atomic orbitals. Formation of bands makes putting unpaired electrons from lower filled bands to higher unfilled bands energetically unfavorable. Therefore band formation makes spin polarization, which is the degree to which the spins of electrons are aligned in one direction, unfavorable in most solids. Hence most solids are not ferromagnetic. In F metals, however, the d bands for spin moment up and spin moment down electrons are split. The reason for a split is that the gain in exchange energy by aligning electrons in one direction is high even in the presence of strong hybridization and band formation. Such a gain in energy is achieved by shifting of spin moment up electron bands down with respect to the spin moment down electron bands. Therefore, in F metals, spin polarization is favored as compared to an N metal. The magnitude of the shift is equal to the gain in exchange energy.

In Section 1.3.1, we present a widely used model for describing scattering asymmetry in electron transport in F metals, the Mott s-d model. The model assumes that the conducting electrons conserve their spin direction, i.e., no spin flipping occurs while the electrons transit an F metal. Mott's model is simplistic and real band calculations for transition metals using Local Spin Density Approximation (LSDA) give more complicated band structures [Refer to Figure 4 in [21]]. However Mott's model is useful to qualitatively understand the nature of spin polarization and differential spin scattering in ferromagnetic metals, which forms the basis for MR studies.

As a convention for this thesis, a conducting electron with spin moment parallel to the local ferromagnetic magnetization is referred to as a $\uparrow$ (majority electron) and an electron with spin moment antiparallel to the local F magnetization as $\downarrow$(minority electron), as shown in Figure 1.4.

1.3.1 Mott's s-d model

In 1936, Mott[24] proposed an s-d model to describe the asymmetric scattering of conduction electrons at the Fermi energy (E_F). In his model, conduction at E_F occurs due to both s and d bands. The dominant current carrier at E_F are the highly mobile s electrons. The effective mass of the s electrons is approximately the free electron mass. Therefore the Bloch waves corresponding to s electrons can be approximated to be plane waves. In contrast, the d electrons propagate in the lattice as Bloch waves, localized near the atoms (Itinerant Model [23]). The localization results in an effective mass of d electrons higher than the free electron mass. Therefore mobility of electrons in the d states is lower than mobility of electrons in the s band. The net conduction in this model is given as the sum of the s and d electron conductivities.

The probability of scattering of electrons at E_F is proportional to the Density of States, $D(E_F)$, available for the electrons to be scattered into at E_F. The electrons obey spin selectivity, i.e., the spin moment of electrons is conserved during a scattering event between two states. The density of states ($D_d(E_F)$),available in the d band at E_F for the minority s electrons, is higher than the density of states available in the d band at E_F for the majority s electrons, to scatter into. More available $D_d(E_F)$ leads to a larger probability of minority s electrons to scatter into the d states and so on. Larger scattering probability leads to reduced conduction. Therefore the overall conduction of the minority electrons is reduced

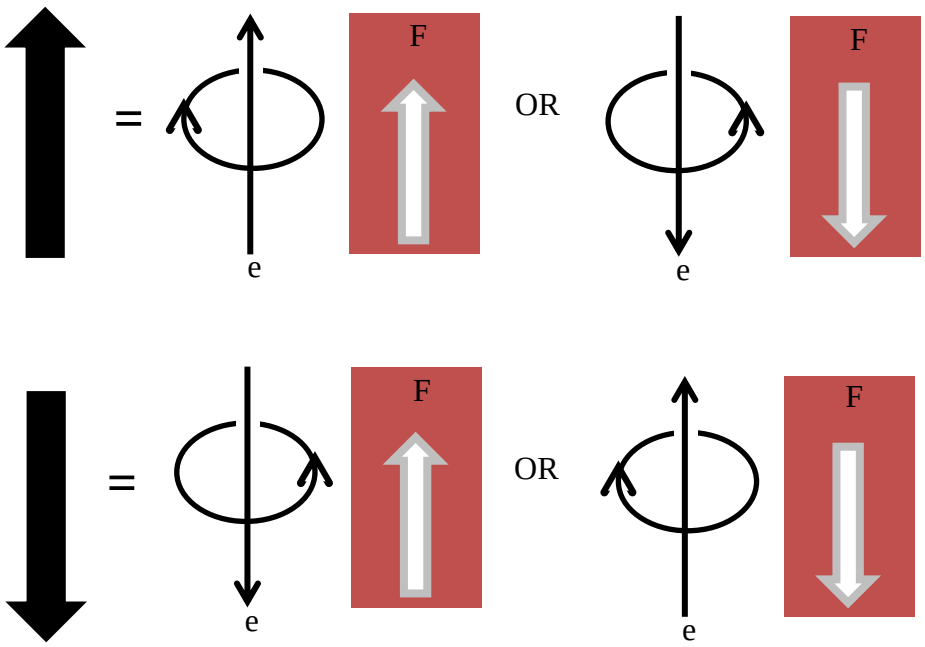

Figure 1.4: Up and Down arrows on the left hand side indicate the convention used in this thesis. Up arrow shows the majority electrons,ie the case when the electron moment is parallel to the local F magnetization. Down arrow shows the minority electrons,ie the case when electron moment is antiparallel to the local F magnetization.

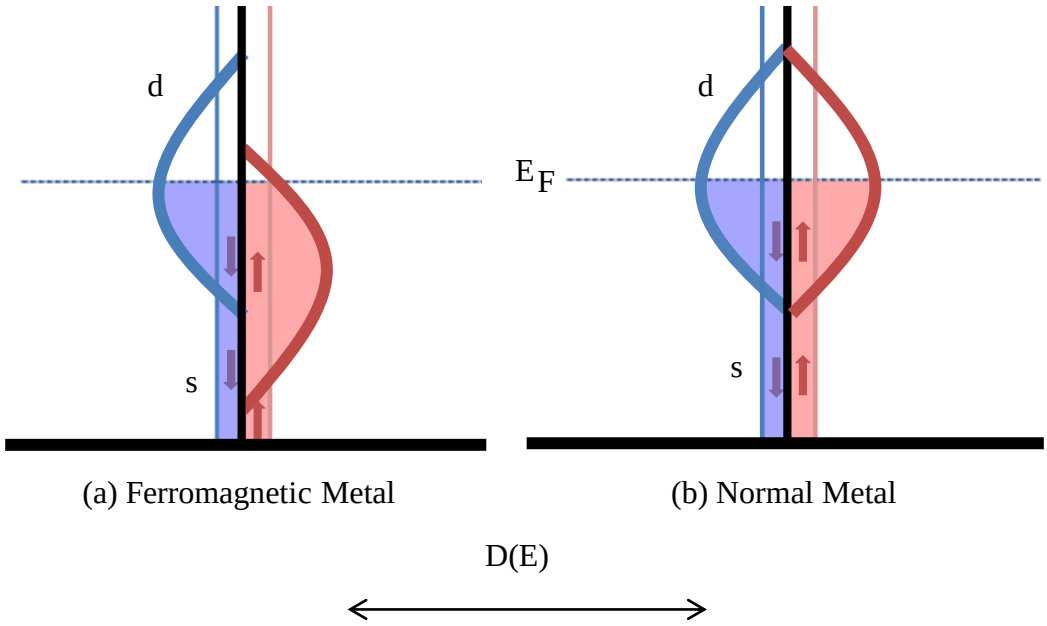

Figure 1.5: Schematic diagram of s and d bands at the Fermi energy E_F, for (a) Ferromagnet (F) metal where the d band density of states,$D_d(E_F)$, available for minority electrons is more than $D_d(E_F)$ available for majority electrons, at the Fermi Energy. Minority s electrons have more sluggish d band states to scatter into than majority s electrons have at E_F. Consequently $\rho_F^{\downarrow} > \rho_F^{\uparrow}$. (b) Normal (N) metal where the $D_d(E_F)$ for majority electrons is the same as $D_d(E_F)$ for minority electrons at E_F. Consequently $\rho_N^{\uparrow} = \rho_N^{\downarrow}$.

due to the scattering events. On the other hand, the scattering probability of the majority s electrons into d states is not high due to the presence of very few available $D_d(E_F)$ to scatter into. Therefore the conduction of majority electrons is higher than the conduction of minority electrons.

Figure 1.5a shows a schematic representation of the s and d bands in an F metal. At E_F, the d band states available for spin moment down electrons is higher than the d band states for spin moment up electrons. Given the spin selectivity of scattering, the current flow at the Fermi energy for the two spin states occurs in parallel. From Figure 1.5a we see that $\rho_F^{\uparrow} < \rho_F^{\downarrow}$ where the $\uparrow$ represents spin moment up and $\downarrow$ represents spin moment down. As an aid to clarity, the nature of the bands for a Normal metal is also shown (See Figure 1.5b). In an N metal, the density of states available in the d band is the same for both up and down moment electrons. Therefore $\rho_N^{\uparrow} = \rho_N^{\downarrow}$.

Experimental evidence for spin polarized transport was provided in the 1970s and 1980s by Deviations from Mathiessens Rule (DMR) studies collected in Campbell and Fert [25]. They collected the residual resistivities per atomic percent impurity based upon Ni,Co, and Fe ternary and binary alloys for a wide range of impurities, and as a function of temperature. From these, they were able to determine different effective residual resistivities of dilute ferromagnetic alloys for spin up and spin down electrons, indicating a scattering asymmetry for minority and majority electrons in F metals.

1.4 Basic Idea of GMR

Having explored the origin of scattering asymmetry, based on spin of conducting electrons transiting an F metal, we turn to Fert's simple model for GMR [2]. Consider an F/N/F trilayer or an $[F/N]_n$ multilayer. GMR is the change of resistance when the relative orientation of the magnetizations of adjacent F layers, separated by an N spacer layer, changes. The maximum and the best defined GMR is obtained in the limiting case when the relative F magnetizations are collinear and change from parallel (P) to antiparallel (AP). In the simplest model, assuming no spin flipping, a current scattered in the first F layer and at the F/N interface becomes spin polarized due to asymmetric scattering of majority and minority electrons. Figure 1.6 shows two cases based on the collinear magnetizations in adjacent F layers. They are:

- **AP Magnetization state:**The $\uparrow$ electrons scatter weakly in the first F layer but strongly in the second F layer, while the $\downarrow$ electrons scatter strongly in the first F layer, but weakly in the second F layer. The total resistance is the parallel combination of $\uparrow$ and $\downarrow$ electron resistances of the sample.

- **P Magnetization state:**The $\downarrow$ electrons scatter strongly in both layers. In contrast, the $\uparrow$ electrons scatter weakly in both F layers, thereby shorting the sample.

As a result the total resistance in the *parallel* (P) case is lower than in the *antiparallel* (AP) case.

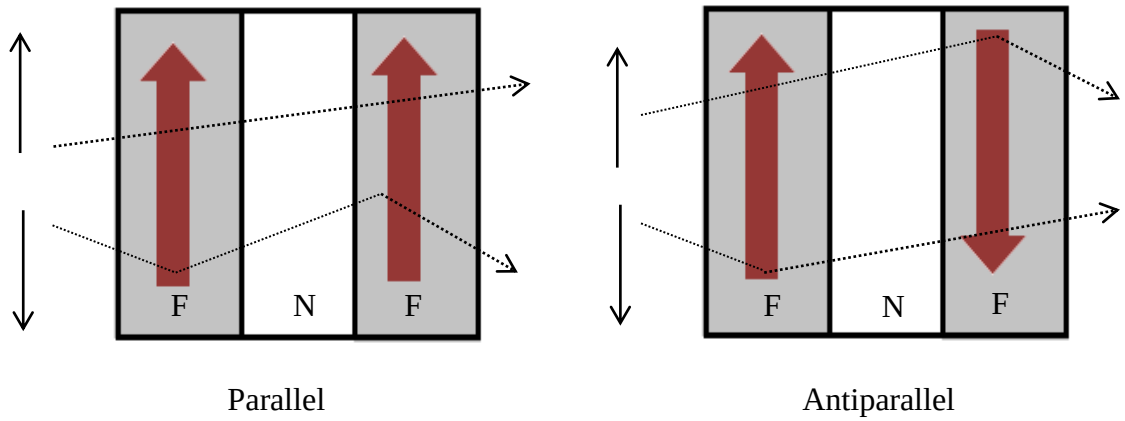

Figure 1.6: In the AP state, ↑ and ↓ electrons get scattered strongly in the second F layer and first F layer, respectively. In the P state, ↑ electrons short the sample while ↓ electrons get scattered strongly in both F layers. Total R(AP)>R(P).

Magnetoresistance (MR) is defined as,

$$MR\% = \frac{(AR(AP) - AR(P))}{(AR(P))} X100 \tag{1.2}$$

1.5 Current Perpendicular to Plane (CPP) Resistance

This thesis is a study of transport properties of metallic multilayers with current flow in the CPP direction. CPP transport data are usually analyzed using a model proposed by Valet and Fert (VF)[27] (Section 2.2), which is based on the Boltzmann formalism. Experimentalists use three different kinds of sample structures to fulfil the requirements of CPP sample

geometry. The important requirement of each sample structure is that the current flowing through the sample should be uniform, allowing a one dimensional theoretical model. We will review the three CPP sample structure designs here.

They are:

1) **Superconducting Cross Strips (CPP S):** This is the sample structure used in this thesis. CPP S involves thin film metals of thickness (t) much shorter than the width (w) of the layers, with Nb superconducting cross strips as electrodes on either side of the layers (See Figure 1.7a). There are many advantages of this sample structure that makes it especially desirable for our use.

   They are:

   a) The superconducting Nb provides an equipotential surface for current to flow uniformly through the sample.

   b) The superconducting Nb does not contribute any finite lead resistance. The only contribution is from the interface resistance of superconducting Nb with adjacent F layers, which can be determined from independent studies [28]. Therefore the measured resistances contain only the sample resistance and an additional known Nb/F interface resistance.

   c) The CPP S method for sample preparation is also suitable to make arbitrary combinations of F, N, and antiferromagnetic (AF) layers.

   d) The sample thickness $t \ll w$, minimizing current fringing around the edges of the sample($\sim 0.4\%$) [29] [30].

e) The sample area A can be measured independently.

There are however some disadvantages of using the CPP S sample structure:

a) The CPP resistance measurements are restricted to low temperatures (<transition T of the superconducting electrodes) to obtain current uniformity.

b) CPP S samples require sophisticated resistance measurement techniques to measure the ultra low sample resistance $\backsim 10^{-8}\Omega$ (See Chapter 2) since the lateral dimensions of the sample $\gg$ sample thickness.

2) **Nanowire Multilayer (CPP NW/ML):** In CPP NW/ML [31], the sample widths (w) are much smaller than their lengths (t) (See Figure 1.7b). The advantages of the CPP NW sample structure are:

a) The sample dimensions ensure that the current flowing through the sample is uniform.

b) Since the sample area is very small (the sample length is much greater than its lateral dimension), the resistances are of the order of $\backsim \Omega$ and much larger than the lead resistances.

c) Resistance can be measured using standard measurement techniques at room temperature.

d) It is also convenient to measure the temperature dependence of CPP MR.

There are however some disadvantages in this sample structure.

a) Nanowire fabrication involves electrodeposition of metals within nanosized pores in polycarbon or sapphire substrates. Usually a single electrolytic bath is used to deposit

two metals (F and N) by switching between their deposition potentials, which limits the combination of multiple different F and N metals. Use of multiple baths has been reported [32] but the fabrication process is complicated and subject to contamination.

b) Transport properties are usually measured on arrays of nanowires, as the high density of pores makes it difficult to isolate the resistance of a single nanowire which makes it difficult to determine A and only the fractional change in resistance ($\Delta R/R$) is measured for CPP MR.

3) **Micro- and Nano-pillar (CPP P):** In CPP P, the lengths are of the same order as the widths (Figure 1.7c). For use in practical devices, CPP P is the most convenient of the three sample structures in spite of the fabrication process involving multiple steps of lithography and Argon ion etching.

The advantages of the CPP P sample structure are:

a) The resistance of a CPP P sample is of the order of fractions of Ω because of the sample dimensions. Therefore it is convenient for room temperature measurements.

b) It is convenient to measure the temperature dependence of CPP MR.

c) Sample area is well defined through lithography.

d) The CPP P method for sample preparation is suitable to make arbitrary combinations of F, N, and antiferromagnetic (AF) layers.

However the disadvantages are that the current through the sample may not be uniform. Uniformity can be approximated only when the sheet resistance, ρ/t, of the extended leads is much smaller than the R of the nanopillar. The finite lead resistance may also

be comparable to the sample resistance R and not easily determined. Such sample structures require state of the art electron beam lithography techniques to make pillars with dimensions $\leq$ 100nm.

1.6 Control of Magnetic Ordering

Since the basic phenomenon of GMR is the change in resistance of a F/N/F trilayer or F/N multilayer when the relative orientations of adjacent F layer magnetizations change from P to AP, we need to be able to control the magnetic ordering in the F layers. The P state is easily achieved with the application of a large magnetic field in the plane of the layers. The main challenge in GMR devices is to obtain the AP state. In our CPP sample geometry Section 1.5, the sample widths are much larger than the sample thicknesses so that demagnetization effects drive the magnetizations to lie in the plane of the layers.

There are three main methods to control the magnetic ordering of the F layers.

1) **Antiferromagnetically coupled $[\mathbf{F/N}]_n$ multilayers:** Such samples were used to discover GMR. As-prepared samples have the magnetizations in adjacent F layers antiparallel to each other. On application of a large magnetic field, the magnetizations become parallel to each other. However Antiferromagnetically coupled F/N/F layers require large magnetic fields to align the magnetizations in the F layers parallel to each other, and only $\backsim$two N-thicknesses give an AP state. For practical purposes, these requirements limit its use.

2) **Uncoupled $[\mathbf{F/N}]_n$ multilayers:** For F/N multilayers with fixed F thickness and vari-

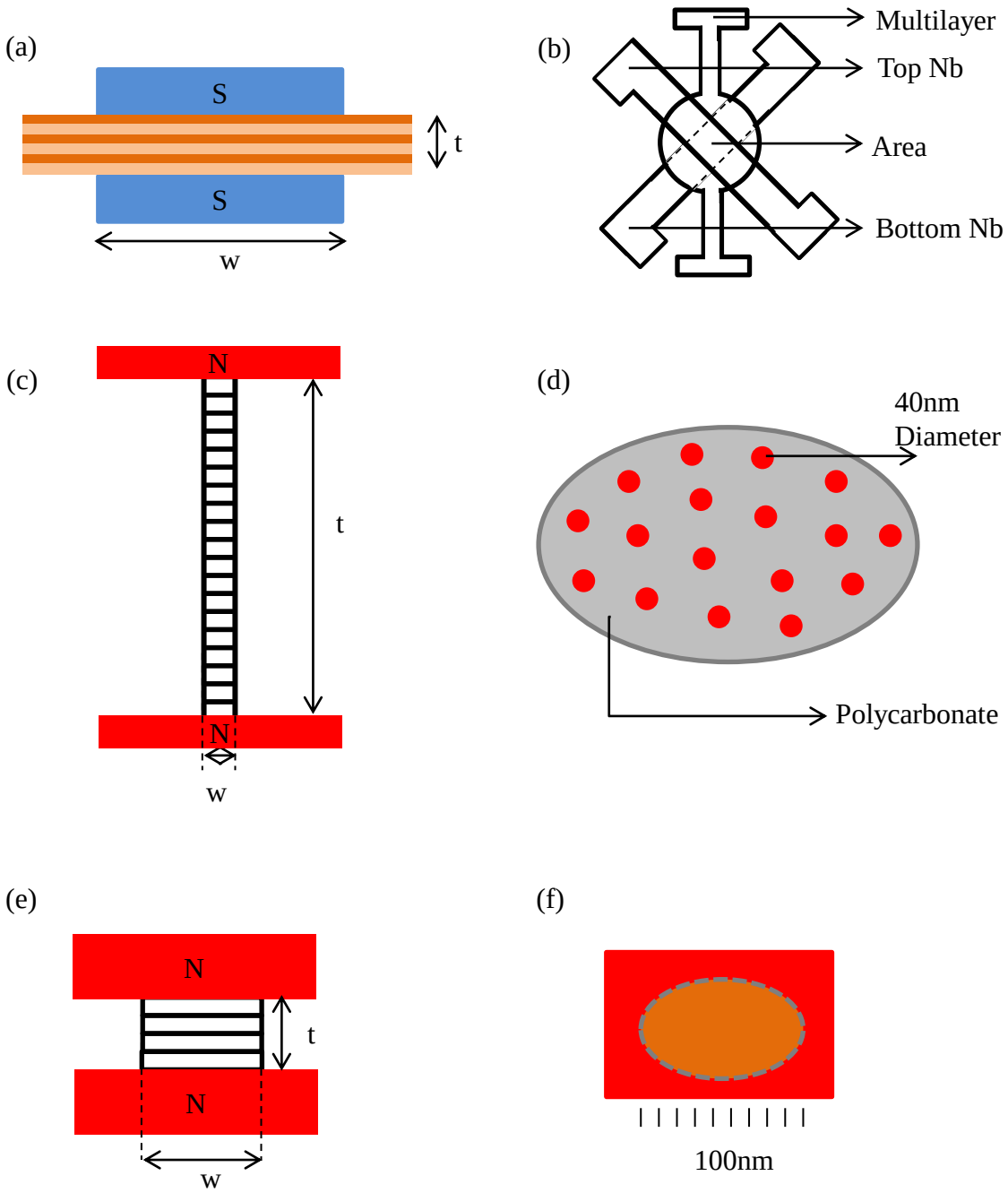

Figure 1.7: Schematics [After [33]] of (a) CPP S sample Cross-Section (b) CPP S sample Top View (c)CPP NW sample Cross-Section (d) CPP NW sample Top View (e) CPP P sample Cross-Section (f) CPP Nano Pillar Top View.

able N thickness, the coupling between F layers alternates between ferromagnetic and antiferromagnetic as the N layer thickness increases [34][35]. The F layers finally become uncoupled when the N layers get thick enough. Figure 1.8 shows a magnetic field sweep for an uncoupled $[Co(6)/Ag(6)]_6$ multilayer [5]. The highest value of resistance is obtained at H=0 Oe in the as-prepared state (AR(0) in Fig1.8) which is not recovered once the sample is taken to a high field saturation (AR(P) in Figure 1.8. After saturation, an intermediate maximum AR is obtained at AR(Peak) at the coercive field H_c.

In strictly uncoupled $[F/N]_n$ the maximum AR at H=0 Oe, AR(0), is only a lower bound to the true AP state [5]. It is not easy to determine how close AR(0) is to the true AR(AP).

3) **Spin Valve Structures:** Spin Valves overcome these disadvantages [36][37]. In spin valves, the Coercive fields of adjacent F layers are made different and the N layer separating the F layers is made thick enough to magnetically decouple the F layers. Application of a field larger than the larger coercive field of the F layers causes the magnetizations to align parallel to each other giving the P state. When the field direction is reversed and swept, the F layer with the lower coercive field switches first, giving the AP state. When the field is swept further, the F layer with the higher coercive field switches, giving the parallel state.

   Different coercive fields for the two F layers can be achieved by:

   a) **Hybrid Spin Valves:** Using two different ferromagnetic metals with different coercive fields, or using two different thicknesses of the same ferromagnetic metal. Figure 1.9 shows a magnetic field sweep for a Hybrid Spin Valve of the form

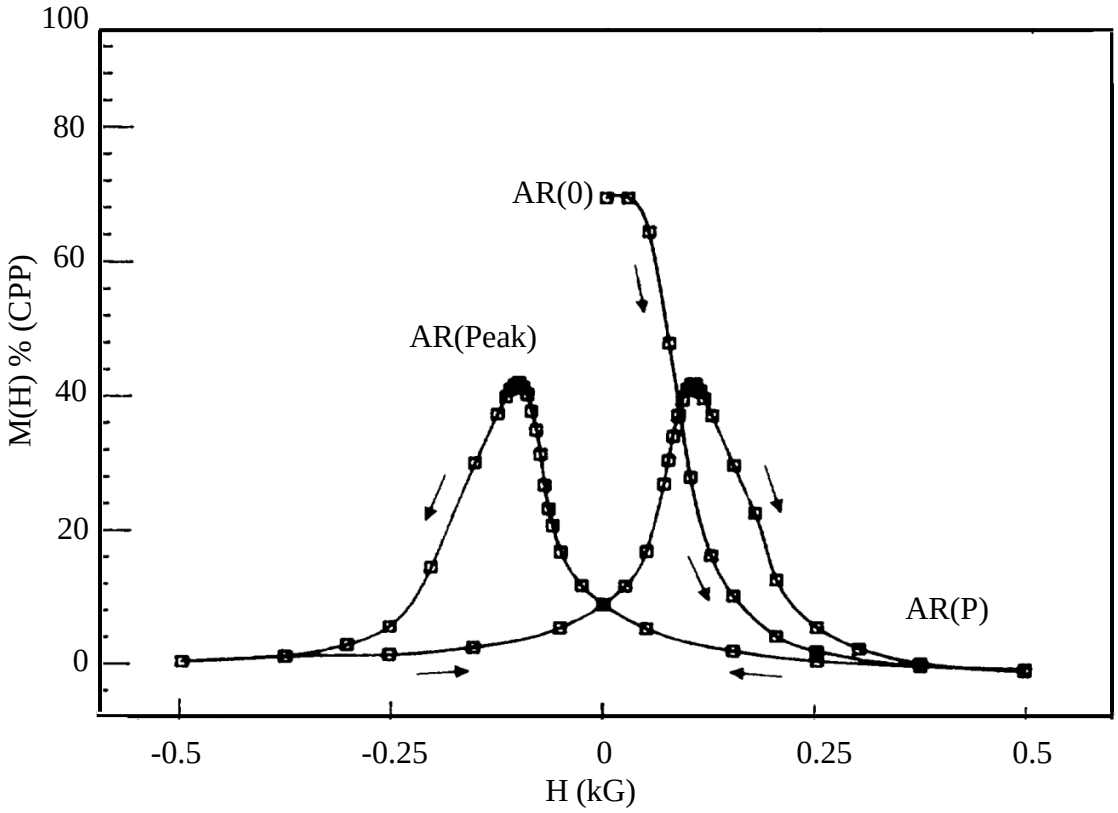

Figure 1.8: $[Co(6)/Ag(6)]_{60}$ multilayer with AR(0) representing the as prepared state resistance. AR(peak) is the intermediate maximum, while AR(P) is the parallel state resistance. [5]

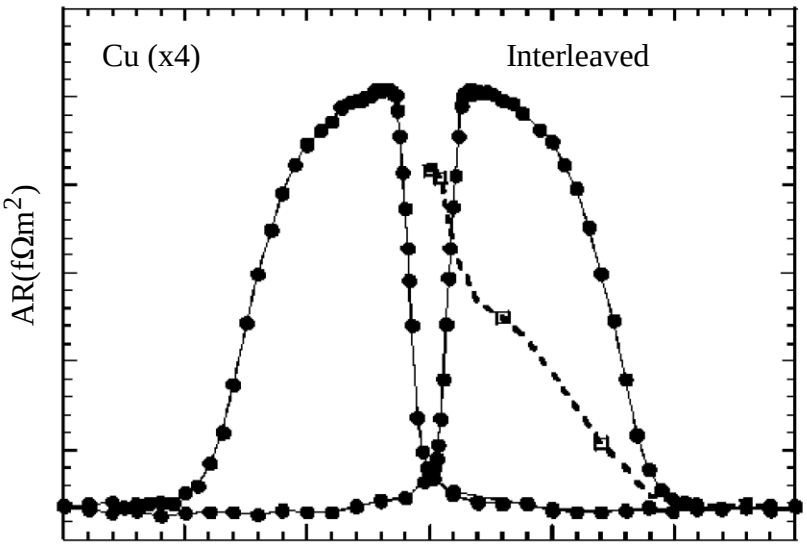

Figure 1.9: Hybrid Spin Valve [Co(8nm)/Cu(10nm)/Co(1nm)/Cu(10nm]$_n$ with n = 4 [38]. Notice the as prepared state AR(0) is lower than the AR(AP) confirming that AR(0) is only a lower bound to the AP state.

[Co(8nm)/Cu(10nm)/Co(1nm)/Cu(10nm)]$_n$ [38]. Note that AR(0) is below AR(AP), consistent with the expectation that AR(0) is a lower bound to the AP state.

b) **Exchange Biased Spin Valve (EBSV):** In 1956 Meiklejohn and Bean [39] discovered that the moments of a ferromagnet can be pinned by an adjacent antiferromagnet (AF) layer. Hysteresis curves of isolated F layers are symmetric about zero magnetic field. This implies that aligning the magnetization of an F metal along an easy axis requires the same energy for both 0 and 180 degrees orientation of the magnetization (Figure 1.10a). When an F layer is grown next to an AF layer, the coercivity of the ferromagnetic layer increases due to coupling with the AF Figure 1.10b. The coer-

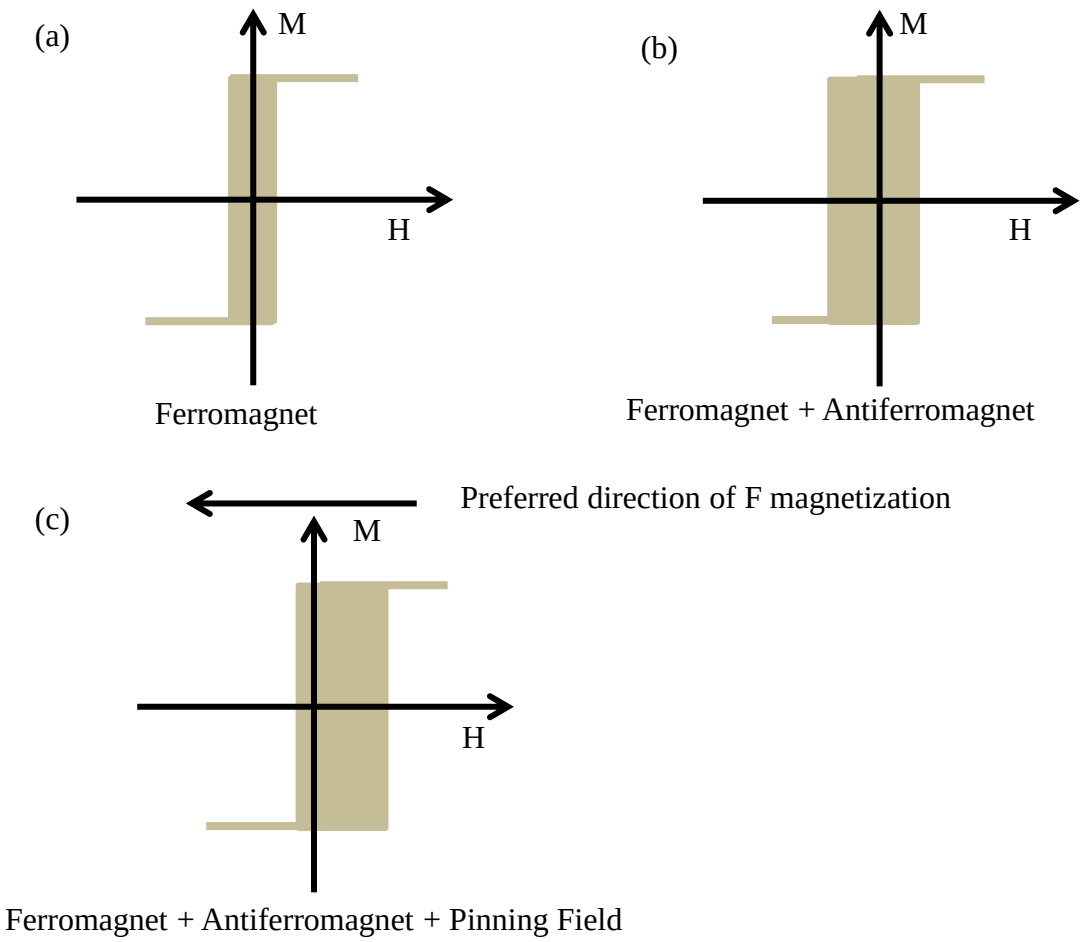

Figure 1.10: Schematic of (a)a hysteresis curve of a free ferromagnet. (b) increase of the coercivity of a ferromagnet adjacent to an antiferromagnet. (c) Magnetization anisotropy created by heating the ferromagnet/antiferromagnet arrangement above the AF Blocking temperature and then cooling in a magnetic field.

civity falls off as 1/t, where t is the thickness of the ferromagnetic layer. When the F/AF layers are heated above the Blocking temperature of the AF layer, and then cooled in the presence of a magnetic field, the hysteresis curve becomes asymmetric about zero magnetic field (Figure 1.10c), the magnetization of the F layer preferring to align along the pinned, or easy magnetization direction. In the sample structure AF/F_{Pinned}/N/F_{Free}, with the two F layers (F_{Pinned} and F_{Free}) magnetically uncoupled due to the N layer in between, the 'pinned' F layer hysteresis is asymmetric about zero while the F_{Free} layer is symmetric. Figure 1.11 shows minor and major field sweeps for an EBSV sample. This method ensures a well defined AP state of magnetization of the F layers.

1.7 This Thesis

1) The first project involves comparing our measurements of the AR of Palladium(Pd)/Iridium(Ir) interfaces with no-free-parameter calculations of AR. The experiment was done double-blind, i.e., no results were shared between us and our theoretical colleagues until after each of us got our 'best values'. In prior studies, comparing measured interface resistances of metal pairs with very close lattice parameters ($< 1\%$) with no-free-parameter calculations gave agreements within mutual uncertainties ($< 20\%$). However experiments on metal pairs with lattice parameters differing by 5% or more disagreed with calculations by 50% or more. We chose Pd/Ir, with lattice parameters differing by 1.3%, as an intermediate case. We will compare our experimental best estimate with no-free parameter calculations.

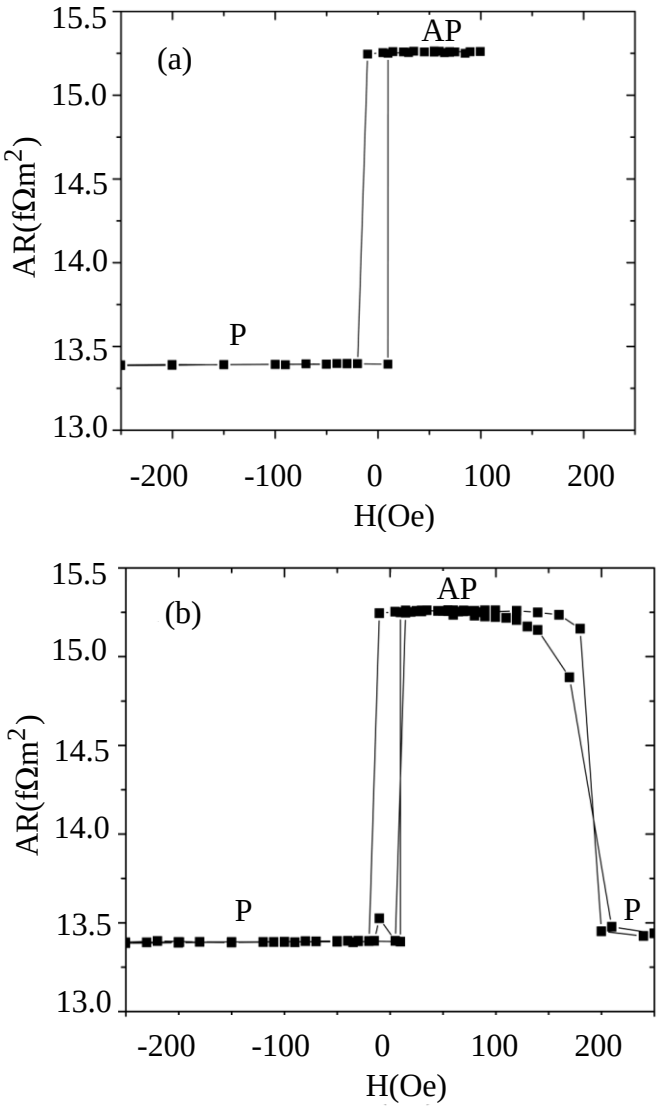

Figure 1.11: EBSV of the form FeMn(8nm)/Py(24nm)/Cu(10nm)/Py(24nm), showing minor (a) and major (b) loops. Initially a large negative magnetic field along the preferred direction of M for the F_{Pinned} layer, aligns the magnetizations in the F_{Pinned} and F_{Free} parallel to each other (P state). When the magnetic field is reversed in the positive direction, the F_{Free} magnetization switches at its H_c while the F_{Pinned} remains pinned, giving the AP state. On reversing the field back to the negative direction, the F_{Free} layer switches back to retrieve the P state. The switching of just the F_{Free} layer is symmetric about zero field and is referred to as a Minor loop (Figure 1.11a). Figure 1.11b shows that at large enough fields ($>H_c$) the F_{Pinned} layer also switches, giving back the P state. On reversing the field direction, the magnetic anisotropy of the F_{Pinned} layer drives it back in the pinned direction for a field $H<H_c$, giving the AP state. A magnetic field sweep showing the switching of both the F_{Pinned} and F_{Free} layers is referred to as a Major loop.

2) The second project involves spin-flipping of conduction electrons within the bulk of two antiferromagnets (FeMn and IrMn) and at the interfaces of these antiferromagnets with Cu. These antiferromagnets are widely used in Giant Magnetoresistance studies and simple theory predicts that spin-flipping in highly ordered antiferromagnets should be weak. We will be looking for the strength of spin-flipping in real sputtered antiferromagnets, which are disordered, and at the interfaces of these antiferromagnets with Cu.

3) An ideal half metal should completely stop electrons with one spin moment direction and pass electrons with the other spin moment direction. Hence an ideal half metal should have maximal scattering asymmetry, and produce a very large CPP-MR. We grow epitaxial layers of the predicted half metallic Heusler alloy CFAS ($Co_2FeAl_{0.5}Si_{0.5}$) on Nb/Cu and Nb/Ag underlayers. Epitaxial CFAS is then used as a part of a hybrid spin valve in hopes of obtaining transport properties of CFAS.

In addition to the projects included in this thesis, I have contributed to other projects in our group which are not included in this thesis. I have second-authored three published papers [40] [41][42], where my contribution has been substantial. In two studies we used $[F/N]_n$ multilayers within Py based double EBSV structures to find the spin flipping probability at F/N interfaces such as $Co_{90}Fe_{10}$/Cu [40] and Co/Cu [41]. In the third study we determined the interface specific resistance and spin flipping probability of the interfaces between the two ferromagnets, Co and Ni, using $[Co/Ni]_n$/Co and $[Ni/Co]_n$/Ni multilayers within Py based double EBSV structures [42]. I have also co-authored three additional published papers [43][44][45] with lesser contribution.

The rest of this thesis is organized as follows. Chapter 2 describes theoretical models

of CPP R transport. Chapter 3 describes the various sample fabrication and measurement techniques. Chapters 4,5, and 6 are devoted to the three separate projects.

To increase the commercial utility of CPP MR devices, studies concentrate on increasing its sensitivity. To achieve that, one needs to know the various parameters that affect CPP MR. This thesis is a contribution to obtaining that knowledge.

Chapter 2

Theory

In this Chapter we describe theoretical models for CPP MR in magnetic multilayers. Reviews [46] [6] [47] have described the theory of GMR in extensive detail. The theory of GMR has also been treated in detail in previous theses from our group [16] and [26] and others [48].

In this thesis we will start with the first phenomenological explanation of CPP MR using a two current series resistor model. We will follow with the Valet Fert theory under the Boltzmann Formalism. We will conclude the chapter with a section dedicated to the theoretical background of the projects in this thesis. The theoretical background for the project discussed in Chapter 4 involves the Landauer Büttiker formalism of transport across multilayers, used to analyze the interfaces of metallic multilayers, while that for Chapter 5 is based on application of the Valet Fert model to derive the spin flipping behavior in metals and at interfaces.

2.1 Two Current Series Resistor Model

Zhang and Levy [4] developed the first theoretical model for CPP transport in an F/N multilayer or F/N/F trilayer assuming no spin flipping and no spin mixing, which leads to two independent spin channels of current. Spin flipping scatterings occur due to spin-orbit scattering of impurities without a local moment in the host metal or spin-spin scattering by impurities with a local moment in the host metal. Spin mixing is a phenomenon of transfer of momentum between electrons with different k states at temperatures where magnon and phonon collisions are significant. They also assumed diffusive transport within the individual layers. The total resistance for each independent current channel is the sum of the resistances in each channel. This model is called the 2 Current Series Resistor (2CSR) model. Later Lee et al [49] and Valet and Fert [27] wrote the equations that gave the resistance of each current channel as simply the series resistor sum of the resistances of the bulk and the interfaces constituting the multilayers (See Figure 2.1). The basic parameters used to describe the 2CSR model are:

1) The asymmetric resistivities of electrons in an F metal, ${\rho_F}^{\uparrow}$ and ${\rho_F}^{\downarrow}$ (Section1.3) from which we can define the bulk scattering anisotropy parameter $\beta_F = \frac{({\rho_F}^{\downarrow} - {\rho_F}^{\uparrow})}{({\rho_F}^{\downarrow} + {\rho_F}^{\uparrow})}$ and the enhanced F resistivity ${\rho_F}^{*} = \frac{({\rho_F}^{\downarrow} + {\rho_F}^{\uparrow})}{4} = \frac{\rho_F}{(1 - {\beta_F}^{2})}$, where ρ_F is the resistivity of the F metal measured independently using the Van der Pauw (VdP) technique (Section 3.3.3).

2) The asymmetric specific resistances at the F/N interfaces ${AR_{F/N}}^{\uparrow}$ and ${AR_{F/N}}^{\downarrow}$. We define the interface scattering anisotropy parameter $\gamma_{F/N} = \frac{({AR_{F/N}}^{\downarrow} - {AR_{F/N}}^{\uparrow})}{({AR_{F/N}}^{\downarrow} + {AR_{F/N}}^{\uparrow})}$ and enhanced interface specific resistance ${AR_{F/N}}^{*} = \frac{({AR_{F/N}}^{\downarrow} + {AR_{F/N}}^{\uparrow})}{4}$.

3) Since normal metals don't exhibit spin scattering asymmetry, the resistivity of normal metals has ${\rho_N}^{\uparrow} = {\rho_N}^{\downarrow}$. The resistivity measured using the VdP technique is ρ_N, which is related to ${\rho_N}^{\uparrow}$ and ${\rho_N}^{\downarrow}$ by $2\rho_N = {\rho_N}^{\uparrow} = {\rho_N}^{\downarrow}$

2.1.1 Analysis of AP and P states using 2CSR Model

Consider a single F/N/F trilayer with equal F layer thicknesses t_F and N layer thickness t_N in parallel (P) and antiparallel (AP) magnetization configurations (Figure 2.1(a) and (b)). Assume no spin flipping and no resistance of outer contacts. Let us define here a length scale in metals, called the spin diffusion length (ℓ_{sf}), which determines the distance an electron diffuses before undergoing a spin flipping collision. Therefore the assumption of no spin flipping entails that the thicknesses of the individual layers are smaller than their respective ℓ_{sf}. In Figure 2.1, the current flows through area A. In the 2CSR model, the specific resistances in the AP and P states for the spin moments up and down electrons are:

$$AR_{up}(AP) = {\rho_F}^{\uparrow} t_F + {AR_{F/N}}^{\uparrow} + 2\rho_N t_N + {AR_{F/N}}^{\downarrow} + {\rho_F}^{\downarrow} t_F \tag{2.1a}$$

$$AR_{down}(AP) = {\rho_F}^{\downarrow} t_F + {AR_{F/N}}^{\downarrow} + 2\rho_N t_N + {AR_{F/N}}^{\uparrow} + {\rho_F}^{\uparrow} t_F \tag{2.1b}$$

$$AR_{up}(P) = {\rho_F}^{\uparrow} t_F + {AR_{F/N}}^{\uparrow} + 2\rho_N t_N + {AR_{F/N}}^{\uparrow} + {\rho_F}^{\uparrow} t_F \tag{2.1c}$$

$$AR_{down}(P) = {\rho_F}^{\downarrow} t_F + {AR_{F/N}}^{\downarrow} + 2\rho_N t_N + {AR_{F/N}}^{\downarrow} + {\rho_F}^{\downarrow} t_F \tag{2.1d}$$

$\therefore AR_{up}(AP) = AR_{down}(AP)$. Taking two channels of current, majority and minority spin, flowing parallel to each other, the total resistance of the network is given as,

$$AR(AP) = \frac{AR_{down}(AP) \times AR_{up}(AP)}{AR_{down}(AP) + AR_{up}(AP)} = \frac{AR_{up}(AP)}{2} = \frac{AR_{down}(AP)}{2} \tag{2.2a}$$

$$AR(P) = \frac{AR_{down}(P) \times AR_{up}(P)}{AR_{down}(P) + AR_{up}(P)} \tag{2.2b}$$

$$A\Delta R = AR(AP) - AR(P) = 4\frac{[\gamma {AR^*}_{F/N} + \beta {\rho_F}^* t_F]^2}{2{\rho^*}_F t_F + \rho_N t_N + 2{AR^*}_{F/N}} \tag{2.3}$$

The equations for AR(AP) and AΔR can be re-written using the parameters β_F,$\gamma_{F/N}$,${\rho_F}^*$ and ${AR^*}_{F/N}$ as

$$AR(AP) = 2{\rho_F}^* t_F + 2{AR_{F/N}}^* + \rho_N t_N \tag{2.4}$$

and

$$A\Delta R = 4\frac{[\gamma {AR^*}_{F/N} + \beta {\rho_F}^* t_F]^2}{AR(AP)}. \tag{2.5}$$

The addition of superconducting layers on each side of a CPP sample doesn't add any spin dependent resistance but just adds a constant $2\mathrm{AR}_{S/F}$ in the denominator of Equation 2.5. The final equation can be written as

$$A\Delta R = 4\frac{[\gamma {AR^*}_{F/N} + \beta {\rho_F}^* t_F]^2}{AR(AP)}. \tag{2.6}$$

$$AR(AP) = 2{\rho_F}^* t_F + 2{AR_{F/N}}^* + \rho_N t_N + 2AR_{S/F} \tag{2.7}$$

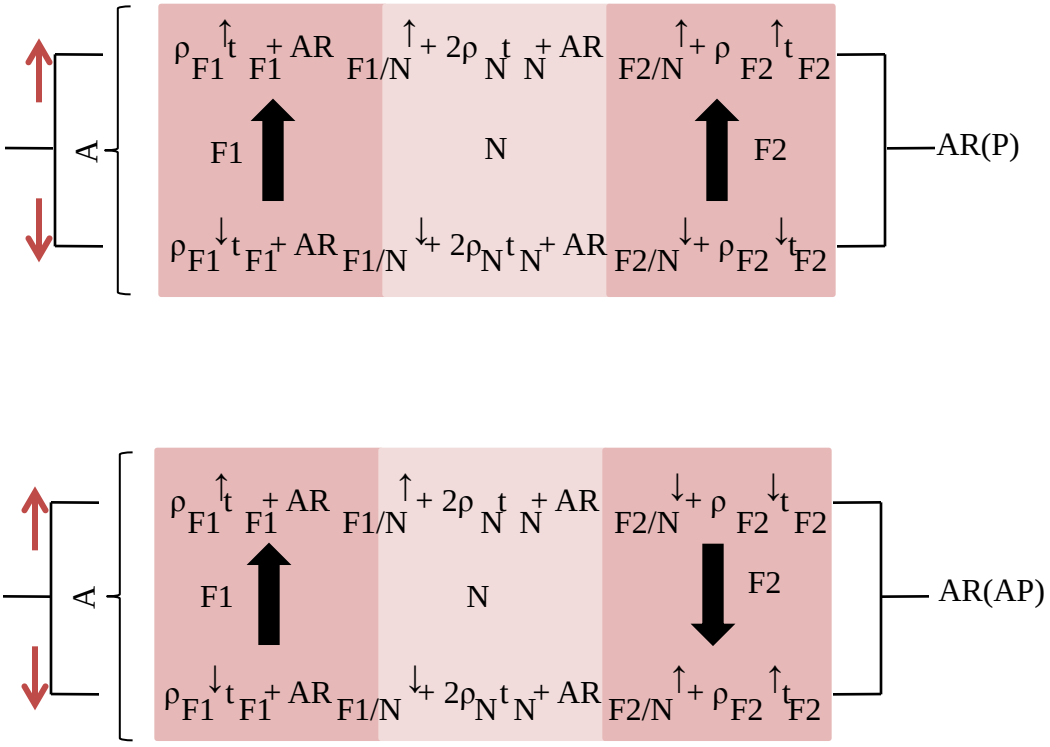

Figure 2.1: F1/N/F2 in the (a) Parallel configuration (b) Antiparallel configuration

2.1.2 Test of the 2CSR Model

As mentioned in Section 2.1, the 2CSR model assumed no spin flipping and no spin mixing within the layers of an F/N multilayer. In this section we review tests of the validity of the assumption in certain cases. Let us consider an $[F/N]_n$ multilayer structure where F is chosen such that $t_F \ll {\ell_{sf}}^F$ (F spin diffusion length) and the ${\ell_{sf}}^N$ is very long. Such a condition ensures that the no spin flipping assumption of the 2CSR model is fulfilled. Neglecting the difference between n and $n+1$ in the $[F/N]_n$ multilayer, AR(AP) becomes,

$$AR(AP) = 2AR_{S/F} + n({\rho_F}^* t_F + 2{AR_{F/N}}^* + \rho_N t_N) \tag{2.8}$$

and AΔR becomes

$$A\Delta R = \frac{n^2(2\gamma {AR^*}_{F/N} + \beta {\rho_F}^* t_F)^2}{2AR_{S/F} + n({\rho_F}^* t_F + 2{AR_{F/N}}^* + \rho_N t_N)}. \tag{2.9}$$

Rearranging Equation2.8 and taking square root of both sides gives

$$\sqrt{A\Delta R(AR(AP))} = n(2\gamma {AR^*}_{F/N} + \beta {\rho_F}^* t_F) \tag{2.10}$$

In a set of multilayers with fixed F layer thickness t_F, Equation 2.10 is independent of ρ_N and t_N. A plot of the left hand side versus n should give a straight line that passes through the origin with slope equal to $2\gamma {AR^*}_{F/N} + \beta {\rho_F}^* t_F$.

Since the right hand side of Equation 2.10 is independent of ρ_N, changing the N metal to an alloy N$'$ with a higher ${\rho_N}'$ but still long ${\ell_{sf}}^{N'}$ should leave the plot unchanged [[33] and

ref therein]. Let us consider the experiments by [50] and [51] with $[F/N]_n$ multilayers where the F layer was chosen to be Co with a fixed thickness of $t_F = 6$nm and the total thickness of the multilayers, $t_T = n(t_N + 6)$ was maintained at 360nm or 720nm. The Co thickness was chosen to be much less than its spin diffusion length (${\ell_{sf}}^{Co} \gg 6$nm [52]) so that the spin flipping in the Co layers could be neglected. As the number of bilayers n decreases, t_N increases. As long as n is large enough so that the $t_N \ll {\ell_{sf}}^N$, Equation 2.10 is valid. As n is reduced, the ratio of t_N to ${\ell_{sf}}^N$ could become large enough that Equation 2.10, based on the assumption of no spin flipping, would not be satisfied. The N metal was chosen to be pure Cu with ${\ell_{sf}}^{Cu} \geq 200$nm [53] [54] at 4.2K. Figure 2.2 shows a plot of Equation 2.10 for a $[Co/Cu]_n$ multilayer system. The open circle data are consistent with a straight line passing through the origin. If Cu is alloyed with an impurity such as Ge, its resistivity changes from ρ_{Cu} for pure Cu to ρ_N for alloyed Cu ($\rho_{CuGe} \gg \rho_{Cu}$). The atomic number of Ge is close to Cu such that the spin orbit scattering cross section of Cu and Ge is small and should not cause much spin flipping. The validity of Equation 2.10, for no spin flipping, should be still satisfied with Ge alloying. As expected, the filled square data for Cu alloyed with Ge falls close to the straight line through the origin for nominally pure Cu. This experiment represents a test of the validity of the 2CSR model.

The above discussion is able to justify the validity of the 2CSR model for no spin flipping in Cu. However if the nominally pure Cu is alloyed with impurities such as Pt, with large spin-orbit scattering cross-section, or Mn with spin-spin interactions due to the Mn local moment in Cu, the spin diffusion length of the alloyed Cu should reduce. This reduction should cause a deviation from the straight line behavior in Equation 2.10 as n is decreased, ie, t_N is increased and eventually becomes larger than ${\ell_{sf}}^N$. The fractional deviation should

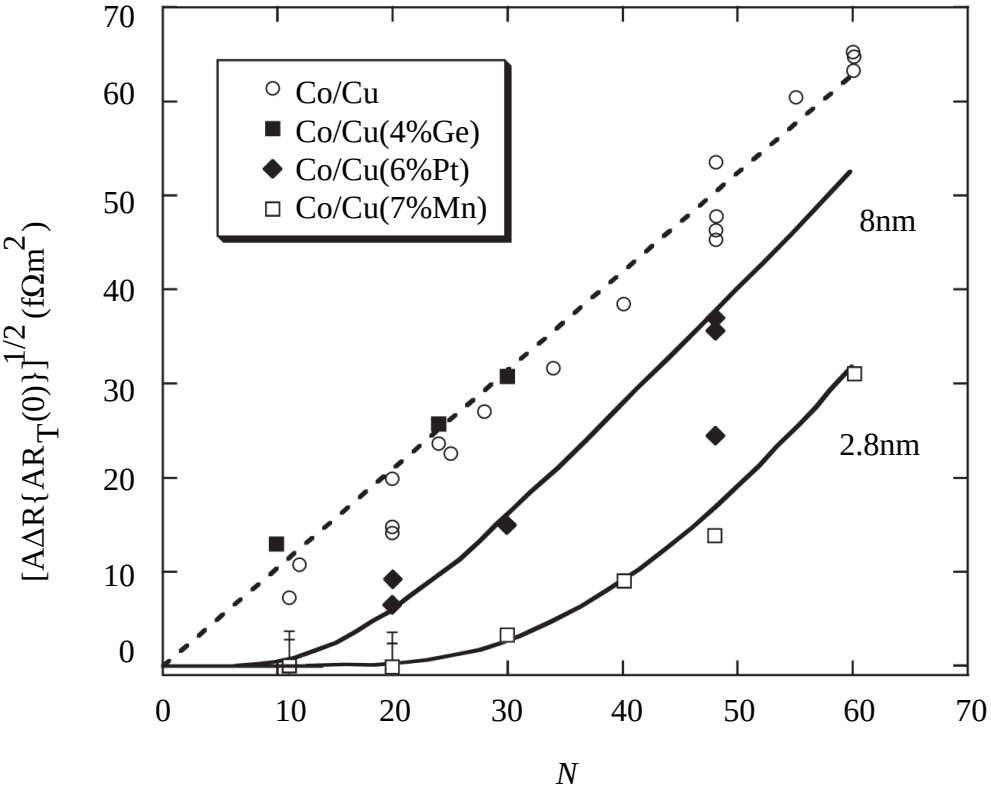

Figure 2.2: $\sqrt{A\Delta R(AR(AP))}$ *versus* n for Co and Cu based alloys. [50]

increase with decreasing n. Figure 2.2 shows that this expectation is obeyed for Cu alloyed with Pt and Mn. That is, the 2CSR model is no longer obeyed when the thickness of the N layer becomes larger than its spin diffusion length (Figure 2.2 shows the values of ${\ell_{sf}}^N$ for the alloyed Cu). In the next sections we will describe the Valet Fert (VF) theory, show that the deviations of the data for Cu alloyed with Pt or Mn from the straight line are quantitatively consistent with its predictions.

2.2 Boltzmann Formalism for CPP MR- Valet Fert Model

This section closely follows the Valet Fert paper [27] and other reviews on the Valet Fert theory of CPP MR which is based on the semi-classical Boltzmann theory of transport. Boltzmann formalism provides a microscopic theory of transport in metals based on an electron distribution function f given, at equilibrium, by the Fermi distribution function f_0. In the steady state, the Boltzmann transport equation is given as

$$\frac{d}{dt}f = (\frac{d}{dt}f)_E - (\frac{d}{dt}f)_{Scatt} = 0 \tag{2.11}$$

where E is the electric field and f (short for $f(r, v)$) is a quasi static electron distribution which gives the number of electrons with given position r and velocity v. The Valet Fert theory is based on the following assumptions:

1) A free electron band structure which neglects Fermi surface effects on the individual layers and at the F/N interfaces.

2) No spin mixing (neglecting electron magnon and electron phonon scattering), making it most suitable to analyze CPP MR at low temperature where magnon and phonon scatterings can be neglected.

3) Diffusive transport of electrons in the metal layers.

Valet Fert [27], showed that the Boltzmann equation model reduces to a macroscopic transport equation if the mean free paths of the individual layers are much smaller than their respective spin diffusion lengths. This condition is irrespective of the layer thickness to the mean free path ratio. Consider an infinite multilayer of alternating single domain F layers with N metal layers of thicknesses t_F and t_N, respectively, with a current density J flowing perpendicular to the layer surface in the z direction. A single parabolic band is considered with same effective mass m^* and Fermi velocity v_F of the electrons in the layers. A local velocity distribution function $f_s(z,v)$,the subscript representing the spin orientation $\pm$ along the x direction ($s_x = \pm\frac{1}{2}$ with spin quantization axis along the layer plane), is assumed for the conduction electrons. The + spin electrons would give - moment and hence are considered to be the minority electrons to the local F layer magnetization and –spin electrons would give + moment and hence would be considered the majority electrons. $f_s(z,v)$ is written as the combination of Fermi Dirac distribution function $f_0(v)$ and a perturbation term $g_s(z,v)$ which gives the anisotropic part of the electron distribution. Unlike the CIP geometry, the CPP geometry has the advantage of a cylindrical symmetry along the axis of current propagation. Therefore the anisotropic term can be expanded in Legendre Polynomials as

$$g_s(z,v) = [\mu^0 - \mu_s(z)] + \sum {n=1}^{\infty} {g_s}^n(z) P_n(cos\theta) \tag{2.12}$$

where θ is the angle between the velocity and the z axis. Here the equilibrium chemical potential is μ^0 and $\mu_s(z)$ describes local variations of the spin dependent chemical potential [27] to account for spin accumulation. Using the above distribution function in the Boltzmann equation one obtains a set of differential equations

$$\frac{e}{\sigma_s}\frac{\partial}{\partial z}J_s = \frac{\bar{\mu_s} - \bar{\mu_{-s}}}{{\ell_s}^2} \tag{2.13a}$$

$$\frac{\bar{\mu_s}}{dz} = \frac{e}{\sigma_s}J_s + \frac{2}{5}\frac{\partial}{\partial z}g^{(2)} \tag{2.13b}$$

$$\frac{{g_s}^{(3)}}{\lambda_s} + \frac{3}{7}\frac{\partial}{\partial z}{g_s}^{(2)} = -\frac{2}{3\kappa}\frac{\partial}{\partial z}J_s \tag{2.13c}$$

$$\frac{n+1}{2n+3}\frac{\partial}{\partial z}{g_s}^{(n+1)} + \frac{{g_s}^{(n)}}{\lambda_s} + \frac{n}{2n-1}\frac{\partial}{\partial z}{g_s}^{(n-1)} = 0 \; for \; n > 2. \tag{2.13d}$$

where $(\bar{\mu_s}(z) = \mu_s - eV(z)$ is the electrochemical potential for spin s. J_s is the current density for spin s. σ_s is the conductivity for spin s. $\lambda_s = v_F(\frac{1}{\tau_s} + \frac{1}{\tau_{sf}})^{-1}$ is the local mean free path for spin s. τ_s and τ_{sf} represent the spin conserving and spin flip scattering event relaxation times. ℓ_s is the spin diffusion length given by $\ell_s = \sqrt{(D_s\tau_{sf})}$ where D_s is the diffusion constant given as $D_s = \frac{\lambda_s v_F}{3}$. κ describes the relation between the Drude conductivity and spin current, $J_s = \kappa {g_s}^{(1)}$ and is spin independent in a single band model.

Apart from the $\frac{2}{5}\frac{\partial}{\partial z}{g_s}^{(2)}$ term in Equation 2.13b, Equations 2.13a and 2.13b are the same as the 1D spin diffusion equations of [55] [56] [57]. This extra term implies that the conservation of individual spin current channels breaks down due to the presence of spin flip relaxation which occurs at a length scale of l_s, the spin diffusion length. This term is called the "Boltzmann Correction". Therefore any spin current divergence occurs over a length scale of the spin diffusion length [46]. Hence we can approximate $\lambda_s\frac{\partial}{\partial z}J \approx \frac{\lambda_s}{\ell_s}J_s$

and if $\lambda_s \ll \ell_s$, the Boltzmann Equations 2.13 and 2.13 reduce to macroscopic transport equations. The "Boltzmann Correction" is therefore proportional to $\frac{\lambda_s}{\ell_s}$ and the macroscopic transport equations

$$\frac{e}{\sigma_s}\frac{\partial}{\partial z}J_s = \frac{\bar{\mu_s} - \bar{\mu_{-s}}}{{\ell_s}^2} \tag{2.14a}$$

$$\frac{\bar{\mu_s}}{dz} = \frac{e}{\sigma_s}J_s \tag{2.14b}$$

are recovered when $\lambda_s/\ell_s \ll 1$. Equation 2.14a states that at steady state, the spin accumulation due to current divergences is balanced by spin flip processes [27]. Equation 2.14b is Ohm's law. The term $\Delta\mu = (\bar{\mu_s}) - (\bar{\mu_{-s}})$ is the 'spin-accumulation' representing the difference of the spin up and spin down Fermi energies. In a free electron model $\Delta\mu$ is related to the out of equilibrium magnetization ΔM by $|\Delta\mu| = 2\mu_0\frac{|\Delta M|}{3n\mu_B}$, where μ_0 and μ_B are the magnetic permeability of empty space and the Bohr magneton, respectively. n is the electron density.

The condition $\lambda_s/\ell_s \ll 1$ for the validity of the macroscopic model is not always satisfied in real metals. However the macroscopic model often agrees with experiments even for such metals. Stiles and Penn [58] solved the Boltzmann equation numerically to verify that the macroscopic model remains valid even when l_s and λ_s are comparable.

Writing the spin-dependent electro-chemical potentials as $\bar{\mu_\pm} = \bar{\mu} \pm \Delta\mu$, where $\Delta\mu$ is related to spin accumulation, Equations 2.14a and 2.14b become

$$\frac{e}{\sigma_\pm}\frac{\partial}{\partial z}J_\pm = \pm 2\frac{\Delta\mu}{{\ell_s}^2} \tag{2.15}$$

$$J_{\pm}(z) = \sigma_{\pm}[F(z) \pm \frac{\partial \Delta\mu}{e\partial z}] \tag{2.16}$$

where $F(z) = \frac{\partial \bar{\mu}}{e\partial z}$ is equivalent to an electric field due to the spin independent part of the electrochemical potential.

Van Son et al [55] have shown that from the two equations Equations 2.14a and 2.14b one can deduce differential equations given as

$$\frac{\partial^2}{\partial z^2}\Delta\mu = \frac{\Delta\mu}{{\ell_{sf}}^2} \tag{2.17}$$

$$\frac{\partial^2}{\partial z^2}(\sigma_-\mu_- + \sigma_+\mu_+) = 0 \tag{2.18}$$

where $\frac{1}{{\ell_{sf}}^2} = \frac{1}{{\ell_{\uparrow}}^2} + \frac{1}{{\ell_{\downarrow}}^2}$.

In a homogeneous medium, the two differential Equations 2.17 and 2.18 have the general solutions,

$$\Delta\mu = Ae^{(\frac{z}{\ell_{sf}})} + Be^{(\frac{-z}{\ell_{sf}})} \tag{2.19}$$

$$\sigma_-\mu_- + \sigma_+\mu_+ = Cz + D. \tag{2.20}$$

VF give the general expressions for $\mu_{\pm}(z)$,$\Delta\mu$,$F(z)$ and $J(z)$ in a homogeneous layer (n) with constants of integration $K_i(n)$. When the F layer magnetization is up, the solutions are given by

$$\bar{\mu_+}(z) = (1-\beta^2)e{\rho_F}^* Jz + {K_1}^{(n)} + (1+\beta)[{K_2}^{(n)}e^{(\frac{z}{{\ell_{sf}}^F})} + {K_3}^{(n)}e^{(\frac{-z}{{\ell_{sf}}^F})}] \tag{2.21}$$

$$\bar{\mu_-}(z) = (1-\beta^2)e\rho_F{}^* Jz + K_1{}^{(n)} - (1-\beta)[K_2{}^{(n)}e^{(\frac{z}{\ell_{sf}{}^F})} + K_3{}^{(n)}e^{(\frac{-z}{\ell_{sf}{}^F})}] \tag{2.22}$$

$$\Delta\mu(z) = K_2{}^{(n)}e^{(\frac{z}{\ell_{sf}{}^F})} + K_3{}^{(n)}e^{(\frac{-z}{\ell_{sf}{}^F})} \tag{2.23}$$

$$F(z) = (1-\beta^2)e\rho^{F*}J + \frac{\beta}{e\ell_{sf}{}^F}[K_2{}^{(n)}e^{(\frac{z}{\ell_{sf}{}^F})} + K_3{}^{(n)}e^{(\frac{-z}{\ell_{sf}{}^F})}] \tag{2.24}$$

$$J_+(z) = (1-\beta)\frac{J}{2} + \frac{1}{2e\rho_F{}^*\ell_{sf}{}^F}[K_2{}^{(n)}e^{(\frac{z}{\ell_{sf}{}^F})} + K_3{}^{(n)}e^{(\frac{-z}{\ell_{sf}{}^F})}] \tag{2.25}$$

$$J_-(z) = (1+\beta)\frac{J}{2} - \frac{1}{2e\rho_F{}^*\ell_{sf}{}^F}[K_2{}^{(n)}e^{(\frac{z}{\ell_{sf}{}^F})} + K_3{}^{(n)}e^{(\frac{-z}{\ell_{sf}{}^F})}] \tag{2.26}$$

where β and $\rho_F{}^*$ have been defined before. For an F layer with down magnetization, the positive and negative indices are interchanged and $\Delta\mu$ changes sign. For an N layer the solutions are,

$$\bar{\mu_\pm}(z) = e\rho_N Jz + K_1{}^{(n)} + [K_2{}^{(n)}e^{(\frac{z}{\ell_{sf}{}^N})} + K_3{}^{(n)}e^{(\frac{-z}{\ell_{sf}{}^N})}] \tag{2.27}$$

$$\Delta\mu(z) = K_2{}^{(n)}e^{(\frac{z}{\ell_{sf}{}^N})} + K_3{}^{(n)}e^{(\frac{-z}{\ell_{sf}{}^N})} \tag{2.28}$$

$$F(z) = \rho_N J \tag{2.29}$$

$$J_\pm(z) = \frac{J}{2} + \frac{1}{2e\rho_N{}^*\ell_{sf}{}^N}[K_2{}^{(n)}e^{(\frac{z}{\ell_{sf}{}^N})} + K_3{}^{(n)}e^{(\frac{-z}{\ell_{sf}{}^N})}]. \tag{2.30}$$

The complete solutions for a given multilayer are obtained by matching the boundary conditions at the interfaces of each two metals. At an interface the currents J_+ and J_- are

continuous if we neglect spin relaxation at the interface, while $\bar{\mu_+}$ and $\bar{\mu_-}$ are continuous if there is no interface scattering. If an infinitesimally thin interface at z_0 causes localized scattering only at the interface, the potentials are given by,

$$\mu^-_{\uparrow,\downarrow}(z = {z_0}^+) - \mu^-_{\uparrow,\downarrow}(z = {z_0}^-) = {AR_{F/N}}^{\uparrow,\downarrow} J_{\uparrow,\downarrow}(z = z_0)/e \tag{2.31}$$

where ${AR_{F/N}}^{\uparrow,\downarrow}$ is the spin dependent boundary resistance at an F/N interface. Using the solutions in the individual layers given above and the boundary conditions, all quantities of interest can be obtained in a multilayer structure.

Even though the Valet Fert model is based on a simplified assumption of electronic band structures, it has agreed very well with experiments in CPP MR [33] in the past two decades. Independent experiments of Conduction Electron Spin Resonance, Weak Localization, Lateral Non-Local and superconducting tunneling measurements have all been used to derive spin diffusion lengths of metals. The results are listed in Tables 1,2 and 3 in [33]. The general agreement between the CPP experiments and the other independent methods suggest that the Valet Fert model is a good approximation to CPP transport in multilayers.

As an example of the value of Valet Fert model, consider a simple Py based EBSV structure of the form Nb/FeMn(8nm)/Py(t_{Py})/Cu(20nm)/Py(t_{Py})/Nb. As long as the thicknesses of the Py and Cu layers are much less than their respective spin diffusion lengths (${\ell_{sf}}^{Cu}$=100nm and ${\ell_{sf}}^{Py}$=5.5nm), $A\Delta R$ follows Equation2.6 with F=Py and N=Cu. The numerator and the denominator of $A\Delta R$ increase as the thickness of t_{Py} increases. However

when $t_{Py} \geq {\ell_{sf}}^{Py}$, with ${\ell_{sf}}^{Cu}$ still long, the more general VF becomes,

$$A\Delta R = 4\frac{[\gamma A{R^*}_{F/N} + \beta{\rho_F}^*{\ell_{sf}}^F]^2}{2{\rho^*}_F{\ell_{sf}}^F + \rho_N t_N + 2A{R^*}_{F/N}} \tag{2.32}$$

That is, it replaces the t_F in numerator of Equation 2.6 with ${\ell_{sf}}^F$ and makes more drastic changes in the denominator. The denominator is reduced to just the total AR of an "active" region of the EBSV consisting of just the contributions between the lengths ${\ell_{sf}}^{Py}$ beyond the Py/Cu interfaces. That is, the denominator becomes just $(2{\rho^*}_F{\ell_{sf}}^F + \rho_N t_N + 2A{R^*}_{F/N})$. The rest of the Py layers, as well as the FeMn layer and the interfaces Py/FeMn, FeMn/Nb, and Py/Nb no longer contribute to the denominator. If we use this basic structure as a starting point to introduce a metal insert in the middle of the Cu layer, the source of any change in $A\Delta R$ can be isolated to be due to only the insert. Any contribution from a fluctuation of Py thickness between samples is irrelevant as far as the value of AΔR is concerned.

2.3 Present Work

In this section we will discuss theoretical backgrounds pertaining to the projects in this thesis by dividing this section into two subsections. The first subsection is devoted to the theoretical background for the Ir/Pd specific interface resistance project (Chapter 4). We will first describe the basis of the reduction of the 2CSR model for Ir/Pd multilayered samples, to a simple one current resistor model. Secondly, we will describe the Landauer Büttiker scattering formalism used to derive the specific interface resistance of two metals. In our

case, the scattering formalism was used by our colleagues in China to calculate $2AR_{Ir/Pd}$. In the second subsection, we will describe an application of the Valet Fert theory to study spin flipping in an N metal and at N/Cu interfaces. In our case, N will be the antiferromagnets IrMn and FeMn (Chapter 5).

2.3.1 Theoretical background of the study of Ir/Pd specific interface resistance:

2.3.1.1 Series resistor Model application to Ir/Pd

The CPP S structure of our samples, using Nb superconducting electrodes, is given in detail in Chapter 4. For the present discussion it suffices to note that the sample structure consists of essentially an S/Cu/F/N/F/Cu/S multilayer where F= Cobalt (Co) layers of thickness 10nm and N=n bilayers of Iridium and Palladium, ie, $[Ir/Pd]_n$ of fixed total thickness t_T= 360nm. The thicknesses of Co are much smaller than its spin diffusion length. However we need to be careful while applying the resistor model to Ir and Pd. ${\ell_{sf}}^{Pd} \sim$ 25nm while ${\ell_{sf}}^{Ir}$ is unknown. We can use resistivity of Ir and Pd as a guide to estimate ${\ell_{sf}}^{Ir}$. From Table 3.4, we see that $\rho_{Ir} \sim 2.5\rho_{Pd}$. Following the discussion in [33] (Figure 14 in [33]), we use the relation $\ell_{sf} \propto (\rho)^{-1}$ to estimate that ${\ell_{sf}}^{Ir} \propto \frac{1}{2.5}/{\ell_{sf}}^{Pd}$. Thus ${\ell_{sf}}^{Ir}$ might be $\sim$ 10nm. An $n \leq 18$ can have t_{Ir} comparable to its spin diffusion length. However we grow almost all of our samples with $n > 20$, with only a few below that range. Therefore we ignore any deviation associated with small n. The equations in Section 2.1.1 are thus used for our samples. We aim to show that $A\Delta R$ (ie the CPP MR) in our samples, with the F=Co layers separated by a total N layer thickness of 360nm, is insignificant compared to the total

specific resistance of the sample.

We will calculate the following:

1) AR(AP) for Nb(150nm)/Cu(10nm)/Co(10nm)/[Ir/Pd]$_n$(360nm)/ Co(10nm)/Cu(10nm)/Nb(150nm): Using the equations from Section 2.1.1, the AR(AP) for N=[Ir/Pd]$_n$ insert is given by

$$AR(AP) = 2AR_{Co/Nb} + 2\rho_{Co}{}^{*}(10nm) + [AR_{Co/Ir}{}^{\uparrow} + AR_{Co/Pd}{}^{\downarrow}]/2 + \rho_{Ir}(360nm)/2 + \rho_{Pd}(360nm)/2 + n2AR_{Ir/Pd} \tag{2.33}$$

$2AR_{Nb/Co} = 6 \pm 1 f\Omega m^2$ is the interface specific resistance of two Nb /Co interfaces, determined in Fierz et al [28]. The Cu next to the superconducting Nb becomes superconducting due to proximity effect and doesn't affect $2AR_{Nb/Co}$ [28]. The resistance contributions from the 10nm of Co and 180 nm of Ir and Pd layers are determined by VdP measurements (Section 3.3.3). The values of the resisitivities are $\rho_{Ir} = 118 \pm 8 n\Omega m$ and $\rho_{Pd} = 46 \pm 1 n\Omega m$ measured at 4.2K (Table 3.4). The Co enhanced resistivity is obtained from the formula $\rho_{Co}{}^{*} = \frac{\rho_{Co}}{1-\beta^2} = 63 \pm 13 n\Omega m$ where $\rho_{Co} = 53 \pm 5 n\Omega m$ and $\beta = 0.46$ [59]. These values of resistivities differ slightly from [60] but they are compatible. The variation is due to additional films used to obtain the average resistivities for the present thesis. ρ_{Pd} used in [60] was obtained from prior results [25] [62]. Based on the studies of other metal pairs [38] [61] [62]–[73], we approximate $2AR_{Co/N=IrorPd}{}^{*} = (AR_{Co/Ir}{}^{\uparrow} + AR_{Co/Pd}{}^{\downarrow}) \approx 1 f\Omega m^2$. This value is a small enough fraction of the total AR that its precise magnitude is not crucial.

Finally, using the above values for the individual terms, we obtain an $AR(AP) =$

$36 \pm 5 f\Omega m^2$ for n=0. Since AR(AP) increases linearly with n (until saturation of AR(AP) for high enough n at which the Ir/Pd bilayer interfaces overlap), the value of $A\Delta R$ for n =0 is the maximum value of $A\Delta R$. Its value decreases for n>0 (See Chapter 4).

2) To show that $A\Delta R \ll AR(AP)$ for n=0:

From Equations 2.6 and 2.7 and using the relations in Section 2.1.1, we get

$$A\Delta R = 4\frac{[\beta_{Co}{\rho_{Co}}^* t_{Co} + \gamma_{Co/N=Ir\ or\ Pd} {AR^*}_{Co/N=Ir\ or\ Pd}]^2}{AR(AP)}. \tag{2.34}$$

$\beta_{Co} = 0.46$ [59] and not knowing the exact value for $\gamma_{Co/N=Ir\ or\ Pd}$, we can approximate it by a typical γ value of 0.5. Using n=0, we get $A\Delta R \approx 0.01 f\Omega m^2$.

Hence the minimum value of AR(AP) $\gg$ maximum value of $A\Delta R$. $A\Delta R$, being an insignificant fraction of the AR(AP), can therefore be neglected and we can safely approximate the total specific resistance of the multilayers, $AR_T \approx AR(AP)$. In this case, the two current series resistor model reduces to an equivalent one current series resistor model. Figure 2.3 shows that R for a typical multilayer (in this case with n=100) is independent of H, with only about 0.03% variation from H= -1000 Oe to 1000 Oe. Such a variation is only a small fraction of the uncertainty in AR which is mostly contributed by the uncertainty in A.

2.3.1.2 Landauer Büttiker Scattering Formalism to calculate Specific Interface Resistance of Non-Magnetic metals:

This section closely follows [74][75][76]–[79]. We first briefly describe the basis of the theory used by our collaborators in the double blind study of $2\mathrm{AR}_{Ir/Pd}$ (specific interface resistance) in Chapter 4.

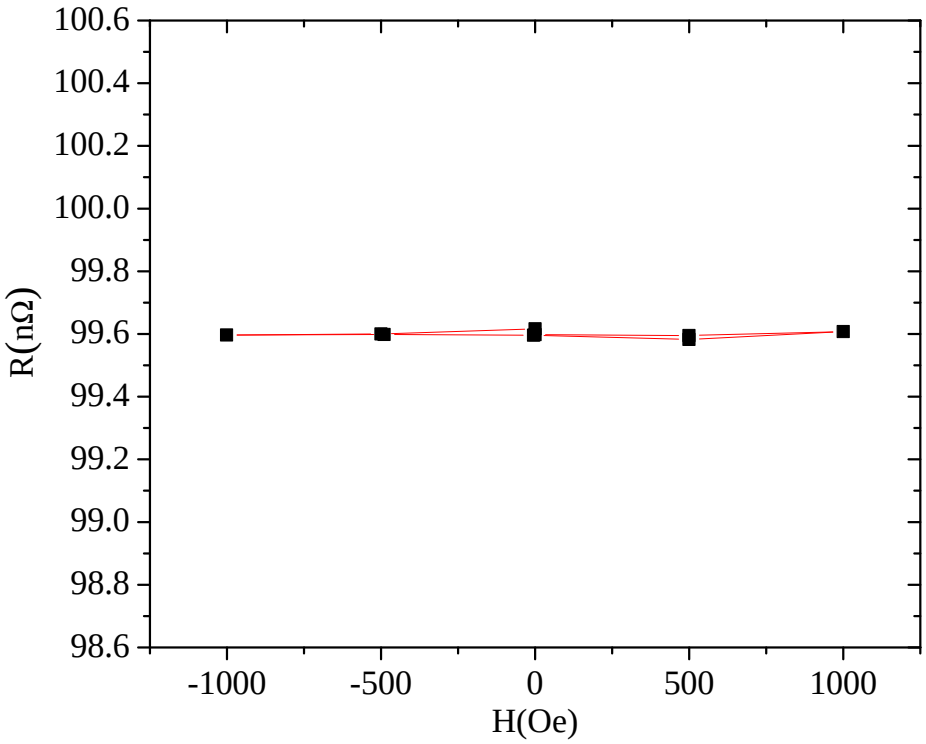

Figure 2.3: AR vs H for n =100. The variation in R is very small $\sim 0.03\%$.

We saw in Section 2.1, about the 2CSR model, how to separate the contributions to the AR of a multilayer from the bulk metals and from the interfaces.

Free electron models serve mainly to define the parameters to be determined by experiment and calculations. However free electron models describing the interface resistance through disorder and interdiffusion have limited scope since they neglect one of the most important feature of transition metals, their complex electronic structure. An important step forward in calculating the interface resistance was made by Schep et al[74], who applied the Landauer Büttiker scattering formalism with the following framework.

1) The full electronic band structure is calculated from first principles.

2) The resistor model is derived.

3) No-free parameter estimates of the interface specific resistances are made.

We will begin with a brief description of the Landauer scattering formalism developed in 1957, followed by its improved version developed by Büttiker, Landauer Büttiker formalism.

In 1957 Landauer developed a scattering theory of transport in mesoscopic systems. In this theory, electrons injected into a sample from a contact reservoir on the left are drained by a contact reservoir on the right. The conductance of electrons is determined by the transmission probability of electrons between Bloch states. The Landauer conductance for a single channel waveguide is given as

$$G^L = \frac{e^2}{h}\frac{T}{1-T} \tag{2.35}$$

where T is the transmission probability of electrons from a $k_{||}$ state (k component parallel to the interfaces) on the left to $k'_{||}$ state on the right. Later Büttiker improved the expression for conductance to obtain the Sharvin resistance if the transmission probability tends to 1. The Landauer Büttiker conductance expression for multiple channel electron transport is given as

$$G^{LB} = \frac{e^2}{h} \sum i\sigma,j\sigma' T_{i\sigma,j\sigma'} \tag{2.36}$$

where $T_{i\sigma,j\sigma'}$ is the transmission probability of an electron entering a scattering region in transverse mode i and spin state σ that is scattered into a transverse mode j and spin state σ'. The Landauer Büttiker scattering formalism has been used to describe the conductance of electrons in magnetic multilayers. The transmission probabilities are calculated using first principles full electronic structure calculations. Here we first present the studies in [74][75][76], where G^{LB} was calculated for single specular interfaces, i.e. interfaces in which the $k_{||}$ component of electron momentum is conserved. Later in this Section we will briefly discuss the calculations in [77]–[79], which were extended to disordered interfaces, i.e. interfaces where the $k_{||}$ component is not conserved.

Schep et al [74] calculated the scattering across a single interface using first principles to avoid arbitrary fitting parameters. They also use a simple model of random matrix theory to describe the diffusive transport in the bulk. To calculate the interface resistance, they assumed a single multilayer period grown along the z axis with interface planes, named L and L′. The scattering properties of a single interface are used as the boundary conditions in the semiclassical Boltzmann equation for transport of electrons between adjacent interfaces. Under the influence of a weak field the deviation in the distribution function ($f_{L,i}{}^{\pm}$) at the

plane L from the equilibrium distribution function ${f_{L,i}}^0$ is given by

$$ {f_{L,i}}^{\pm} = {f_{L,i}}^0 + \delta(\epsilon_{L,i} - E_F)[\mu_L - \mu^0 + {g_{L,i}}^{\pm}] \tag{2.37} $$

where + and signs indicate the right and left going states along the z axis at the interface, respectively. The index i is a notation which indicates the component of the bulk Bloch vector parallel to the interface at L, $k_{||}$. $\epsilon_{L,i}$ is the energy of the i^{th} state at L and similar to Section 2.2 , $(\mu_L - \mu^0)$ and ${g_{L,i}}^{\pm}$ represent the isotropic and anisotropic deviations of the chemical potential respectively.

The distribution functions at the planes L and L′are connected by the following equations.

$$ {f_{L,i}}^{+} = \sum\nolimits_{j\in L} (T_{L,L'})_{ij} {f_{L,j}}^{+} \sum\nolimits_{j\in L'} ({R'}_{L,L'})^{ij} {f_{L',j}}^{-} \tag{2.38a} $$

$$ {f_{L,i}}^{-} = \sum\nolimits_{j\in L} (R_{L,L'})_{ij} {f_{L,j}}^{+} \sum\nolimits_{j\in L'} ({T'}_{L,L'})_{ij} {f_{L',j}}^{-} \tag{2.38b} $$

The terms $(T_{LL'})_{ij}$ and $(R_{LL'})_{ij}$ represent the transmission and reflection probabilities of electrons from state i to state j. By combining the boundary conditions between planes L and L′and the boundary conditions between L′and another plane L″, the boundary conditions between L and L″can be obtained. Diffusive scattering in the bulk is incorporated by assuming isotropic mixing of all the k states within the bulk. The transmission and reflection probabilities are given by

$$ T_{ij} = {T'}_{ij} = \frac{1}{N}\frac{1}{1+s} \tag{2.39a} $$

$$ R_{ij} = {R'}_{ij} = \frac{1}{N}\frac{s}{1+s} \tag{2.39b} $$

where $s = e^2\rho N/Ah$, N being the number of conduction channels and ρ the resistivity in the bulk. They found that the parameter s, which describes the strength of diffuse scattering, does not enter the final expression for the interface resistance, so the interface resistance remains parameter free. By solving for the case of an infinite A/B multilayer with periodic boundary conditions, the interface specific resistance contribution is obtained in terms of N_A and N_B, the number of conducting channels in metals A and B and the transmission probability across the interface of A and B. The final expression for interface resistance (Equation 2.40) resembles the expression for the interface resistance of a resistor model. The resistor model is thus obtained in the case of complete diffusive scattering in the bulk with no phase coherence.

$$AR_{A/B} = \frac{Ah}{e^2}[\frac{1}{\sum ij T_{ij}} - \frac{1}{2}(\frac{1}{N_A} + \frac{1}{N_B})] \tag{2.40}$$

The calculation for the specific interface resistance by Schep et al[74] is applicable to both specular and diffusive interface scattering and general band structure of metals on either side of the interface. In their calculations, Schep et al neglected interface roughness by assuming ideal interfaces with specular scattering. Their calculations for the Co/Cu pair were compared with experimental values of Co/Cu for (100) and (111) planes at the interfaces (Table 1 in [74]). The comparisons clearly showed that specular scattering at the interfaces combined with ballistic bulk scattering didn't agree with the experimental results. The case of diffusive scattering in the bulk combined with specular scattering at the interfaces, however, gave better agreement with the experimental result. Schep [74] also states that

> We cannot conclude, however, that interface roughness is negligible, since it may be instrumental in achieving the diffusivity which we here attribute to the bulk material.

Disordered interfaces were studied by Xia et al [79][78] in multilayers of Co/Cu, Fe/Cr and Ag/Au layered systems. Interface disorder was modeled into the system via lateral supercells. The transmission and reflection probabilities across the interfaces were calculated using surface Greens function with a linear muffin tin orbital basis. The electronic structure was calculated self-consistently in the local density approximation. The disorder is modeled by randomly distributing atoms of the two metals, on either side of the interface, in the lateral supercells. The potentials for the disordered layers are calculated self-consistently in the CPA (Coherent Potential Approximation) approximation. The conductance in a disordered system is a sum of a ballistic transport component ($k_{||}$ is conserved in the transmission matrix) and a diffusive transport component ($k_{||}$ is not conserved in the transmission matrix). In disordered interfaces, electrons undergo mainly forward scattering which reduces the ballistic transport component but at the same time increases the diffusive component. The strong diffusive scattering also reasonably explains why the resistor model remains valid even for very thin metal layers between interfaces where the bulk scattering should not be important. Very thin metal layers compounded with specular scattering at interfaces should lead to quantum coherence in the layers where the resistor model ceases to remain valid. Xia et al did calculations for interface intermixing of several random distributions of the two metals including a 50%-50% random alloy with an estimated thickness of 2 layers [79]. The results for the different multilayers are summarized in Table 1 in Xia et al [78].

The studies by Xia et al[78][79] is yet another proof that the Valet Fert model is a good

approximation to CPP transport. The experimental results for the specific interface resistances, based on the two current series resistor model agree well with the specific interface resistance calculations with real band structures for metallic pairs (shown in Table 4.1) with closely matching lattice parameters and lattice structures. In Chapter 4 we will see the calculations extended to Ir/Pd multilayers with further alterations in the electronic structure calculations intended to improve the method and obtain better band structures.

2.3.2 Determination of spin diffusion length of an N metal and at an N/Cu interface

This section is aimed to describe the theoretical background of our experiment to determine spin relaxation in non-magnetic (N) metals and at non-magnetic interfaces (N/Cu) using CPP S EBSV samples. The discussion closely follows Park et al [63].

The motivation of the design of the sample structure is to be able to determine the effect of spin flipping behavior of a desired metal. The basic geometry of the sample structure used for this technique is a multilayer structure given by AF/F/Cu/X/Cu/F. Here AF is an antiferromagnet such as FeMn, F is a ferromagnet such as Permalloy (Py = $Ni_{84}Fe_{16}$) and X is the metal/alloy of interest, inserted in the middle of the Cu layers. The spin relaxations caused by the growing N layer or increasing number of N/Cu interfaces causes the $A\Delta R$ to decay. The design of the spin valve structure is motivated by the following reasons. The magnetization of the Py layer adjacent to the FeMn gets "pinned" because of exchange biasing with the neighboring FeMn. The "pinned" Py layer is magnetically decoupled from

the "free" 24nm Py layer by the presence of the 20nm of Cu in between. If there is no N insert in the sample, there is no spin flipping at N/Cu interfaces or in bulk N. $A\Delta R$ is then maximum. As an insert N is introduced and its thickness is increased, $A\Delta R$ will decrease. As the insert thickness t_N increases, the decay in $A\Delta R$ based on the VF model is due both to the added resistivity and spin relaxation due to the insert. The Py layers are maintained at a chosen fixed thickness $t_{Py} \gg {\ell_{sf}}^{Py}$ since ${\ell_{sf}}^{Py}$=5.5nm so that the $A\Delta R$ is insensitive to sample fluctuations of t_{Py} as we discussed in the end of Section 2.2.

In practice, a more rigorous calculation is performed. It is based on solving the Equations for the spin dependent and spatially varying chemical potentials and current densities for each layer in the sample (Section 2.2), followed by matching them at the boundaries. The numerical calculations are made simpler due to the symmetrical nature of the sample structure. In the present section we will briefly discuss an approximate VF model that describes the essential physics of determining the spin flipping behavior in a metal/alloy and its interface with Cu.

With the basic Py based EBSV structure introduced above, we can use two techniques with different kinds of inserts to determine the spin flipping behavior of a bulk metal (or alloy) or spin flipping at an interface of a metal(or alloy)with another metal such as Cu.

In the first technique, where we are interested in the spin flipping behavior in the bulk of a metal or alloy, a thickness t_N of the metal of interest is inserted in the middle of the Cu layer. The AΔR decays initially as a result of the added specific resistance and exponential decay caused by spin flipping at the N/Cu interfaces, followed by a decay due to added specific resistance and spin flipping exponential decay in the bulk N layers. As long as the thickness of the bulk N layer, t_N, is less than the spin diffusion length, ${\ell_{sf}}^{N}$, the contribu-

tion from the specific resistance increases linearly until $t_N > \ell_{sf}{}^N$. In that case, the specific resistance contribution becomes a constant and the only contribution comes from the spin flipping in the bulk of the N metal, which decays exponentially at the rate of $-t_N/\ell_{sf}{}^N$.

In the second technique, where we are interested in spin flipping behavior of the N/Cu interface, we insert M bilayers of N/Cu in the middle of the Cu in the Py based EBSV structure. As the number of bilayers M, is increased, the number of N/Cu interfaces increases and $A\Delta R$ decays with increasing $M(2AR_{N/Cu})$, due to both the added specific interface resistance of M bilayers and an exponential decay due to spin flipping at the interfaces. The spin diffusion length is obtained from the exponential decay in $A\Delta R$ which decays at the rate of $-2Mt_I/\ell_{sf}{}^I$ ($=-2M\delta$), where t_I is a fully formed sputtered N/Cu interface thickness (3-4 ML [64]) and $\ell_{sf}{}^I$ is the spin diffusion length of the interface. This technique of introducing M bilayers is useful when the spin relaxation at the N/Cu interfaces is not too strong. In 2000, Park et al [63] studied the bulk spin flipping behavior in various metals such as CuPt, Ag,V,Nb,W, and FeMn. Figure 2.4 [63] shows the final graph of the decay in $A\Delta R$ with increasing t_N thickness of the inserts. For all metals, except FeMn, the spin flipping at the N/Cu interfaces is weak as evidenced by the slower rate of $A\Delta R$ decay, while the interfaces are forming ($t_N \ll t_I$), for all metals except FeMn. In FeMn, the $A\Delta R$ drops by almost a factor of 400 by the time the t_{FeMn} is $\sim$ 1nm. For these other metals, the slower decay is due simply to the additional resistance from the growing interfaces with a nominal interface spin flipping. For two of the N metal inserts CuPt/Cu and Cu/Ag, the initial decay in $A\Delta R$ is especially weak. This is because there is essentially no interface between CuPt and Cu and the independently measured Cu/Ag interface resistance is very small [87]. The N/Cu interface spin flipping for all these metal inserts with weak interface spin flipping can be

determined using the technique of M N/Cu bilayer inserts. However we cannot use the same technique for FeMn. Figure 2.4 clearly shows that by the time only two interfaces are formed, the value of AΔR has decayed so much that measuring AΔR for more than 2 interfaces is not feasible.

We now look to an approximate model to treat the interface and bulk spin flipping in metals such as FeMn, where the spin flipping at the interface with Cu is so strong. We first treat the situation of spin flipping at the interfaces of N/Cu while they are still *forming*. Figure 2.5a shows a schematic diagram where the sputtered thickness t_N of the insert N is $< t_I$ of a fully formed interface. In this case the nominal sputtered metal t_N intermixes with the Cu on either side and the total effective interface, shown by the shaded region in Figure 2.5a, consists of a 50%-50% alloy of N/Cu whose thickness is $2t_N$. This region grows until $2t_N \sim 2t_I$ where t_I is the sputtered interface thickness expected to be $\sim$ 3-4ML [64]. The approximate VF equation for decay in AΔR is given by the following equation.

$$\begin{aligned} A\Delta R &\propto exp(-\frac{2t_N}{2t_I}(\frac{2t_I}{{\ell_{sf}}^I}))(\frac{1}{AR_0 + AR_N}) \\ &\propto exp(-\frac{2t_N}{2t_I}(2\delta))(\frac{1}{AR_0 + AR_N}) \end{aligned} \tag{2.41}$$

Here AR_0 is the total specific resistance as contributed by the sample minus the alloyed region, and ${\ell_{sf}}^I$ and AR_N are the assumed interface spin diffusion length and specific resistance due to the insert N, respectively. $\delta = t_I/{\ell_{sf}}^I$. If the growing nominal interface thickness is labeled as $t_I{}'$, then the value for AR_N is given as:

(i) $AR_N = \rho_{N/Cu} 2t_N$ for $t_N = t_I{}' \ll {\ell_{sf}}^I$ where $t_I{}'$ is still less than t_I.

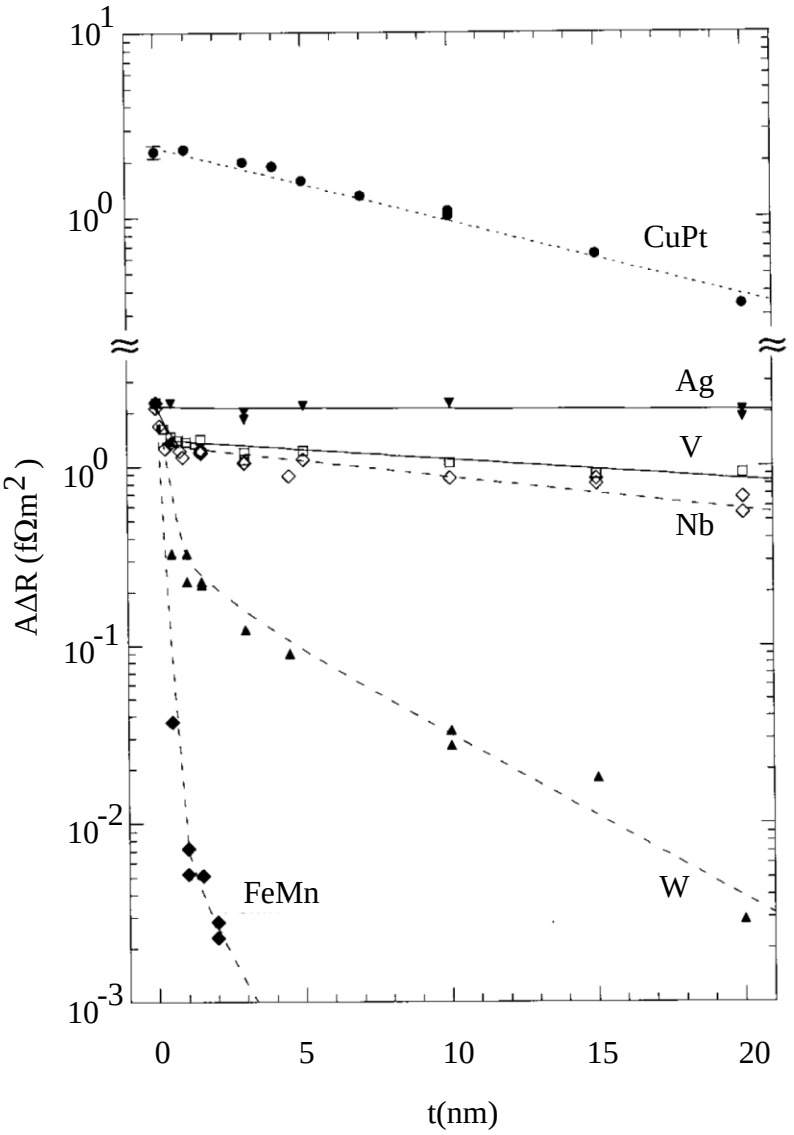

Figure 2.4: $A\Delta R$ versus t of various N inserts.[63]. Note that all metals/alloys, other than FeMn, undergo nominal AΔR decay for small t_N, indicating weak interfacial spin flipping. In the case of FeMn, however, the initial decay is almost by a factor of 400 which indicates a strong spin flipping at the FeMn/Cu interface. The growing interface plays a strong role in spin relaxation and is treated independently in Equation 2.41.

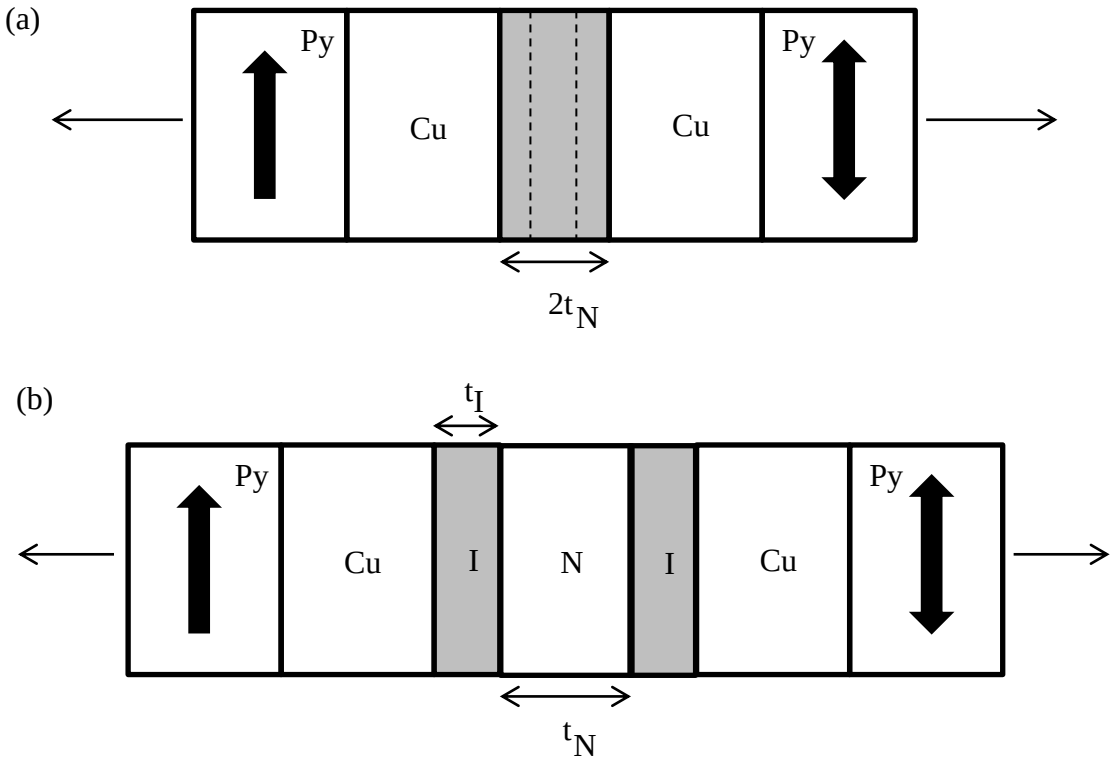

Figure 2.5: Schematic of the modified model for the case (a) when the interfaces N/Cu are not fully formed yet. Shaded region shows 50%-50% alloy of N-Cu and dotted lines show nominal sputtered N layer thickness. (b)The fully formed interface has thickness t_I and the bulk, minus any mixture with Cu, has a thickness t_N.

(ii)$AR_N = \rho_{N/Cu} 2{\ell_{sf}}^I$ for $t_N = t_I' \gg {\ell_{sf}}^I$ where t_I' is still less than t_I.

Here $\rho_{N/Cu}$ is the resistivity of the interfacial 50%-50% N-Cu alloy which we take equal to ρ_N. Such an assumption for $\rho_{N/Cu}$ is reasonable for N = AF (antiferromagnet) since in this case $\rho_N \gg \rho_{Cu}$.

After the two interfaces have fully formed, ie, $2t_N \sim 2t_I$, the bulk N metal begins to grow as shown in Figure 2.5b. The additional decay in $A\Delta R$ is then dominated by the bulk N metal and the approximate VF equation for decay in $A\Delta R$ is given by:

$$A\Delta R \propto exp(-2\delta) exp(-\frac{t_N}{{\ell_{sf}}^N})(\frac{1}{AR_0 + AR_N}) \tag{2.42}$$

The value of AR_N is now given as:

(i) $AR_N = \rho_N t_N + \rho_{N/Cu} 2{\ell_{sf}}^I$ for $t_N \ll {\ell_{sf}}^N$

(ii) $AR_N = \rho_N {\ell_{sf}}^N + \rho_{N/Cu} 2{\ell_{sf}}^I$ for $t_N \gg {\ell_{sf}}^N$.

Chapter 3

Sample Preparation and Fabrication: CPP Sample Structures, Preparation and Measurements.

In this section we describe the structure, preparation and measurement of all samples used in the studies done in this thesis. This chapter is divided into 3 main sections.

3.1 Description of the types of samples used in this thesis.

3.2 Description of the sputtering system used in metal deposition.

- Low temperature Sputtering system.
- High temperature Sputtering system.
- Sample Patterning Techniques.

3.3 Measurement techniques.

- Liquid Helium temperature CPP resistance measurement.
- Sample Area measurement.
- Resistivity measurements.
- Magnetization measurements.
- Energy Dispersive Spectroscopy.

3.1 Types of samples in this Thesis

Prior to describing the details of the sample preparation, fabrication and analysis, we briefly describe the sample structures used in this thesis. All samples are deposited on a 0.5" X 0.5" dimension substrate. We use Si substrates for the Antiferromagnet (IrMn and FeMn) and the Ir/Pd Interface Resistance studies and MgO single crystal substrates for the Heusler alloy study. The first step in the sample preparation process involves cleaning the substrates.

1) We clean the Silicon Si (100) orientated substrates sequentially with alconox, acetone, Isopropyl Alcohol (IPA), and De-ionized water (DI) water in an ultrasonic cleaner and blow dry with Nitrogen. The cleaning process ensures that the substrate surface is free of grease and contaminants.

2) Since the MgO (001) single crystal substrates are pre-cut, pre-cleaned and sealed in Argon by the manufacturer, we don't clean them further.

We deposit the desired multilayered sample structure on the substrates using the deposition processes described in Section 3.2. The multilayered structures used are described as follows.

3.1.1 Nb Superconducting cross- strip multilayer to study Pd/Ir:

The multilayer structure is:
Nb(150nm)/Cu(10nm)/Co(10nm)/$[Pd(t)/Ir(t)]_n$/Co(10nm)/Cu(10nm)/Nb(150nm). The metals are deposited using the Low Temperature Sputtering system. The total Pd and Ir thickness is kept the same at $n(2t) = t_T = 360nm$. Samples are made with varying number of bilayers (n).

3.1.2 Nb Superconducting cross-stripped EBSV structure for the study of antiferromagnet N = IrMn or FeMn:

The EBSV structure is Nb(150nm)/Cu(10nm)/FeMn(8nm)/Py(24nm)/Cu(10nm)/N(t_{AF}) Cu(10nm)/Py(24nm)/Cu(10nm)/Nb(150nm).
The metals are deposited using the Low Temperature Sputtering system. Samples are made with a variable t_{AF} of N.

3.1.3 Micrometer Pillars of Hybrid Spin Valve structures for study of CFAS Heusler Alloy:

In this project, we have made different kinds of samples to obtain epitaxial CFAS necessary to display its half metallicity. In this section we discuss the fabrication of one of the sample structures. The other sample structures are discussed in detail in Chapter 6. The micropillar fabrication procedure is identical in all the sample structures. The difference lies in the metal layers grown under the epitaxial CFAS using high temperature sputtering.

The sample structure we will discuss here is:

Nb(001)(150nm)/Cu(001)(10nm)/CFAS(001)(t)/Cu(25nm)/Py(24nm)/Cu(10nm)/

Nb(25nm)/Au(15nm)/Nb(150nm)/Au(5nm)

The $Co_2Fe(Al\,Si)_{0.5}$ (CFAS) alloy needs to be grown epitaxially to display its half metallic property. Epitaxial growth requires high temperatures to provide depositing atoms surface mobility to nucleate on the underlying lattice structure. CFAS has a cubic structure. Thus epitaxial growth of CFAS will be best on metal underlayers with a cubic structure such that, given a desired crystal orientation, the length between two surface atoms of the substrate and the subsequent layer are similar. Hence even if the lattice parameters of two adjacent layers growing in the same crystal orientation, don't match, they can grow with minimum strain if the layers are rotated to match the similar lengths between surface atoms. Hence all the underlayers of CFAS should also be grown epitaxially as well. The epitaxial layers are grown at high temperature using the high temperature Sputtering system. The layers following CFAS are then grown at about room temperature. We then pattern six micrometer pillar samples on each chip, with diameter=50μm, using Optical Lithography and Ion

Milling [81] [80]. Finally a top electrode is deposited using Low Temperature Sputtering.

From here on for the CFAS study, a sample refers to a single micrometer pillar and a chip refers to a set of six pillars patterned on a single chip. For all other projects, there is only one CPP S sample per chip/substrate; a *sample* there refers to a single measurable CPP S structure.

3.2 Metal Deposition Processes:

We deposit metals using a Sputtering system described in detail by Slaughter et al [29] and Lee et al [30], except that two small guns [82] have been added to the four larger guns in the system that they describe.

Sputtering is a process in which highly energetic inert gas ions collide with a target material that releases atoms. The target atoms released are deposited onto a substrate. A tungsten filament acts as a cathode which emits electrons when heated by a current flowing through it. The emitted electrons are accelerated, parallel to the target surface, towards the anode shown in Figure 3.1. High purity Ar (Argon) gas is introduced near the target and the emitted electrons ionize the gas, creating plasma. These positive Ar ions scatter off the target surface, maintained at a certain negative voltage, releasing target atoms that get deposited on a substrate positioned above the target. Sputtering is done in purified Ar gas at typically a pressure of $\sim$ 2.5 X 10^{-3} Torr. Magnetron sputtering uses a magnetic field near the target to trap secondary electrons near the target surface. The field forces the electrons to follow helical paths thereby producing more Ar ions. The ionized Ar ions are

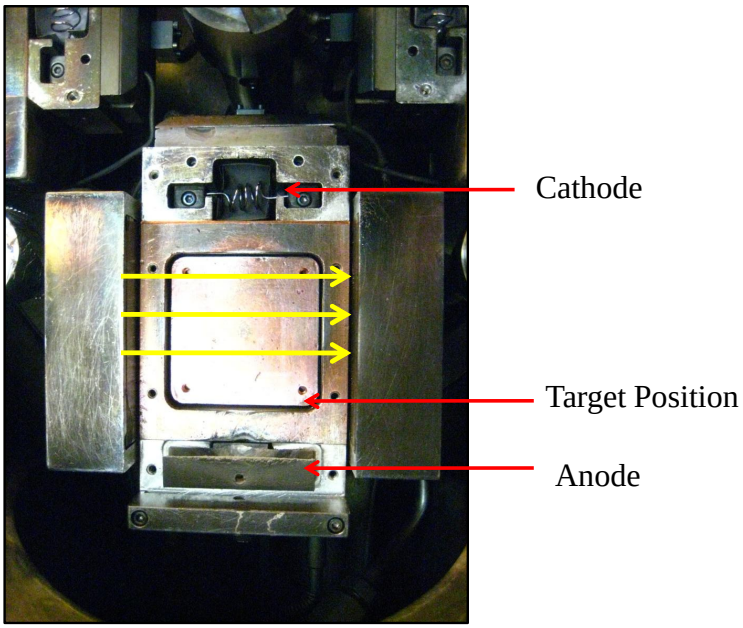

Figure 3.1: Shows one of the large Guns in the Sputtering chamber. The target, anode and cathode arrangement in the sputtering chamber. The yellow arrows represent the magnetic field lines of the magnetron arrangement.

heavy enough to not be deflected by the magnetic field.

Our sputtering chamber is equipped with six guns to accommodate six targets, four triode sputtering guns with 2.25" diameter X (0.25" or 0.125") thick and two magnetron guns with 1" diameter X 0.125" thick targets. Having the capability of loading upto 6 targets, permits deposition of multilayers with six different metals/alloys. Each target has its own mounting parts (gun part) and a chimney to prevent contamination from other target materials. All the target gun systems are water cooled to prevent overheating during the sputtering process. Figure 3.2 shows the 6 gun assembly of the sputtering system. A shutter plate right above the targets, with four open positions that are four fold symmetric, can be rotated to

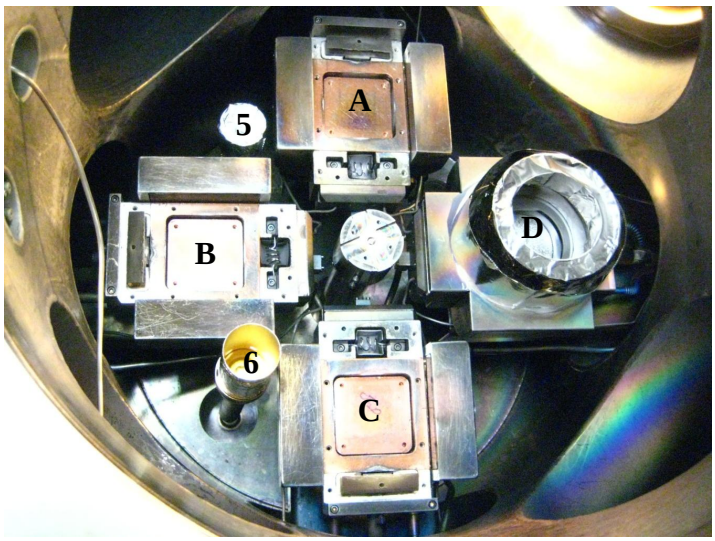

Figure 3.2: Six Gun assembly. A,B,C and D are big Guns. Here Gun D is loaded with a Nb Target. 5 and 6 are small DC Magnetron Guns. Here Gun 6 is loaded with Au. The chimneys around the loaded targets prevent cross-contamination during sputtering.

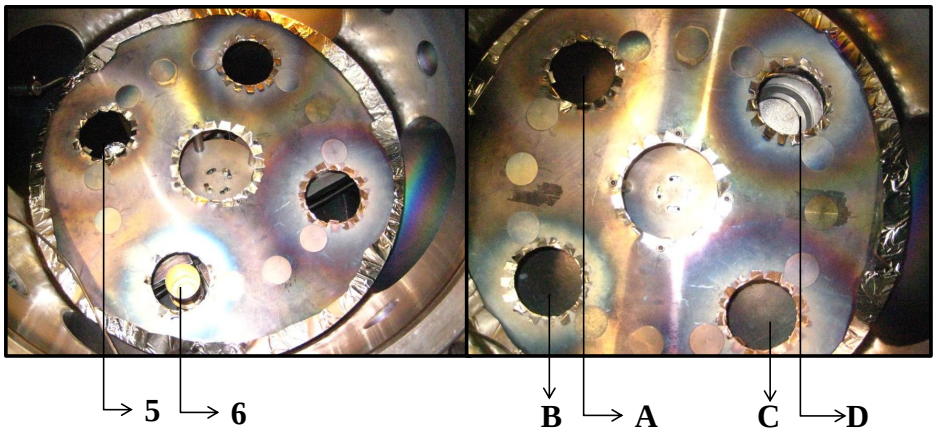

Figure 3.3: The Shutter plate positioned above the targets. (a) Shutter 2 position with open small guns. (b) Shutter 1 position with open large guns.

two positions; either all open big targets (Shutter 1 position) with closed small targets, or just the two small targets open (Shutter 2 position)Figure 3.3a and b. The movement of the Shutter plate is controlled by a stepper motor (Compumotor M106-178) programmed via Labview.

We take multiple measures to ensure the purity of the sputter chamber for a clean deposition of metals.

1) Users are required to wear gloves at all times, to prevent transfer of hand oils to the chamber or any part used in the Sputter system.

2) The substrate holders (made of Aluminum) Figure 3.4 and masks (Stainless Steel) Figure 3.5 are cleaned before each sputter run with a 1:3 Nitric Acid: Water solution. The masks are further treated by adding a few drops of Hydrofluoric Acid to the 1:3 solution. The chemicals etch away unwanted metals deposited on the holders and masks from previous runs.

3) To reduce contaminants (water vapor, helium, nitrogen, carbon dioxide, oxygen, etc), the sputtering chamber is pumped down to high vacuum $\sim$ 2-3 X 10^{-8} Torr. To achieve high vacuum, a roughing pump initially reduces the pressure in the chamber down to $\sim$2 X 10^{-1}Torr. Then a cryopump pumps down the chamber to $\sim$2-3 X 10^{-8} Torr. Use of a cryopump avoids oil contamination. The cryopump is regenerated at elevated temperatures, to release trapped gasses, every 3 to 4 sputter runs to improve its pumping performance.

4) The four big guns are fitted with Copper gaskets while the top of the chamber and the two

smaller guns are fitted with Viton o-rings. The gaskets and o-rings are high temperature resistant ($<550^0$C for Copper and $<200^0$C for Viton) and provide high vacuum seal. Ultra high vacuum $< 10^{-9}$ Torr uses Copper gaskets.

5) To clean the chamber surfaces of adsorbed gasses, it is baked for ∼8-10 hours to temperatures of about 80^0 C while pumping down. The presence of the Viton o-rings and other factors such as moisture in the chamber increase the pumping duration. It takes normally two nights, including the baking period, for the chamber to pump down to ∼ 2-3 X 10^{-8}Torr.

6) The chamber is equipped with a cold trap (Meissner Trap). Right before the deposition process, the cold trap is filled with liquid Nitrogen, thereby freezing out any residual water vapor in the chamber. This process further reduces the pressure by typically about half. The trap is continuously fed with Liq. Nitrogen during Sputtering.

7) Argon gas, ionized to create the plasma, is purified by removing O_2 and N_2 by reaction with a hot Ti based alloy [29] using a commercial gas purifier (Matheson Hydrox Purifier 8301). The pressure inside the chamber with the Ar gas is maintained at ∼2.5 X 10^{-3}Torr, at which sputtering occurs.

The Sputtering assembly is equipped with two kinds of chamber tops. One kind is used for metal deposition at low temperatures (-30^0C to 30^0C). The other is used for high temperature (Room Temperature to 1500^0C) deposition. The details of the two tops are given in the following sections.

3.2.1 Low Temperature Sputtering:

Low temperature sputtering is not epitaxial, leading to close packed layers such as (111) FCC and (011)BCC. The low temperature top includes:

1) A Substrate Position and Masking Aparatus (SPAMA) plate that has 8 open slots to house substrates. It is connected to a stepper motor whose movement is controlled by a computer using a Labview Program. It is usually maintained at a distance of ∼11cm above the targets.

2) Two Film Thickness Monitors (FTM) that are located on the SPAMA plate. A FTM consists of a quartz crystal whose oscillating frequency changes with the change in surface mass. The FTM is moved over the target to deposit a metal on the FTM crystal. With the density of the metal deposited on the quartz crystal specified, a Labview program calculates and displays the sputtering rate. Given the known sputtering rates, the sputter Labview program calculates the dwell time of deposition for a known thickness of a metal during the sputter runs. The deposition rates are measured before each sample is made. The rates of the metals/alloys used in this thesis were kept fixed at the values shown in Table 3.1. The rates can be varied by varying the Target negative voltage and current.

3) To maintain low temperature of the substrates, a capillary tube passes through the cold trap containing liquid Nitrogen (Liq. N_2) and carries dry N_2 gas at $\sim$ 1000 psi pressure. The N_2 gas gets cooled by the Liq. N_2 and in turn cools the SPAMA plate. Prior multilayer depositions indicated that best reproducibility occurs for substrate temperatures between -30^0C and 30^0C.

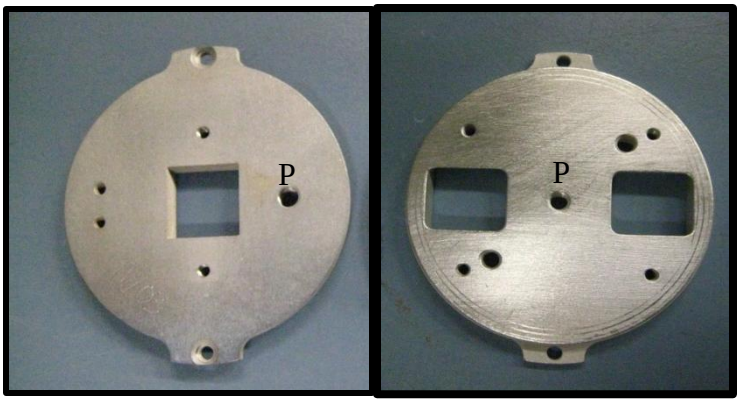

Figure 3.4: Substrate holders used in the low temperature sputtering top. (a) CPP Substrate holder. (b)CIP Substrate holder. 'P' represents the pivoting screw connection to the masks shown in the next Figure.

4) Two thermocouples monitor the temperature of the cold trap and the temperature of the SPAMA plate.

The user writes a sequence file, in the sputter Labview Program, which specifies for the computer the desired multilayer structure. When the program is run with a desired sequence file, the SPAMA and shutter plates rotate to deposit the sequence of multilayers on a chosen substrate.

The CPP mask (Figure 3.5a) comprises of 4 patterned mask settings that allow sequentially depositing the bottom Nb strip, the sample multilayer and finally the top Nb strip. A fourth setting on the CPP mask covers the sample when it is not being deposited on. A manually movable wobble stick allows the masks to be rotated without breaking vacuum. The sequence file for a desired multilayer structure is coded to include "pauses" in the program to give the user time to rotate the CPP mask using the wobble stick. For CIP samples

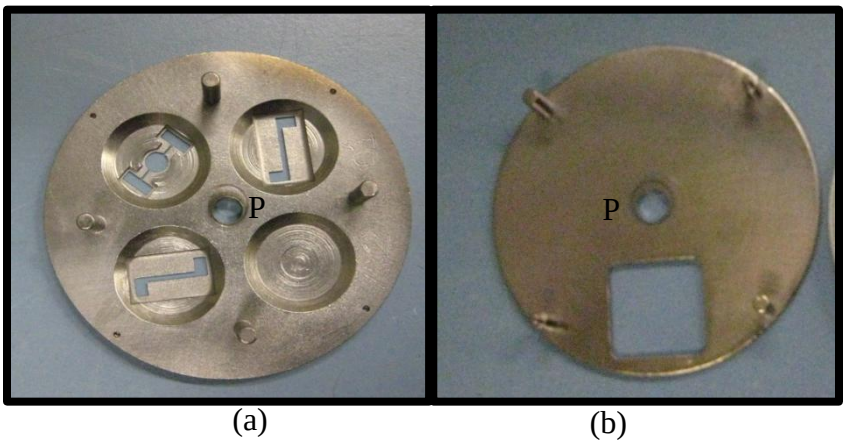

Figure 3.5: Substrate masks used in the low temperature sputtering top. (a) CPP Mask with the four positions. (b)CIP Mask with the two (open and close) positions. The pillars shown here are used to rotate the masks (about the pivot point 'P') using the wobble stick.

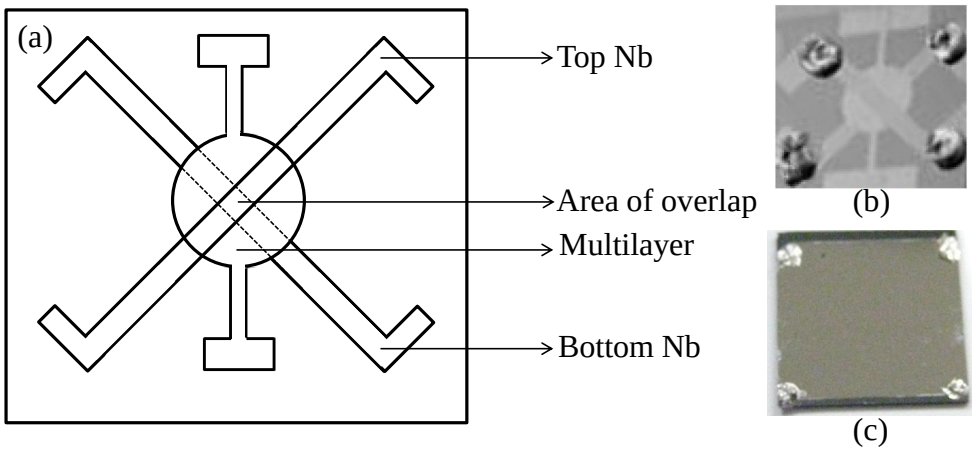

Figure 3.6: (a) Top view of CPP Superconducting cross-stripped sample. 'A' is the area of the overlap of the two superconducting electrodes. (b) Shows the image for such a sample with Nb Superconducting electrodes. The four Indium contacts are made by soldering to connect the V and I leads during measurements.(c)Image of a CIP film. The four Indium contacts are made for VdP measurements 3.3.3.

Target	Deposition Rate(Å/sec)
Nb	4.6±0.5
Py	5.0±0.2
Co	4.3±0.2
Ir	5.2±0.1
Pd	5.3±0.1
Cu (2.25" Target)	7.2±0.3
Cu(1" Target)	2.4±0.1
$Fe_{0.5}Mn_{0.5}$(2.25" Target)	4.2±0.1
$Fe_{0.5}Mn_{0.5}$(1" Target)	0.6±0.1
$Ir_{0.2}Mn_{0.8}$	3.8±0.1

Table 3.1: Sputtering Rates. The_±_ represents the variation of sputtering rates over various runs.

the mask is simply an open-close mask (Figure 3.5b). One CIP substrate holder (Figure 3.4b) can be used to deposit two separate CIP samples.

Figure 3.6a and b show a top view of a CPP sample used in the Ir/Pd and Antiferromagnetic studies. With the aid of the CPP mask, we can achieve the cross-strip pattern of the Nb electrodes with the multilayers sandwiched in between. A top view of a CIP sample is shown in Figure 3.6c.

3.2.2 Preparation of a Micrometer Pillar Sample for half metallic CPP MR Study using CFAS

For details of chip deposition (High temperature sputtering system), the reader is referred to [82]. Chip preparation for the CPP MR studies of the Heusler alloy CFAS is done differently from the low temperature sample preparation described above. The reason is that we need to grow epitaxial films of CFAS to obtain a half metallic character for the CFAS layer.

A high temperature sputtering assembly, as described in the following section, facilitates the growth of epitaxial layers during sputtering. This assembly, however, lacks the ability to change masks in situ. The substrate holder is shown in Figure 3.7a. It sits over the substrate plate with the help of 4 Molybdenum pillars at a distance of about 1 cm from the plate. The Molybdenum pillars have low thermal conductivity and thermally insulate the substrate plate during high temperature deposition on a particular substrate. The pillars prevent use of a rotating mask like the previously described CPP samples. The mask that is present can only be pulled out (open) or pushed in (closed) Figure 3.7b, ie. it is not possible to obtain a CPP S cross stripped sample using the mask shown in Figure 3.5a. To design a sample, with multilayers sandwiched in between Nb leads, we grow our multilayers on Nb and subsequently pattern micrometer pillar samples using microfabrication techniques. Our multilayer structure, sandwiched between Nb, is essentially a hybrid spin valve of the form [F1/N/F2] such as CFAS/Cu/Py ($Ni_{81}Fe_{19}$) or CFAS/Ag/Py. The fabrication of our hybrid spin valve micropillars, with Nb leads, is a multi step process summarized in the following sub sections. In Chapter 6 (Section 6.5), we will discuss the different growth recipes used to obtain epitaxial CFAS on Nb, with or without a buffering underlayer such as Cu, Ag or both. The underlying processes in all the different recipes are essentially the same, differing in only the temperatures at which they are grown. In the present section we will elaborate on one of our sample structures with CFAS grown epitaxially on Nb and Cu,

Nb(150nm)/Cu(10nm)/CFAS(t)/Cu(25nm)/Py(24nm)/Cu(10)/Nb(25nm)/Au(15nm)
/Nb(150nm)/Au(5nm).

The following subsections will describe the sample fabrication process in the order:

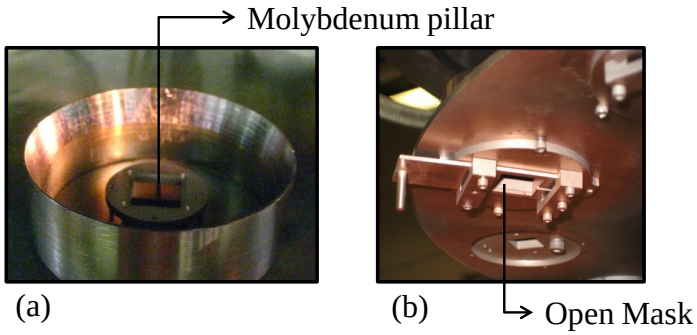

Figure 3.7: High Temperature(HT) (a) Substrate Holder showing the Molybdenum pillars thermally insulating the substrate plate from the holder. (b) Substrate Mask viewed from under the substrate plate. Here the mask is open and we make use of a movable "wobble stick" to open or shut the mask, thus protecting a chip/substrate from contamination.

3.2.2.1 High Temperature Sputtering for the desired multilayer.

3.2.2.2 Optical Lithography to pattern micrometer sized circles.

3.2.2.3 Ion Milling and SiO insulation to fabricate micropillars.

3.2.2.4 Lift off of the SiO insulation.

3.2.2.5 Ion Milling to clean the sample surface prior to top electrode deposition.

3.2.2.6 Top electrode deposition using Low Temperature Sputtering.

3.2.2.1 High Temperature Sputtering:

For the study of transport properties of CFAS, we need to grow the CFAS layer epitaxially (Section 6.5). To obtain epitaxial multilayers we require a high temperature sputtering assembly (Figure 3.8). High temperature provides surface mobility to the depositing metal atoms which leads to nucleation of those atoms on the underlying lattice structure. A

single crystal substrate is required to provide nucleation sites for subsequent layers to grow epitaxially at high temperature. We use MgO single crystal substrates in the (001) crystal growth direction. MgO has a cubic structure (lattice constant = 4.212Å). When Nb (lattice constant = 3.30 Å), Cu (lattice constant = 3.61 Å) and CFAS (lattice constant = 5.69 Å) are grown on MgO at high temperature the layers register the basic cubic structure to grow in the (001) crystal growth direction. The lattice mismatch is most likely overcome by rotation of lattice planes in the plane of the layers (Section 6.5).

In the case of CFAS grown with Nb as the bottom lead and Cu as an underlayer, X ray diffraction spectra indicated that we obtain epitaxial growth of Nb, Cu and CFAS when Nb is grown at 650^0C, Cu at $\sim 100^0$C and CFAS at 500^0C.

The assembly is equipped with two heaters. The low temperature heater can go up to 700^0C and is free to rotate 270 degrees. The high temperature heater can go up to 1200^0C. It is water cooled, which restricts its movement to ± 90 degrees. Unlike the room temperature assembly top, the substrate plate in the high temperature assembly top is not computer controlled. Therefore the sequence files are coded to include 'pauses' to manually position the substrates over the targets. The shutter plate is computer controlled to prevent unwanted depositions. The high temperature top is also equipped with a cold trap (Meisner trap) to contain liquid Nitrogen during the sputtering run, but this assembly lacks a Nitrogen gas cooling system. Hence sputtering below room temperature is not done using this assembly.

The heater temperature are monitored using thermocouples attached to them. The error in reading the temperature is large as the reading is very sensitive to the alignment of the thermocouples with respect to the heaters. For our purposes, it is desirable to calibrate the temperatures of the substrates with respect to the Voltage of the power supplies to the

Heater	Voltage(V)	Approximate Temperature
Low T	10	200^0C
Low T	13	250^0C
Low T	14	300^0C
Low T	15	400^0C
Low T	17	500^0C
Low T	18	600^0C
Low T	20	700^0C
High T	23	650^0C

Table 3.2: Calibration of heater power supply voltage to substrate temperature. Given the ambiguity of the thermocouple reading, the values are approximations.

heaters (Table 3.2). We also determined that the time a substrate takes to reach the desired stable temperature varies between 5-10 minutes after the heaters are lowered onto them.

The process for high temperature sputtering of the bottom layers is as follows:

1) The sputter chamber is prepared by loading Nb, Cu, Py and CFAS into triode guns. We load the Au target in one of the dc magnetron guns.

2) The single crystal MgO (001) oriented substrates are loaded onto the Molybdenum substrate holders.

3) The chamber is closed and pumped down until the pressure inside the chamber is 2-3 X 10^{-8} Torr.

4) The high temperature heater (HT) power supply is turned on. We make sure that the cooling water is running.

5) We let the HT heater go up to 1200^0C.

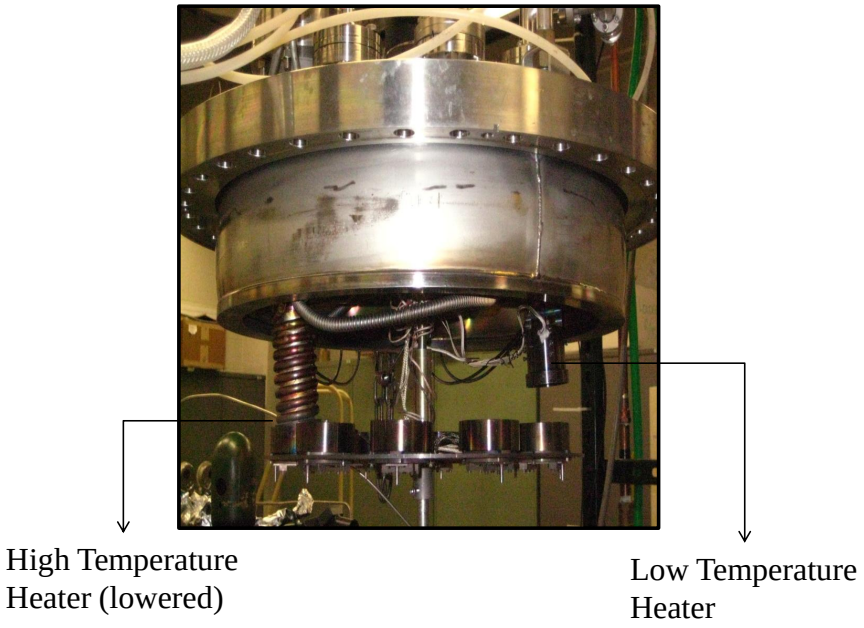

Figure 3.8: HT top Assembly showing the High Temperature heater (lowered on a sample) and the Low Temperature heater.

6) The HT heater is then loaded on the substrate and pre-deposition anneal it for ∼45 minutes. This process removes substrate roughness and surface Oxygen, making the surface clean for subsequent depositions. Pre-deposition annealing is done in vacuum to make sure that any residual material (solvents) left during preparation and polishing of the MgO substrate is removed.

7) After pre-deposition annealing of the substrates, the chamber is opened and the strip masks are mounted under the substrates. Figure 3.9a shows the image of a strip mask.

8) The system is pumped down for a day to ∼2-3 X 10^{-8}Torr (high vacuum needed for good deposition).

9) The process for starting the run is similar to that of low temperature sputtering. However there is no high pressure Nitrogen gas to cool the substrate plate.

10) The cold trap is filled and the chamber pressure is reduced further to low 2 X 10^{-8}Torr, the Low Temperature (LT) voltage is turned on and increased gradually to 17V. The temperature of the heater is maintained at ∼500^0C and it takes about 30 minutes to stabilize. The voltage for the heater temperature was calibrated separately giving 17V to reach a temperature of ∼500^0C.

11) The HT heater power supply is increased from 0V to 22V-23V. The temperature of the heater is maintained at ∼650^0C and it takes about 10 minutes to heat up. We make sure that water is turned on for cooling to prevent excessive heat loads.

12) The substrates are then ready for deposition.

13) We load (lower) the HT heater onto the substrate and wait 5 minutes before depositing a 150nm Nb layer at 650^0C.

14) The HT heater is then unloaded and we wait for 10 minutes for the substrate temperature to cool to $\sim 100^0$C. Cu grows well at temperatures less than 100^0C.

15) We deposit 10nm of Cu.

16) The LT heater is then loaded and we wait 10 minutes to let the substrate temperature reach $\sim 500^0$C.

17) We deposit t_{CFAS} (nm) of CFAS at $\sim 500^0$C.

18) Subsequently we wait for at least five hours to let the substrate cool to room temperature. This process prevents diffusion of the subsequent layers into CFAS. Liquid Nitrogen is slowly leaked into the Meisner trap to maintain cleanliness.

19) We deposit 25nm of Cu to act as a spacer layer between the CFAS and the Py layer deposited next.

20) We then deposit 24nm of Py, 10nm of Cu, 25nm of Nb and finally a 15nm Au (Gold) capping layer. Au prevents the chip from oxidizing.

21) The chip is then ready for micropillar patterning as explained below. To summarize, the multilayers deposited are: Nb(001)(150nm)/Cu(001)(10nm)/CFAS(001)(t_{CFAS})/ Cu(25nm)/Py(24nm)/Cu(10nm)/Nb(25nm)/Au(15nm). Figure 3.9b shows a schematic of the top view of our chip after sputtering. The sample pillars are patterned on the exposed region shown in Figure 3.9b.

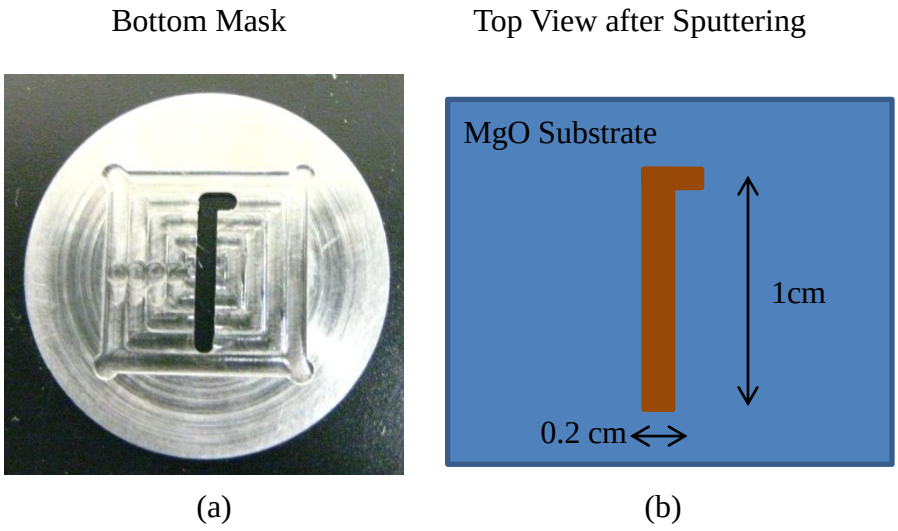

Figure 3.9: (a)Bottom Mask. (b)Chip after sputtering.

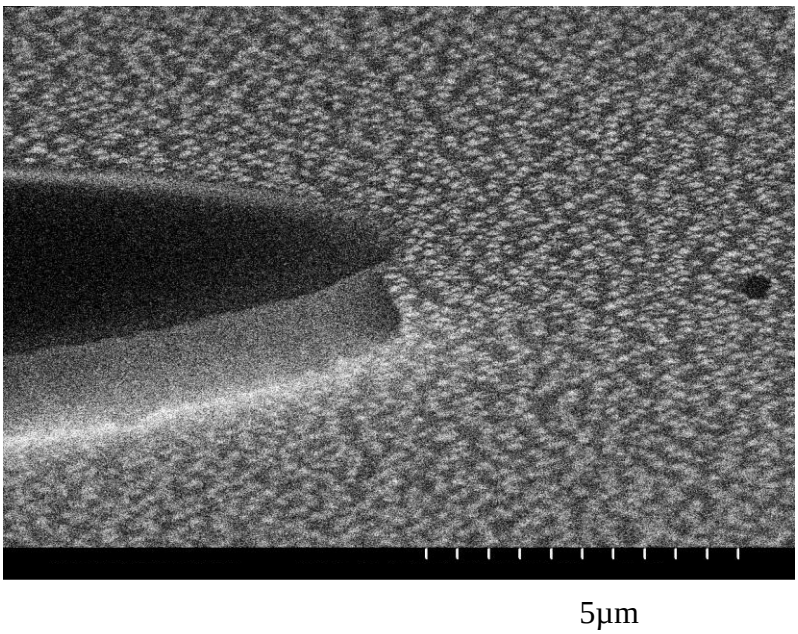

Figure 3.10: Undercut image of a pillar.

3.2.2.2 Patterning Micropillars using Optical Lithography

Photolithography is a process in which UV light is used to make patterns on chip surfaces. In this process chips are coated with a light sensitive resist called photoresist. Thereafter the chips are baked in order to remove solvents from the resist. Baked photoresists react to UV light by either getting etched or hardening with respect to a photoresist developing solvent. The former are called positive resists and the latter are called negative resists. Therefore one can use masks with patterns that either expose or cover the samples depending on the kind of resist used. In our case we use a positive photoresist (S1813).

The chips are processed in the Keck Microfabrication Facility in MSU. We use the Class 100 clean room for Optical/ Photolithography of our chips. The recipe used for the photolithography is explained as follows.

1) The chip is Spin coated with S1813 positive resist at 5K rpm for 50 seconds.

2) It is baked directly on a hot plate at 110^0C for 60 seconds.

3) We align the chip with a photo mask with six circular patterns of 50μm diameter each, using a mask aligner. We then expose the chip to UV light through the photo mask for 10 seconds.

4) The chip is dipped in Cholorobenzene for 5 minutes and rinsed in DI water to remove the Cholorobenzene. We blow dry the chip with Nitrogen gas and bake it on the hot plate at 95^0C for 60 seconds. Dipping the chip in Cholorobenzene helps the surface of the unexposed resist, i.e. the circular pattern, to harden. This in turn helps in providing an umbrella shaped top to the resist that is useful for the lift off process. This undercut

texture helps lift-off solvents to seep under the hardened top and dissolve the resist.

5) The exposed resist is 'developed', i.e. dissolved, for 55 seconds using a 352 Developer which is a NaOH (Sodium Hydroxide) based photodeveloper, and then rinsed in deionized water. The chip is blow dried with Nitrogen gas and baked at 95^0C for 60 seconds. Figure 3.10 shows the SEM image of an undercut after developing the exposed resist.

   Figure 3.11a shows the schematic of one sample on a chip, after the development step.

6) The chip is loaded onto an ion mill substrate holder.

3.2.2.3 Ion Milling

Ion Milling is a reverse process of sputtering. Here highly energetic Argon ions are used to etch away deposited metal atoms from the surface of a chip exposed to the ions. The photoresist acts as a mask by protecting the area covered by the resist from the Argon ions. Therefore we can selectively etch the area around the resist coating. The ion milling is done using a Commonwealth Scientific Argon Ion beam source. The vacuum chamber used for ion milling is also equipped with a dc magnetron sputtering system with a gold target and a boat to do thermal evaporation of SiO. A substrate plate has the facility to load 5 chips at a time. It also has a Film Thickness Monitor and an open spot that is used for SiO deposition, as explained later. A shutter with one opening under the substrate plate is used to control the exposure of a chip to the process that is desired. A load lock lets us avoid venting the chamber every time a chip is taken in or out. Substrate holders have a magnetic attachment. A magnetic arm is housed in the load lock and is used to attach to the substrate holder while loading and unloading a chip.

The following procedure is used to calibrate the etching rates of a metal or alloy.

1) A 100nm film of metal X is deposited using the same condition that the metal would be deposited on an actual sample.

2) Electron Beam Lithography is used to make a pattern (pattern width $< 30\mu$m). The pattern is easier to identify with an AFM, used later, than a larger pattern. A single layer of resist is used. The pattern is then developed.

3) After loading the film X in the Ion Mill chamber, about 200nm of Au is deposited on the FTM after feeding in the parameters for Au density in the thickness monitor program. The FTM is then exposed to the Ion Beam source and the Au milling rate (R_{Au}) is determined. The power supply condition (Beam source current and voltage) is kept constant during the experiment to maintain the same rate R_{Au}.

4) The time of exposure, of the film X, is calculated using the equation Time=$(d_{Assumed})/R_{Au}$ A thickness of $d_{Assumed}$ of the film X is milled.

5) The thickness etched, d_{Actual}, is then determined using an AFM.

6) A ratio of $d_{Assumed}/ d_{Actual}$ gives us a constant k_X for the metal X.

7) Thereafter, to mill a thickness 'd' of metal X, the time for milling is calculated using the equation Time=$(k_X/R_{Au})d$. The milling rate ratios of the relevant metals and alloys are shown in Table 3.3.

The calibration process is time consuming and is not repeated every time the Ion Mill is used. We assume that the Mill Rate ratios for a particular metal or alloy with respect to Au

X/Milling Ratio	k
Au	1
CFAS	3.9
Nb	6.8
Cu	7.1
Py	2.5

Table 3.3: Milling ratios of metals/alloys.

do not change. However, we measure R_{Au} every time, before milling our sample. We also make sure that the power supply conditions during Ion Milling of our chip are the same as what they were during the measurement of R_{Au}.

For our chips, we mill through the top Au (15nm)/Nb(25nm)/Cu(10nm) and a little bit $\sim$4nm of Py. The milling process defines the area through which our uniform CPP current flows. The process of ion milling is explained in the following steps.

1) The substrate holder is loaded into the chamber using a load lock.

2) The chamber is pumped down for 5-6 hours to a base pressure of $\sim$ 1-2 X 10^{-8}Torr.

3) Argon is introduced into the chamber and the FTM is rotated over the gold target set on the dc magnetron sputtering gun. The pressure in the chamber is increased to 3.1 X 10^{-3}Torr for Au sputtering.

4) The FTM (set for gold parameters) is rotated over the Au sputter position and the shutter is opened.

5) The gun is turned on and $\sim$200nm of Au is deposited onto the FTM.

6) The ion beam power supply is turned on and we wait 20 minutes for it to stabilize. The gate valve is opened to reach a pressure of 2.2 X 10^{-4}Torr.

7) The FTM is rotated on top of the ion beam source and the shutter is opened. We record the ion mill rate of Au, R_{Au}, for a few minutes till it stabilizes. The shutter is then closed.

8) We calculate the milling period of the chip based on the ratios of the metals/alloys, described above. For the present case, we want to mill Au(15nm)/Nb(25nm)/Cu(10nm)/ Py(4nm) on a chip, to pattern the six pillars. $\therefore$ Milling Time= $\frac{1}{R_{Au}}$[15nm k_{Au} + 25nm k_{Nb} + 10nm k_{Cu} + 4nm k_{Py}]

9) The chip is rotated over the ion beam source and milled for the calculated time, after which the shutter is closed.

10) The beam source keys are turned off and we wait for the ion beam source to cool down for 30 minutes before turning it off. The Argon is turned off after another 20 minutes. Figure 3.11b shows a schematic of one pillar after the process of ion milling.

3.2.2.4 SiO Insulation

The sample pillar obtained as a result of etching by the ion milling now needs to be properly insulated before the top Nb electrode deposition. The insulation prevents the top Nb electrode from shorting with the bottom Nb electrode and forces current to pass through the patterned area A, i.e. the sample pillar. A SiO insulating layer is deposited after dry etching with the ion mill in the same chamber. This removes sample dirt, which would make poor quality insulation. SiO is deposited using indirect thermal evaporation.

The source boat consists of two adjoining cylinders. The source is contained in the one which is covered. On heating the boat, the SiO vaporizes in the covered cylinder and the

vapor passes through the junction onto the empty uncovered one. Hence SiO is deposited indirectly.

The procedure of promoting a smooth steady rate of deposition prevents clumping of SiO on the surface of the sample. The system is water cooled during evaporation. The chip is rotated during the deposition process to ensure uniformity. This is done by opening the valve that connects the magnetic arm to the main chamber. The chip is then lifted with the arm. The substrate plate is rotated such that the opening on the substrate plate is directly on top of the SiO target. The magnetic arm is lowered just enough to make the chip sit approximately at the same height as the FTM. A spinner is then attached to the arm to make it spin along with the chip as the deposition takes place.

The deposition process is outlined as follows:

1) We open the valve to the magnetic arm and wait for the pressure in the chamber to go down to $\sim$ 3 X 10^{-8} Torr. This takes 5-6 hours.

2) Cooling water is turned on.

3) The power supply to the SiO evaporator is switched on and gradually increased to 0.02V. We let it stabilize for 20 minutes.

4) The variac to the power supply is finally increased to 0.025V and the FTM program is changed to the SiO parameters.

5) The substrate plate is rotated and the FTM is brought on top of the SiO target.

6) The shutter is opened and the SiO deposition rate is recorded. It is usually between 0.6 to 0.7nm/sec. The shutter plate is closed.

7) The magnetic arm is lowered and the sample is pulled out. The substrate plate is rotated and we bring the opening onto the SiO target position.

8) We lower the magnetic arm to approximately the height of the FTM from the target.

9) We attach the spinner and slowly increase the speed to 40rpm.

10) The shutter is opened and SiO is deposited to obtain a thickness of 150-160nm on the chip.

11) Finally the shutter is closed and the SiO power supply is slowly reduced to 0V.

12) We turn on Argon to protect the hot source and wait for 30 minutes before turning off water. We wait for another 30 minutes before taking out the chip using the load lock. Figure 3.11c shows a schematic of one pillar after the process of SiO deposition.

3.2.2.5 Lift Off

After insulation the samples are covered with SiO as shown in the Figure 3.11c. The next step in the processing is to remove the insulation from the top of the chip. This is done by lift off. The umbrella shaped structure of the photoresist, giving an undercut, becomes important at this step. The lift off is achieved by letting the photoresist dissolve in a solvent called PG Remover. The presence of the undercut ensures that the remover is able to reach the resist to lift it off. This process is done in the KMF Class 100 room.

The process is outlined as follows:

1) We dip the chip in a beaker containing PG Remover and place the PG Remover beaker in a water bath on a hot plate for $\sim$3 minutes.

2) We then pull out the beaker of PG Remover with the chip in it and place it in an ultrasonic cleaner for ∼2 minutes.

3) We alternate between holding in the water bath and ultrasonic cleaning for ∼15 minutes.

4) Finally we rinse the chip in DI water and blow dry with Nitrogen gas. Steps 2) and 3) are repeated if lift off is not good. Figure 3.11d shows a schematic of a sample after the process of lift off.

3.2.2.6 Ion Milling and Top Electrode Deposition

Before depositing the top electrode on each sample on a chip, we need to clean the surface of the chip of residual resists or oxide layers. To do that, we ion mill the chip for ∼10 seconds before loading it to the sputtering system for top Nb electrode deposition.

After taking the chip out of the ion mill substrate holder in the Class 100 room of KMF, we load the chip in the sputtering CIP substrate holder Figure 3.4b. We use a physical mask of similar dimensions as our substrate (0.5"X0.5") to mask the chip leaving the pillar samples exposed. The mask is thus designed to allow Nb to deposit on the pillars but prevent any shorting between them. The sputtering process is similar to Section 3.2.1 and the sample is completed with a layer of 150nm of Nb followed by 5nm of Au. The Au prevents oxidation and provides better adhesion to the indium contacts. Figure 3.11e shows a cartoon of a sample after the process of top electrode deposition. Figure 3.11f shows the top view image of a chip. Indium electrodes are soldered onto the top Nb pads for lead connections.

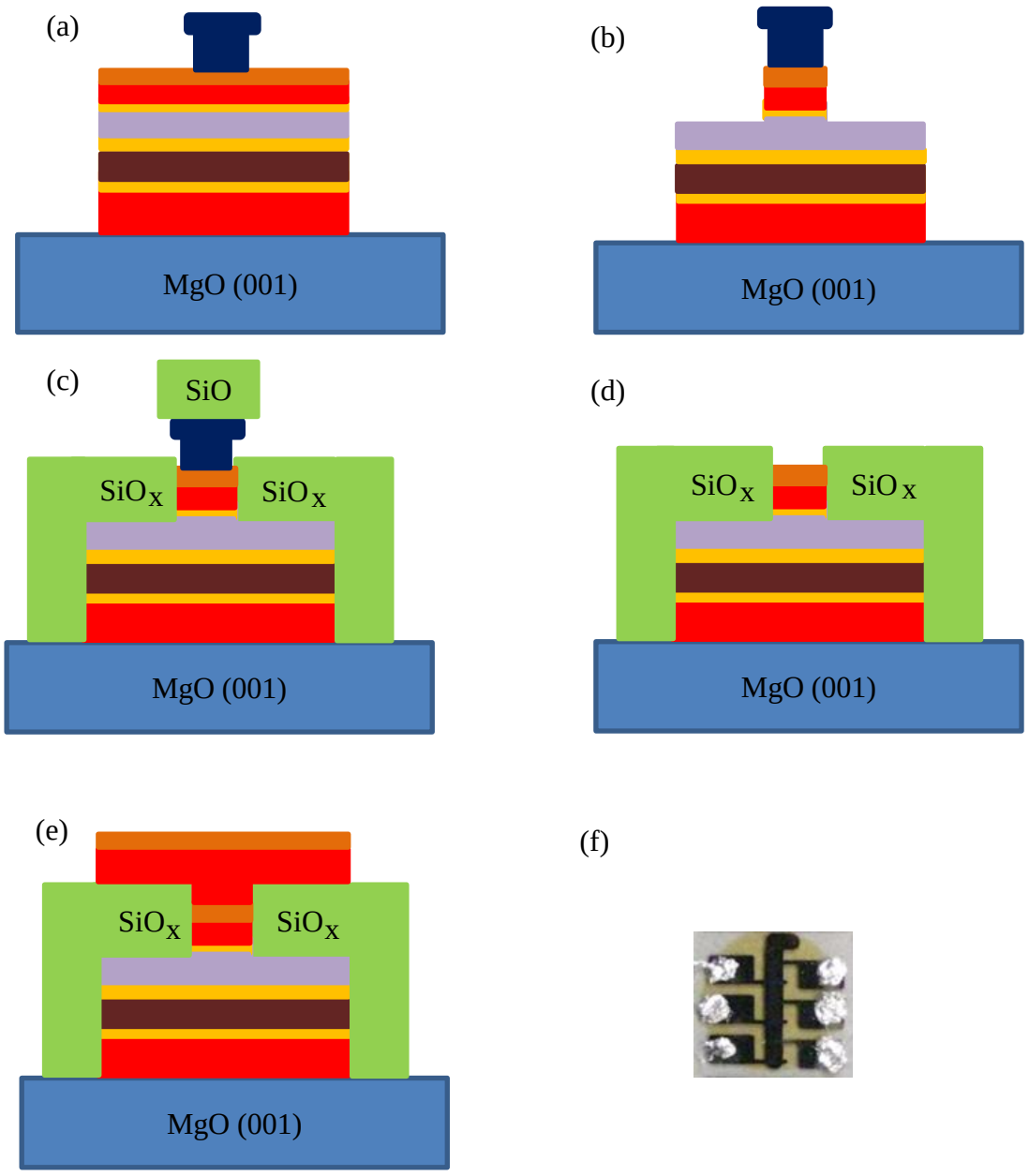

Figure 3.11: Sample Patterning :(a)After Photolithography, Chlorobenzene hardening and development.(b)After Ion Milling (c)After SiO deposition (d)After Lift Off (e)After top electrode deposition (f)Top View of a chip.

3.3 Measurement Techniques

The following sections discuss various equipment and techniques used to analyze our samples.

3.3.1 Resistance Measurement

The sample geometry, and resulting very small resistances R_S of our CPP MR samples, require special measuring equipment [29][83]. We use a potentiometer bridge circuit with a Superconducting Quantum Interference Device (SQUID) as a null detector to achieve the required sensitivity. We apply a known current I_S (Maximum I=100mA) through our sample, which acts as the resistance of one arm of the bridge circuit. The other arm of the bridge circuit is a known reference resistance R_{Ref}. A current I_{Ref}, which passes through R_{Ref}, adjusts through a feedback circuit connected with the SQUID to balance the potentiometer circuit. Finally with known R_{Ref}, feedback resistance R_b and the voltage V across R_b (=I_{Ref} x R_b, in a balanced circuit the same current flows through R_b and R_{Ref}), the computer is programmed to calculate the sample resistance in a balanced potentiometer circuit. This is given by $R_S = \frac{V}{I_S}\frac{R_{Ref}}{R_b}$.

Since the measurements are made at Liq Helium (He) temperature (4.2K), we need a convenient cooling and warming system. We describe the equipment, designed by Prof. William P.Pratt Jr., to mount samples in a SQUID potentiometer assembly. The assembly is ∼1m long with the sample mounted at the bottom. This assembly allows the user to submerge and pull a sample out from a 60 liter Liq. He storage dewar fairly quickly (∼20min). The assembly is appropriately called the Quick Dipper (QD). The sample is placed within a superconducting magnetic coil that produces a magnetic field in the plane of the sample.

There are two QD assemblies, differing in the value of the Reference Resistor R_{Ref}(=95$\mu\Omega$ for QD1 and 126$\mu\Omega$ for QD2) and the magnetic field strength (Calibrated Magnetic Coil Constant: QD1= 574 Gauss/A and QD2= 560.5 Gauss/A). QD1 can go up to fields ∼3K Gauss and QD2 can go up to fields ∼5K Gauss. Stepwise variation of the magnetic field is controlled by a computer program. The QD (1 or 2) contains a SQUID and a persistent switch used to eliminate fluctuations in the current supplied to the superconducting magnetic coil, thereby reducing variations in the field during measurement. This whole unit is slowly inserted into the 100L Liq. He storage dewar until the sample is submerged under the Liq. He at 4.2K. During measurement of R_S, an in plane magnetic field is varied under computer control using a Kepco magnetic power supply. Figure 3.12 shows a schematic diagram of the SQUID potentiometer circuit.

3.3.1.1 Sample Connections

In this section we briefly discuss the preparations prior to mounting a sample on the QD. The three projects described in the present thesis have different sample structures which will be described in detail in Chapters 4, 5 and 6. For the moment we will focus on the different methods of preparation for each sample type.

- Ir/Pd Multilayer samples: In these CPP S Nb cross stripped samples, we put Indium contacts on the Nb strips using ultrasonic soldering. The four probe connections with two voltage leads and two current leads are shown in Figure 3.12.

- IrMn (FeMn) EBSV samples (Section 1.6): In these CPP S Nb cross stripped samples,

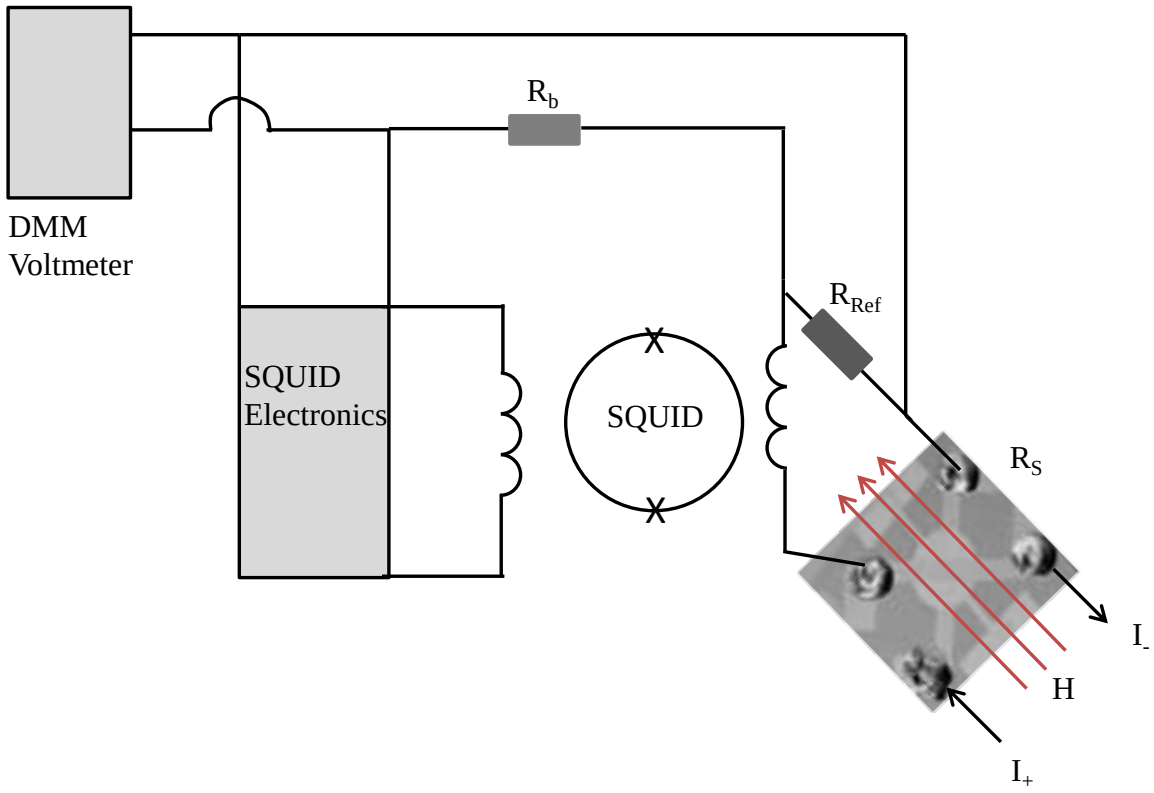

Figure 3.12: SQUID based potentiometer circuit. R_S is the sample resistance, connected to the V and I leads. H is the in-plane field (applied in the pinned direction in EBSV samples). R_b is the feedback resistance. R_{Ref} is the reference resistor ($95\mu\Omega$ for QD1 and $126\mu\Omega$ for QD2)

we first put Indium contacts on as before. However since these samples are EBSV, we need an additional step of Pinning the ferromagnetic F layer adjacent to the antiferromagnetic AF layer prior to mounting the sample on the QD. To pin the magnetization of the F layer next to the AF, we heat the sample to a temperature higher than the Blocking temperature of the AF (in this case ∼453K for an 8nm thick FeMn AF layer) in a vacuum chamber. The sample is then cooled in the presence of a magnetic field of 200 Oe. The effect of pinning is described in Section 1.6. After the pinning process the sample is mounted on the QD with the four probe connections made as in Figure 3.12. It is however important to align the pinned easy axis of the F layer along the magnetic field of the superconducting magnetic coil of the QD.

- Hybrid Spin Valve Micropillar samples: The four probe measurement for the half metallic CFAS spin valve micropillars is shown in Figure 3.13. Indium is used to make contacts with the leads of the six samples on a chip. A Voltage and a current lead are connected to the Nb pad corresponding to the sample to be measured (sample 1 in Figure 3.13). The current then flows into the sample being measured and out of an adjacent sample (sample 2). The voltage drop across the sample is measured by connecting the other voltage lead to a third sample through which no current flows. Since the Nb is superconducting at the measuring temperatures, only the drop across sample 1 is measured. This process can be repeated for any of the six samples on a chip as long as at least three samples are working.

To check the QD connections and sample quality, we make the following measurements prior to measuring R_S for the sample multilayer:

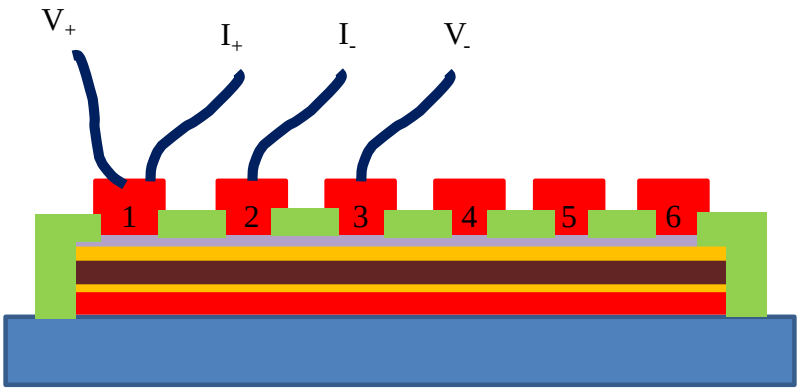

Figure 3.13: Connections to measure resistance of sample 1.

- After connecting the Voltage and Current leads in either of the QD systems, we connect a multimeter to the "Sample" coaxial connection at the top of the QD to measure the resistance of the leads. It is usually in the range of 20-30Ω which is essentially the total lead resistance.

- We check the resistance of the sample with respect to ground to check for possible shorts of the current leads to the QD body.

- We check the feedback resistance. It should be ∼10kΩ.

- After dipping the QD in the Liq. He dewar, we check the sample lead connection again. The resistance should now be ∼6Ω the resistance of the leads at Liq. He temperature.

- Before turning on the magnetic field, we check for possible superconducting shorts by measuring the current dependence of our samples. The variation of the sample resistance, with respect to different fractions of a full scale current (0.01,0.1 and 1 fraction of full scale current), is observed. A substantial increase in resistance with

increase of current fraction from 0.01 to 1 shows the presence of pin holes, which make the sample superconducting for small currents and resistive for larger currents. Such shorts are rare with samples sputtered at low temperatures, but occur more often with epitaxial samples (1 in 4 samples).

3.3.2 Area Measurement

In CPP samples deposited using the low temperature sputtering system, the area A through which current flows is calculated by measuring the widths of the two Nb cross strips and multiplying them together to get the area A = W_1X W_2. The widths are measured using a Dektak surface profiler. Each strip is scanned four times and the results are averaged [30]. The error is given by the twice the standard deviation of the mean of the four width scans performed on each Nb strip. Finally the error on the area is obtained in quadrature. To allow for systematic uncertainties, such as different values for a given area found by different users, the minimum uncertainty for a given A is taken as 5%.

For the micropillar samples in the half metallic studies, the sample area A through which uniform current flows is the 50μm diameter circular area obtained with the photomask. SEM pictures, obtained using the Hitachi SEM in the KMF facility, are used to measure the pillar diameters. Figure 3.14 shows one pillar.

3.3.3 Resistivity Measurements

The Van der Pauw (VdP) technique is a convenient method to measure the resistivities (ρ) of metals/alloys since it can be used on any arbitrarily shaped sample without holes by

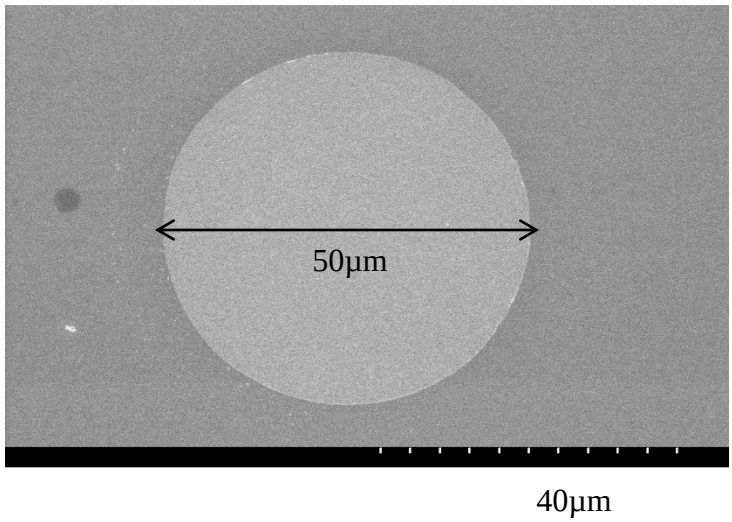

Figure 3.14: SEM image of a pillar with 50μm diameter.

measuring its sheet resistance [84]. The VdP measurement on a uniform film of a metal gives us the current-in-plane (CIP) ρ for that metal. For our samples, we are interested in the current-perpendicular -to-plane (CPP) ρ of a metal. In principle, ρ for a cubic metal is isotropic. But columnar growth of sputtered multilayers may lead to different structures in the perpendicular and parallel directions to the metal plane. Hence in general for sputtered metals, the CIP and CPP ρ need not be identical. Fierz et al [28] measured CPP ρ of F (Ni and Co) metal films by making Nb/F(t_F)/Nb samples with varying t_F. A plot of AR versus t_F, measured on these samples at 4.2K, gave the expected linear increase of R with t_F. ρ_F is the slope of the graph. The same technique can be used to measure CPP ρ_N for N metals by putting thin layers of F next to the Nb to eliminate any proximity effect in the N metal at 4.2K. Test comparisons of the CIP and CPP resistivities, at 4.2K, show results usually consistent to within mutual uncertainties [38]. Hence we usually choose the more convenient CIP VdP measurement.

To determine the layer resistivities we regularly sputter separate films of metals/alloys using the CIP holder (Section3.2) in the same sputter runs while depositing CPP samples. To minimize surface effects, the thickness of a metal film is chosen to be much larger than its mean free path. The mean free path of a metal (averaged over the mean free paths on the Fermi surface) is estimated as $\lambda_t = \frac{(\rho_b l_b)}{\rho}$, where $\rho_b l_b$ is a temperature independent constant for the metal with dimensions of AR and of the order of 1 fΩm^2 [33][85]. ρ is the resistivity of the metal at a given temperature. As an example, consider Copper (Cu). The resistivity at 4.2K is 5$\pm$1nΩm [33] and $\rho_b l_b \sim 0.6$ fΩm^2 [85]. Using the above equation, the mean free path of Cu can be estimated to be $\lambda_t \approx 120$nm. A film of Cu with thickness larger than 120nm should be sufficient to minimize surface effects. We usually grow 200nm of the metal/alloy film to be measured. Now Cu is a very low resistivity metal and most metals listed in Table 3.4 have higher resistivity than Cu. Therefore Cu serves as an example of a metal with a longer mean free path as compared to other metals of concern in this thesis and a usual film thickness of 200nm for VdP measurements is acceptable.

An exception is shown in Table 3.4 for FeMn deposited using a small gun. The thickness of FeMn used is 40nm which should be sufficient to minimize surface scattering due to the large FeMn resistivity ($\rho \sim 1000$nΩm). Indium contacts are soldered at the corners of the film of interest, Figure 3.15. Two Voltage and two Current leads are then attached to these contacts in a two step process.

1) First the two voltage leads are attached between contacts 1 and 2, and the current leads are attached between 3 and 4. To check linearity of V with I, the current source is varied

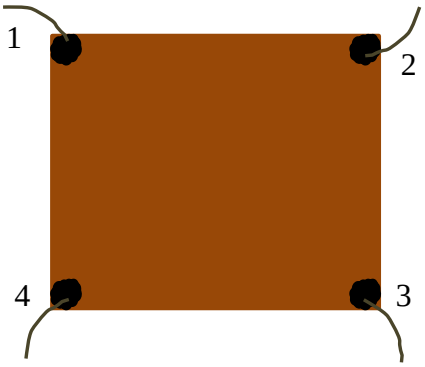

Figure 3.15: Connections for VdP measurements. $R_1 = V_{12}/I_{34}$ and $R_2 = V_{23}/I_{14}$.

in steps from 1mA to 30mA and the voltages are measured. The process is repeated for negative currents to eliminate thermoelectric effects and voltage offsets of the voltmeter. The resistance is calculated for each current and an average R_1 for the two highest current measurements is obtained.

2) The leads are then switched to connect the voltage leads between 2 and 3 and current leads between 1 and 4 and the process is repeated with currents of both polarities. The resistance in this case is labeled R_2.

The resistivity is given by the equation $\rho = \frac{(\pi t(R_1 + R_2)f)}{2ln(2)}$, where t is the thickness and f is a correction factor determined from the ratio of R_1 to R_2. The value of f is obtained from the graph in [84].

We check the resistivities obtained from VdP measurements as follows.

1) The resistivities of metals/alloys measured at 4.2K are compared to the resistivities obtained at the same temperature, previously in our group using similar methods. Some comparisons are shown in Table 3.4. Most of our values, with the exception of FeMn, are

Metal/Alloy	#N Films	Target Size	ρ(4.2K) $\pm\delta\rho$ (Present)(nΩm)	ρ(4.2K) $\pm\delta\rho$ (Prior)(nΩm)	$\Delta\rho$ (Present) (nΩm)	$\Delta\rho$ (Pure) (nΩm)
Ir	6	Large	118±8	-	56±17	50[85]
Pd	4	Large	46±1	40±3 [62] [63]	108±8	106 [85]
Co	4	Large	53±5	60±9 [86]	65±12	57 [85]
Py	2	Large	93±5	120±40 [86] [87]	106±15	-
Nb	9	Large	50±9	78±15 [86] [87], ∼60[28]	148±27	144[85]
IrMn	13	Large	1497±109	-	46±160	-
FeMn	4	Large	1289±129	875±50[40]	42±145	-
FeMn	2	Small	999±219	875±50[40]	323±396	-

Table 3.4: The average resistivity (ρ(nΩm)) of sputtered metals/ alloys measured at 4.2K, with the exception of Nb (measured at 13K), is compared to prior measurements. The average values are obtained by measuring N films of each metal/alloy. $\Delta\rho = \rho(295K) - \rho(4.2K)$ (For Nb, $\Delta\rho = \rho(295K) - \rho(13K)$) is compared to the pure metal values from Landolt- Bornstein[85]. Target size indicates whether a 2.25" diameter (Large) or a 1" diameter (Small) was used to deposit the films. Nb resistivity is measured using a Quantum Design SQUID Magnetometer(Section 3.3.4). The FeMn resistivity for the small gun was measured on a 40nm thick sample.

compatible with the previous measurements.

2) The resistivities are measured at both room temperature and at 4.2K to obtain the difference, $\Delta\rho = \rho(295K) - \rho(4.2K)$, which can be compared with the ρ for pure metals assuming Matheissen's rule for the resistivities. According to Matheissen's Rule, the resistivity $\rho(c,T)$ of a metal at a temperature T with impurity concentration c is estimated as $\rho(c,T) \approx \rho_0(c) + \rho_P(T)$, where $\rho_0(c)$ is the resistivity due to the impurity c and $\rho_P(T)$ is the resistivity of the pure metal at temperature T. A comparison of $\Delta\rho$ from our measurements to $\rho_P(T)$ is shown in Table 3.4. The values are compatible. Since Nb becomes superconducting at 4.2K, the resistivity is measured at 13K using a Magnetometer to reach this temperature (described in the following section).

3.3.4 SQUID Magnetometer

Two SQUID (Superconducting Quantum Interference Device) based magnetometers, MPMS XL and MPMS XL II, from Quantum Design are used for two purposes :

1) Magnetization Measurements: MPMS XL can achieve a maximum field of 5 Tesla and can be set at any temperature from 2K to 400K. MPMS XL II can achieve a maximum field of only 1 Tesla and a temperature range of 2K to 350K. MPMS XL II is shielded against earth's magnetic field and therefore can be used for high resolution magnetic measurements.

2) ρ and T_C Measurements: The capability of setting the magnetometers at various temperatures makes them useful to measure transport properties. Hence it is also useful to measure resistance or resistivity at temperatures other than 4.2K or room temperature. In particular, we use them to measure the transition temperature of Nb and its resistivity at 13K which is above its transition temperature $T_C = 9.2 \pm 0.2$ K. The average value of T_C we obtained, by measuring the change in Nb resistance with varying steps of temperature, was $T_C = 9.0 \pm 0.1$K which is pleasantly close to with the known Nb T_C= 9.2K [16]. The close agreement highlights the purity of our sputtered Nb.

3.3.5 Energy Dispersive Spectroscopy

We use Electron Dispersive Spectroscopy (EDS) to determine the elemental composition of our $Co_2Fe(Al\ Si)_{0.5}$ (CFAS) Target and deposited samples by measuring the energies of the emitted X Rays when an electron beam strikes the surface of the sample. A sample holder was designed to hold the CFAS target (0.25") in the SEM high vacuum chamber to maintain

a required distance (working distance) between the electron gun and the sample surface. When a beam of electrons with energy greater than the characteristic excitation energy of an element, strikes atoms of the elements constituting a sample, inner shell electrons are knocked out and higher energy shell electrons jump to vacancies created in the inner shells releasing energy in the form of X Rays. The energy and wavelength of the X Rays produced is characteristic of the element. The EDS measurement system is housed inside a Hitachi Scanning Electron Microscope (SEM) which can produce an electron beam with adjustable energy (by modifying the accelerating voltage of the electron beam). An X Ray detector system is located within the vacuum chamber of the SEM. It consists of mainly four parts; a collimator, a detector crystal, a field effect transistor and a liquid nitrogen dewar. The Collimator eliminates stray radiation from striking the detector. A detector crystal made of Si infused with Lithium to provide a semiconductor region is located at a low angle close to the sample region. The SiLi crystal detector converts each X Ray into voltage pulses which are amplified using the field effect transistor. The liquid nitrogen dewar keeps the detector crystal cold, thereby preventing redistribution of the Li, reducing electronic noise, and maintaining a constant SiLi resistance, preventing any shorting out from the bias voltage to the semiconducting SiLi at higher temperatures.

The analyzer part of the EDS system consists of a pulse processor, an analog to digital convertor, a multichannel analyzer and finally a computer display. The analyzer components convert the amplified voltage pulses produced by the detector system to a series of pulses that correspond to the energy of the X Rays and finally sorts them into different channels based on their energy. Finally the computer outputs and analyzes the X Ray spectra and displays the elements corresponding to the energies of the X Rays.

Chapter 4

Specific Resistance of (Iridium/Palladium) N1/N2 interface.

This project was published in [60]. It has been rewritten and expanded for this thesis.

4.1 Introduction

In metallic multilayered structures, scattering at interfaces plays an important role in electron transport. In an $[N1/N2]_n$ multilayer, with n repeats of the non-magnetic metals N1 and N2, such scattering is characterized by twice the interfacial specific resistance, $2AR_{N1/N2}$. In this chapter, we focus on 2AR for sputtered interfaces of the metal pair, Palladium (Pd) and Iridium (Ir)[60]. Our motivation for choosing Pd/Ir is explained as follows.

In prior studies of 2AR [38] [30] [62]–[73], special interest has attached to lattice matched pairs that have the same crystal structure and the same lattice parameter a_o to within $1\%(\Delta a/a_0 \leq 1\%)$. As explained in Section 2.3.1.2, calculations of AR for such pairs can

be done without any free parameters, using the local density approximation to calculate the electronic structure of each metal and then a modified Landauer formula to calculate $2AR_{N1/N2}$ for chosen interface structures, such as perfectly flat, not intermixed interfaces, or two or more monolayer (ML) thick 50%-50% random alloys of the metals [74]–[78] (Section 2.3.1.2). Values of 2AR for four lattice matched pairs, Ag/Au[75][78], Co/Cu[75][78]–[79], Fe/Cr[75][76] and Pd/Pt[62], agree well with calculations for both perfectly flat and 50%-50% alloyed interfaces (Table 4.1).

At the other extreme, for metal pairs with lattice parameters differing by 5% or more, experimental values of 2AR disagree with calculations by from 50% to more than factors of two [70]. Reducing the lattice parameter difference from $\sim$ 10% for Pd/Cu to 5% for Pd/Ag and Pd/Au did not improve the agreement between theory and experiment [70]. A study comparing calculations and experiments of residual resistivities of impurities in different hosts showed that calculations are sensitive to local strains [88].

Pd and Ir have FCC structures with bulk lattice parameters that differ by slightly over 1% (1.3% [22]). They thus fall between the pairs where data and theory agree and disagree. The aim of this project was to see whether experiment and calculations agree for them. The study was set up as double blind, with our experimental findings and calculations by the theoretical group of K. Xia in China not shared until each group had determined its value for comparison. In addition, of the four other pairs listed in Table 4.1, Ag/Au, Fe/Cr and Pd/Pt are all mutually soluble, whereas Co/Cu are barely mutually soluble at 295K [89]. Since Pd/Ir are also not mutually soluble at 295K (Ir and Pd are miscible only above 1753 K−see Figure 291 in [89]), our study should also extend our knowledge of mutually insoluble pairs.

The present Chapter is organized as follows. We begin in Section 4.2 with a description of the sample design to determine $2AR_{Ir/Pd}$. In Section 4.3 we present $\theta - 2\theta$ X-ray diffraction measurements used to check the orientations and lattice parameters of the sputtered Pd and Ir layers and the periodicity of the Pd/Ir multilayers. In Section 4.4, we briefly describe the application to Pd/Ir of the theory covered in Section 2.3.1. In Section 4.5 we present our experimental results, and compare them with the calculations by our collaborators Xia and Wang. In section 4.6 we summarize and conclude.

4.2 Experimental Technique:

We use the CPP S sample geometry (Section 1.5) to obtain $2AR_{Ir/Pd}$. Our samples are sputtered multilayers grown at temperatures between -30^{o}C and + 30^{o}C (Section 3.2.1). To obtain AR (Sections 3.3.1 and 3.3.2), CPP resistances are measured using an ultra sensitive SQUID based potentiometer and area A is measured using a Dektak Profilometer. The uncertainty in AR is mostly contributed by a typically 5% uncertainty in A.

4.2.1 Sample Structure:

Our technique to determine $2AR_{Ir/Pd}$ follows from [64], based upon a [Pd(t)/Ir(t)]$_n$ multilayer with fixed total thickness, t_T = 360 nm = 2nt. If the Pd and Ir layer thicknesses are kept equal to each other, then the total thicknesses of both Ir and Pd stay fixed at $t_T/2$, and as n increases, only the number of interfaces increases linearly with n. If the interfaces

are infinitely thin, the total specific resistance of the multilayer alone should be given by

$$AR = \rho_{Ir}\frac{t_T}{2} + \rho_{Pd}\frac{t_T}{2} + n(2AR_{Ir/Pd}) \tag{4.1}$$

According to Equation 4.1, a plot of AR versus n should give a straight line with slope $2\mathrm{AR}_{Pd/Ir}$.

In practice, the sample must be more complex. Two 10 nm thick layers of Cobalt (Co) are deposited between the Nb strips and the Pd/Ir multilayer to eliminate any superconducting proximity effect. Co prevents a direct contact of the superconducting Nb with the non-magnetic Ir /Pd multilayer which can turn part of the Ir and Pd superconducting. Our actual samples have the form:
Nb(150nm)/Cu(5nm)/Co(10nm)/$[\mathrm{Ir(t)/Pd(t)}]_n$/Co(10nm)/Cu(5nm)/Nb(150nm) The 5nm of Copper (Cu) next to the Nb electrodes is included to give best multilayer growth conditions. Cu adjacent to the superconducting Nb becomes superconducting due to the proximity effect. The 10 nm layers of ferromagnetic Co are far enough apart (360 nm) that they produce no significant CPP-MR (Section 2.3.1).

In this model, we subsume into $2\mathrm{AR}_{Ir/Pd}$ all interface contributions, including any due to finite interface thickness. When the interfaces begin to overlap, AR should increase more slowly, eventually becoming constant when the layers are so thin that the sample becomes just a uniform 50%-50% alloy.

4.2.2 Equation and Estimate of Intercept for later consistency check:

According to Equation 2.33 from Section 2.3.1, the total specific resistance, AR is given as

$$AR = AR(AP) = (2AR_{Co/Nb} + 2\rho_{Co}{}^{*}(10nm) + (AR_{Co/Ir}{}^{\uparrow} + AR_{Co/Pd}{}^{\downarrow})/2 + \rho_{Ir}(360nm)/2 + \rho_{Pd}(360nm)/2) + n(2AR_{Ir/Pd}) \tag{4.2}$$

Combining the constant sum of terms in the parenthesis in Equation 4.2 and representing them as K gives

$$AR = K + n(2AR_{Ir/Pd}) \tag{4.3}$$

A plot of the total AR versus n should give a straight line up until the finite thickness interfaces start to overlap, after which the total resistance starts to saturate. The slope of this line is equal to $2\mathrm{AR}_{Ir/Pd}$. The intercept of the plot, AR(n=0) should be given by K in Equation 4.3. In Section 2.3.1, we estimated K from independent measurements; adding up the six terms gave K=36$\pm$5 $f\Omega\mathrm{m}^2$. In Section 4.5.2, we will compare this value with our data as a check for internal consistency.

4.3 Structural Studies:

To check crystallographic orientations and lattice parameters of our sputtered Ir and Pd, we took $\theta - 2\theta$ high angle X-ray diffraction spectra on sputtered 200nm thick films of Ir

and Pd. The resulting plots are shown in Figure 4.1. For low temperature sputtering, the metals should grow in close packed planes, which for FCC Ir and Pd are (111). The lattice parameters for the bulk metals are a_{Ir} = 3.84Å and a_{Pd}=3.89Å, giving $\Delta a/a_{Ir} = (3.89 - 3.84)/3.89 = 1.3\%$ [22]. These lattice parameters should give interplanar spacings $d_{Ir} = a_{Ir}/\sqrt{3} = 2.22$Å and $a_{Pd}/\sqrt{3} = 2.25$Å.

From Bragg's law [22], we expect

$$2d_{hkl}sin\theta = m\lambda \tag{4.4}$$

where λ=1.54Å is the Kα wavelength for Cu, the source of the X-rays, the integer m is the order of diffraction (in Figure 4.1, m = 1), and θ is the angle between the incident X Ray and the scattering planes.

From Equation 4.4 and the data in Figure 4.1, we get d_{Ir} = 2.23± 0.01Å and d_{Pd} = 2.25± 0.01Å.

To determine the bilayer thicknesses of our Ir/Pd multilayers, we used $\theta - 2\theta$ low angle XRD as shown in Figure 4.2. The plots are for bilayers with n= 100 and n=160. The d from Figure 4.2 for n= 100 is d=33.7 Å and that for n=160 is d=20.5Å. The intended values for the thicknesses are d=36Å for n=100 and d=22.5Å for n=160. Therefore the multilayer periodicities are within 7% of the intended.

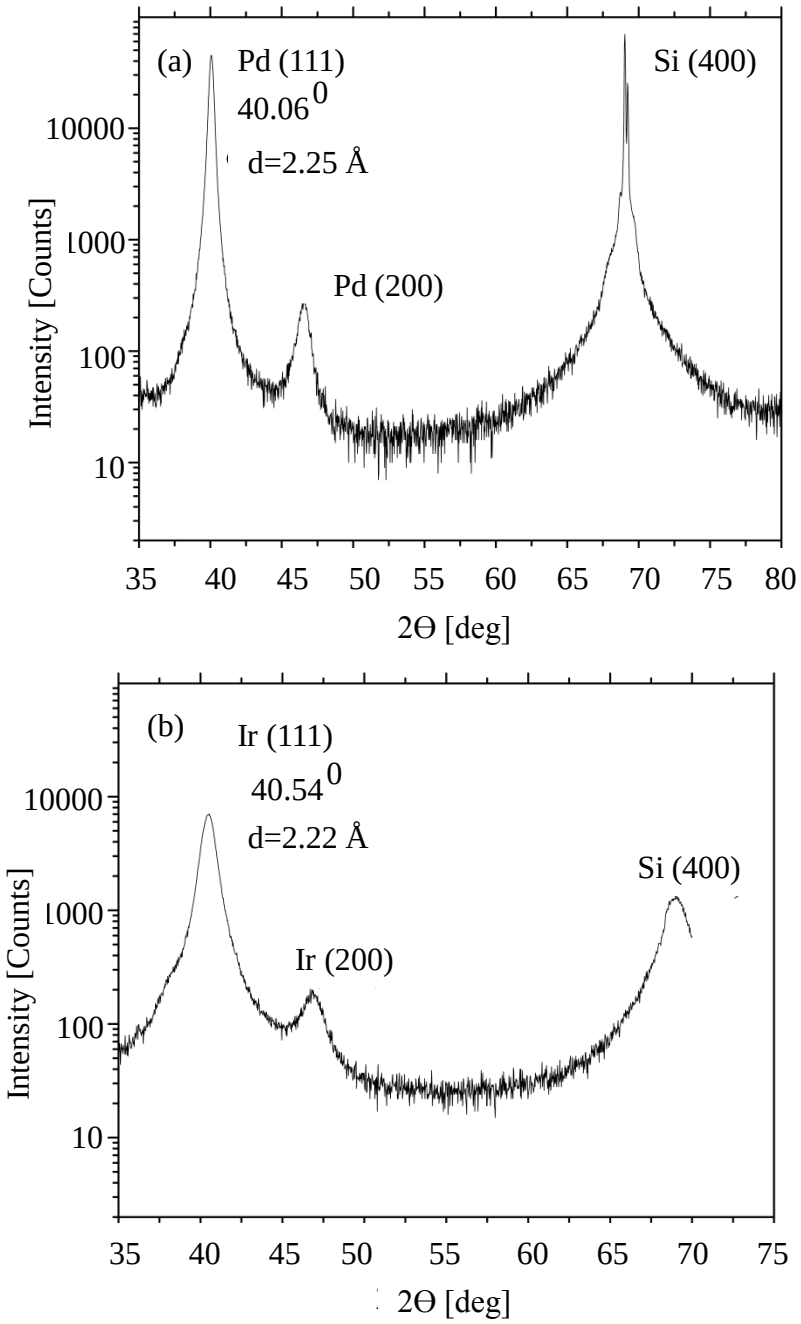

Figure 4.1: (a) Pd High angle XRD. (b) Ir High Angle XRD. The peaks correspond to (111) FCC peaks of Ir and Pd, and (400) peak of the Si substrates.

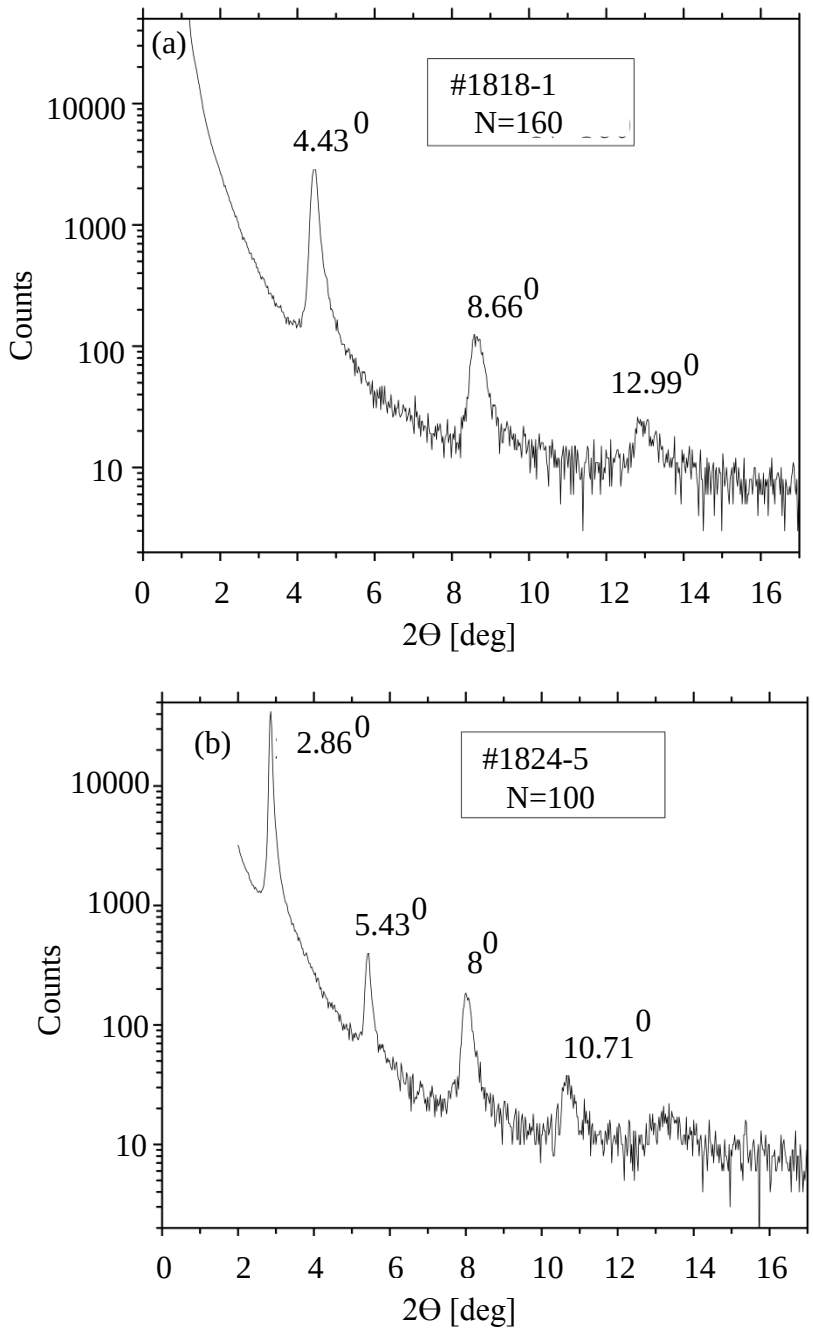

Figure 4.2: (a)and (b)are Low angle Xray spectra of $[Ir/Pd]_n$ for n= 160 and n=100.

4.4 Theory:

The general procedures for calculating 2AR for a lattice matched pair are described in Section 2.3.1. We describe here the application of this technique to Pd/Ir. The technique is two-step: 1) calculate the electronic structures of the metals, assuming a common lattice structure and lattice parameter; then 2) calculate 2AR using a modified Landauer formula, for two different types of interfaces: (a) a perfectly flat interface with no metal intermixing, and (b) an intermixed interface consisting of 2ML of a 50%-50% random alloy of the two metals.

(1) The local density approximation (LDA) is used to calculate the electronic structure, assuming the common FCC crystal structure of the two metals and a common lattice parameter. The obvious choice of the common lattice parameter is the average of the lattice parameters of the two metals, d=3.87Å. Xia and Wang checked that using the equilibrium lattice parameter of either d_{Pd}=3.89Å or d_{Ir}=3.85Å, changed $2AR_{Ir/Pd}$ by only ∼2%. Once these assumptions are made, the electronic structures are determined using a choice of the crystal potential. In prior publications [75][78], the crystal potentials were based upon Linear Muffin Tin Orbitals (LMTO) and an *spd* basis (ℓ_{Max}=2 with 9 orbitals). At the time of the present double blind study between our experimental group and our theoretical collaborators, Xia and Wang, had updated their electronic band structure calculations to a full Muffin Tin Orbital (MTO) potential with an *spdf* basis (ℓ_{Max}=3 with 16 orbitals). In Section 4.5.3 we will compare our results with both MTO *spd* and *spdf* calculations.

After the electronic structures are calculated, the 2AR of metal pairs can be determined using a Landauer formula, modified for the Sharvin resistance, with no adjustments [74].

Earlier studies showed that agreement with experimental results for interfacial resistances occurred only for diffuse transport through the bulk of the metals. In contrast, assuming ballistic transport led to quantum coherence and disagreement with experiment [74]. Using diffuse transport through the bulk of the metals, Xia and Wang determined the interfacial resistance for two separate kinds of interfaces- perfectly flat and 2ML of 50%-50% intermixed alloy.

4.5 Results and Discussion:

In this section we first present our experimental data and then compare them to the calculations by Xia and Wang done independently as a double blind study.

4.5.1 Experimental Result:

The analysis in Section 2.3.1 and Section 4.2 predicts that AR should increase linearly with n and then saturate. Figure 4.3 shows a plot of total AR versus n, which does as predicted.

The slope of the linear part of the plot gives $2\mathrm{AR}_{Ir/Pd}$. Given uncertainty in the data, and the inability to absolutely define the beginning of the saturation of total AR, we tried different fits. In Figure 4.3, we show best fit lines for $n = 100$ (dashed line), $n = 120$ (solid line) and $n = 140$ (double dashed line). The slopes (S) of the three fits are 1.06±0.03 $f\Omega\mathrm{m}^2$, 1.04±0.03 $f\Omega\mathrm{m}^2$ and 1.00±0.04 $f\Omega\mathrm{m}^2$, respectively for n= 100, 120 and 140. Taking account of the uncertainties, we choose as our best estimate $2\mathrm{AR}_{Ir/Pd}$=1.02±0.06 $f\Omega\mathrm{m}^2$.

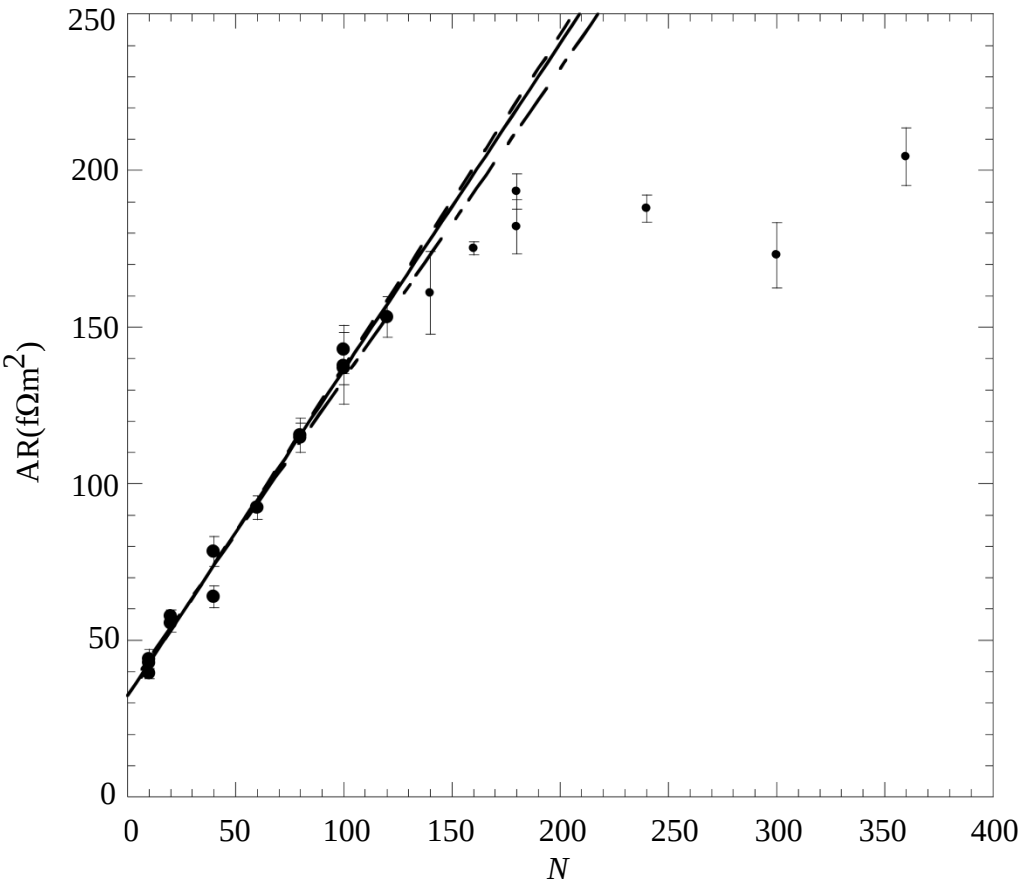

Figure 4.3: AR versus n. Dashed line shows linear fit till n= 100; solid line shows linear fit till n=120; double dashed line shows linear fit till n=140. For n=100, Intercept = 31.7±2.1 Slope = 1.06±0.03. For n=120, Intercept = 32.3±2.1 Slope = 1.04±0.03. For n=140, Intercept = 34.2±2.6 Slope = 1.00±0.04.(all units are in $f\Omega\text{m}^2$)

4.5.2 Test for Consistency

As a check for internal consistency of our analysis, we compare the intercepts from the plot of AR vs n with K from Equation 4.3. Our best fit lines in Figure 4.3 for n=100, 120 and 140 give intercepts: 31.7±2.1 $f\Omega\text{m}^2$, 32.3±2.1 $f\Omega\text{m}^2$ and 34.2±2.6 $f\Omega\text{m}^2$, respectively. Rounding the average of these three values gives AR(n=0)=33±2 $f\Omega\text{m}^2$. This value is compatible with our estimate of K= 36±5 $f\Omega\text{m}^2$ obtained in Section 2.3.1.

From the value at which the data saturate we can estimate the resistivity of a 50%-50% alloy of Ir and Pd. For a total thickness of 360nm the total AR saturates at ∼190 $f\Omega\text{m}^2$. Thus, $\rho(50\% - 50\%)$ =AR/360nm ≈ 500 nΩm.

Unfortunately we cannot check this value independently due to the lack of enough reliable information from the two references [85] [90] have usual alloy resistivities. We can, however, estimate the thickness of interface from the value of n at which the total AR saturates. Saturation indicates the point at which the individual thicknesses of the Ir and Pd layers become comparable to the interface thickness t_I. From Figure 4.3, if we estimate $n = 180$, as the last n to which we can fit a line passing through the data before saturation occurs, the thickness of the interface is 2t_I=360nm/180=2.0 nm. Hence the interface thickness can be estimated to be $\text{t}_I \sim$ 1nm, at the upper end of the expected thicknesses of our sputtered interfaces [64].

4.5.3 Comparison with Theory

We are now ready to compare our experimental value of $2\text{AR}_{Ir/Pd}$ with the calculations done by Xia et al [78].

1) For the present study Xia et al first calculated the electronic structure using the LDA approximation for the Ir and Pd Fermi surfaces based on MTO with a *spd* basis and using a lattice parameter of a_0=3.87Å (Section 4.4). Table 4.1 shows the results for LMTO and *spd* calculations for other metal pairs and MTO *spd* analysis of Pd/Ir. The $2AR_{Ir/Pd}$ values obtained for the two kinds of interfaces gave

   $2AR_{Ir/Pd}{}^{M}$TO-*spd*=1.21±0.10 $f\Omega m^2$ for perfectly flat interfaces.

   $2AR_{Ir/Pd}{}^{M}$TO- *spd*=1.22±0.10 $f\Omega m^2$ for interfaces of 2ML thick 50%-50% Ir-Pd alloy.

   The listed uncertainties allow the calculated Fermi energies for Ir and Pd to deviate from experiment by ±0.05eV [88]. These values don't quite overlap with our experimental best estimate result of $2AR_{Ir/Pd}$=1.02±0.06 $f\Omega m^2$.

2) Adding the extra f orbitals should give more accurate potentials and thus more accurate band structures. Xia and Wang updated their calculations of electronic structures in the LDA approximation to MTO analysis with an *spdf* orbital basis. Using the lattice parameter a_0=3.87Å and a FCC(111) crystal structure, the $2AR_{Ir/Pd}$ obtained for the two kinds of interfaces assumed were

   $2AR_{Ir/Pd}{}^{M}$TO-*spdf*=1.10±0.10 $f\Omega m^2$ for perfectly flat interfaces.

   $2AR_{Ir/Pd}{}^{M}$TO- *spdf*=1.13±0.10 $f\Omega m^2$ for interfaces of 2ML thick 50%-50% Ir-Pd alloy.

Both results now agree with the experimental value of

$2AR_{Ir/Pd}{}^{Exp}$=1.02±0.06 $f\Omega m^2$ within mutual uncertainties.

The agreement between the calculations for both perfect and alloyed interfaces can be

explained by the following discussion. In perfect interfaces the component of the crystal momentum parallel to the interfaces is conserved, ie, $k_{||}$ is conserved. In alloyed interfaces, the conservation of $k_{||}$ is relaxed. Hence the change in $2AR_{Ir/Pd}$ for alloyed interfaces is a result of two effects:

1) The relaxation of $k_{||}$ conservation increases the number of final states to which electrons can be scattered, thereby increasing electron conductance.

2) In contrast, scattering due to the interface disorder increases $2AR_{Ir/Pd}$.

For many lattice matched pairs, these two effects can roughly cancel.

As Table 4.1 shows, the results for Ag/Au, Co/Cu and Fe/Cr change only a little from the LMTO *spd* to MTO *spdf* calculations. For Pd/Pt the calculated MTO *spdf* changes by approximately 30% from the LMTO *spd* calculations, and agrees less well with the experimental best estimate.

4.6 Summary and Conclusions:

In this project, experiments and calculations were done separately in double blind, and then the results were shared. Experimentally, we determined the specific resistance of sputtered Ir/Pd interfaces to be $2AR_{Ir/Pd}$=1.02±0.06 $f\Omega m^2$. The calculations of $2AR_{Ir/Pd}$ were done for a common lattice parameter and common crystal structure of FCC (111) without adjustments. The following separate conditions were used:

1) *spd* MTO calculations for both perfectly flat and 2ML thick 50%50% random alloy of Ir and Pd. As shown in Table 4.1, the results were similar to our experimental value, but

Metals Structure	$(\Delta a/a_0)\%$	$2AR^{Exp}$ $(f\Omega m^2)$	2AR(Perf.) $(f\Omega m^2)$	2AR (50-50%) $(f\Omega m^2)$	2AR(Perf.) $(f\Omega m^2)$	2AR (50-50%) $(f\Omega m^2)$
Basis Prior Studies			LMTO *spd*	LMTO *spd*	MTO *spdf*	MTO *spdf*
Ag/Au (FCC) (111)	0.2	0.1[64]	0.09 [75][78]	0.12 [75][78]	0.09	0.13
Co/Cu (FCC) (111)	1.8	1.0[59]	0.9 [75][78]–[79]	1.1 [75][78]–[79]	0.9	1.1
Fe/Cr (BCC) (110)	0.4	1.6[68]	1.9[75], 1.5[76]	1.6[75]	1.7	1.5
Pd/Pt (FCC) (111)	0.8	0.28±0.06 [62]	0.30±0.04 [62]	0.33±0.05 [62]	$0.40^{+0.03}_{-0.08}$	$0.42^{+0.02}_{-0.04}$
Basis Present Study			MTO *spd*	MTO *spd*	MTO *spdf*	MTO *spdf*
Ir/Pd (FCC) (111)	1.3	1.02±0.06	1.21±0.10	1.22±0.10	1.10 ±0.10	1.13 ±0.10

Table 4.1: Comparison of experimental values of 2AR interface with calculations. Listed uncertainties allow calculated Ir/Pd Fermi energy to deviate from experiment by ±0.05eV [91].

didn't quite overlap within the mutual uncertainties.

2) *spdf* MTO calculations for both perfectly flat and 2ML thick 50%-50% random alloy for Ir and Pd. Now the calculations agreed with our experimental best estimate to within mutual uncertainties.

To conclude, calculations by Xia and Wang agree reasonably well with our experimental value of $2\mathrm{AR}_{Ir/Pd}$, with no adjustable parameters. The *spdf* MTO calculations agree somewhat better with the experimental best estimate.

Chapter 5

Determination of Spin Flipping behavior in antiferromagnets IrMn and FeMn

This Chapter expands upon published results in [92] and [93].

5.1 Introduction and Motivation:

Antiferromagnets (AF),such as IrMn and FeMn, are widely used in Spintronics studies. In Giant Magnetoresistance, Exchange Biased Spin Valve devices use AFs as a pinning layer for adjacent ferromagnetic layers using exchange bias coupling [36] [94]–[95]. They also form an essential part of Antiferromagnetic GMR (AFGMR) studies [96] [97]. Since AF's are widely used in the CPP geometry, it is important to know their transport properties, including the spin diffusion length of the AF layers and the spin flipping properties of AF/N interfaces. In

2000, Park et al[63] conducted experiments to determine the interfacial resistance and spin relaxation in non magnetic metals and non magnetic interfaces using a technique (Section 2.3.2) that involved inserting the non-magnetic metal of interest into the middle of the 20nm thick Cu layer center layer in a Py (Permalloy- NiFe) based Exchange Biased Spin-Valve. They used the same technique to try to determine the spin diffusion length of the antferromagnetic alloy $Fe_{50}Mn_{50}$. They found that as little as 1nm of FeMn inserted into the middle of the 20nm Cu caused the CPP MR to drop by a factor of 400 (Figure 2.4). They attributed the rapid drop in CPP MR to strong spin flipping at the FeMn/Cu interface. They couldn't extend the studies to beyond 2nm thick FeMn because by then the CPP MR was so small ($\sim$0.001 $f\Omega m^2$) that it became comparable to the uncertainty in their data.
In the present study we use the same technique to determine the unknown spin flipping properties of the antiferromagnet $Ir_{20}Mn_{80}$ and its interface with Cu. IrMn is widely used in devices because of its greater stability at higher temperatures as compared to FeMn. Motivated by our findings in the IrMn study, we also extend the spin flipping study on FeMn to thicker FeMn insert layers.

The present chapter is organized as follows. We start with the sample structure design, the basic idea of our experiment, and sample fabrication and measurement processes. We then present our study with N=IrMn inserts which is divided into two parts, $t_{IrMn} \leq$5nm and $t_{IrMn} \leq$30nm, based on our published papers [92] [93]. Finally we present a similar study of N=FeMn inserts extended to $t_{FeMn} \leq$30nm.

5.2 Samples and Spin diffusion length determination technique

The theoretical analysis is based on the Valet Fert model and is discussed in Section 2.3.2. The sample structure, as described there, consists of a Py based EBSV with an N insert. In our case the N insert is an antiferromagnet AF layer of the alloy (IrMn or FeMn) of interest. The complete sample structure is given as FeMn(8nm)/Py(24nm)/Cu(10nm)/N(t_N)/ Cu(10nm)/Py(24nm).

5.3 Sample Measurement:

The samples are deposited using room temperature sputtering as described in Section 3.2.1. The EBSV samples were pinned (Section 3.1) prior to the measurement of R, measured using the SQUID based potentiometer circuit (Section 3.3.4). Figure 5.1a shows sweeps from -H to +H for a sample with t_{IrMn}= 0nm i.e. no N= IrMn insert between the Cu in the EBSV structure. At -150 Oe, the two Py layer magnetizations are parallel (P) to each other because the magnetic field is oriented in the direction of the pinned Py layer. At about +20 Oe the free Py layer moment flips to give an antiparallel (AP) state, and when the magnetic field is taken to a large enough positive field of +H= +300 Oe, the pinned layer flips to give a parallel (P) state again. As the field is reduced, the pinned F layer, with its asymmetric hysteresis about zero field (Section 1.6), tends to align along its preferred direction of magnetization (pinning direction) giving back an AP state. As the field becomes negative, the free F layer

switches its magnetization along the pinned layer giving back the P state. Negative fields of -150 Oe or larger (such as -200 or -300 Oe) and H $\geq$ +200 Oe gave well defined P states, which give the same AR to within experimental uncertainty. The AP state is well defined at 50 Oe.

The -H to +H sweep for a sample with IrMn insert thickness t_{IrMn} = 0.6nm is shown in Figure 5.1b. Compared to Figure 5.1a, the AΔR shrinks as the insert is introduced, giving a decrease in signal to noise ratio. Beyond a thickness of IrMn =1nm the signal becomes comparable to the uncertainty in R. Therefore, to measure AΔR beyond t_{IrMn}=1nm, we used the following strategy. First, we put the superconducting magnet that produces the field in a persistent mode using a superconducting shorting switch. Measurements in persistent mode reduce fluctuations in field H during resistance measurements. Second, we averaged 100 measurements of R at -150, -200 or -300 Oe, then 100 measurements of R at +50 Oe, and finally 100 measurements of R at +300 Oe. We then repeated the same cycle. Finally we found R(P) by averaging the four average values at -H = -150 Oe (alternatively -200 Oe or -300 Oe) and +H = 300 Oe. R(AP) was obtained by averaging the two average R values at +50 Oe. We took the difference of these averages to be our best estimate of ΔR, and used the standard deviation of the mean to obtain the uncertainty in ΔR. We then multiplied ΔR with the area of the sample (Section 3.3.2) to obtain AΔR .

To check reproducibility and sensitivity of our samples, we measured more than one sample for each thickness of IrMn. In some samples, there are one or two outliers among the 600 data points, which we could relate to flux jumps in the SQUID measurement by looking at the raw data. These outliers are discussed in Appendix A. As an example to show

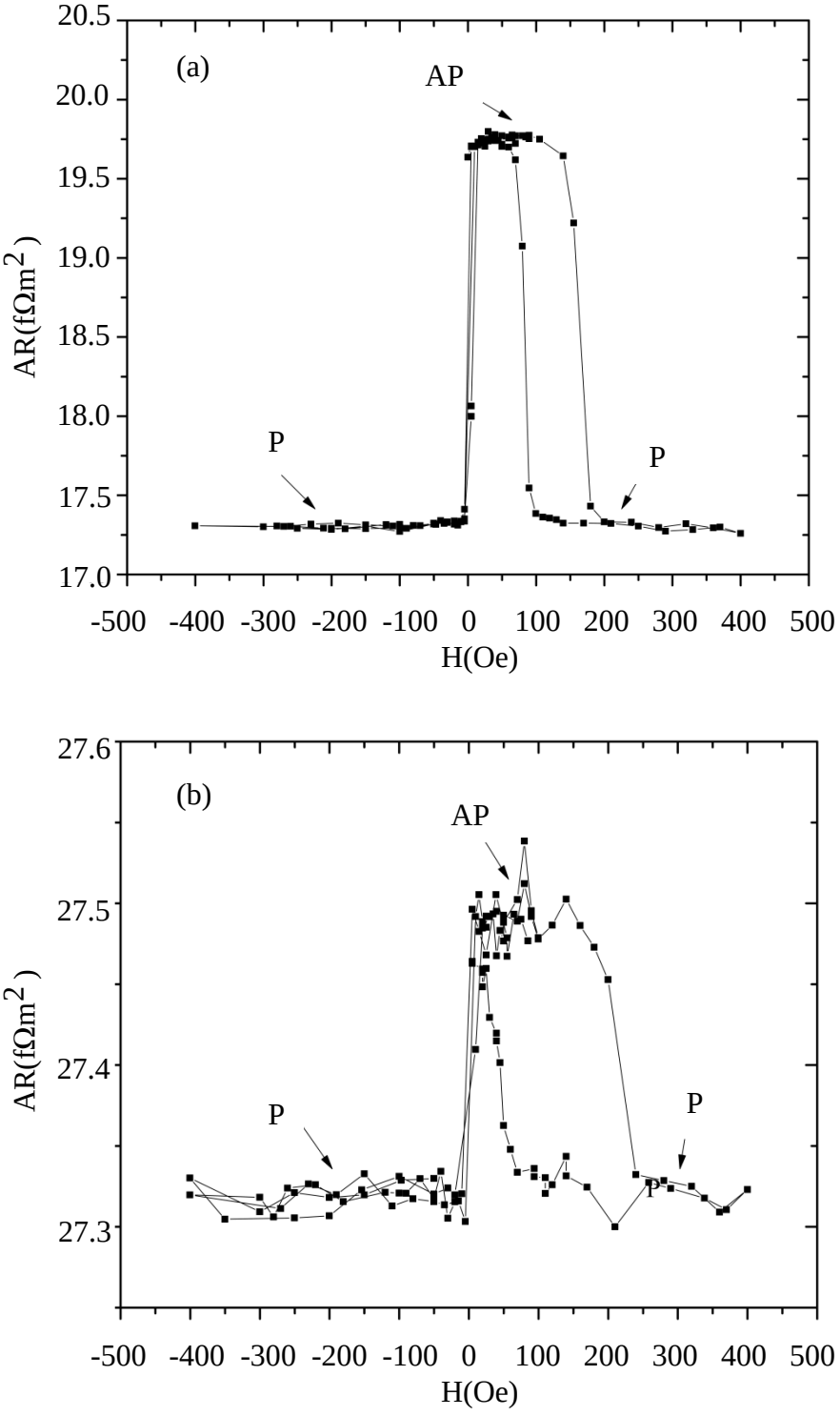

Figure 5.1: Magnetic Field sweeps from -H to +H for (a) $t_{IrMn} = 0$nm and (b) t_{IrMn}=0.6nm [92]

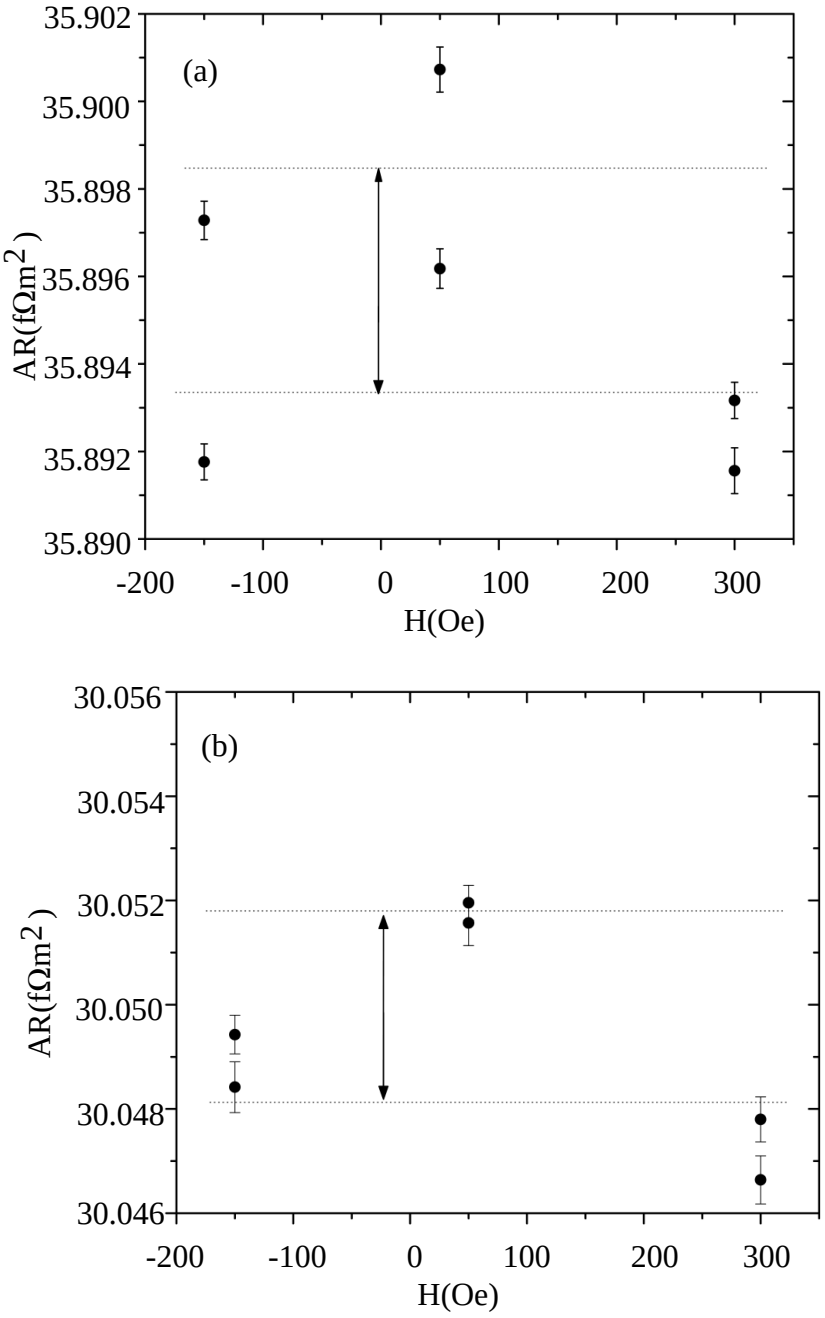

Figure 5.2: Magnetic Field variations of AR of two different 5nm samples. We take 2 X 100 measurements at -150 Oe, +50 Oe, or +300 Oe and their averages are shown using filled circles. The two dotted lines represent the average value of the nominal AP and P state AR values. The arrow connecting the two dotted lines represents the value of AΔR for the two samples. (a) AΔR = 0.0037$\pm$0.0004 $f\Omega\mathrm{m}^2$ (b) AΔR = 0.0050$\pm$0.0005 $f\Omega\mathrm{m}^2$ [93].

the reproducibility of our data, Figure 5.2 compares two independent t_{IrMn} = 5nm samples that had no outliers.

5.4 Data Analysis

Our first study was done with N= IrMn inserts up to t_{IrMn}= 5nm [92]. This was followed by N=IrMn inserts up to $t_{IrMn} \leq$ 30nm, and then N =FeMn inserts up to t_{FeMn}= 30nm [93]. The following sections discuss the data analysis of the studies in this order.

5.4.1 N=IrMn insert for t_N up to 5nm

In 2000, Park et al [63] used the technique of embedded N inserts in the middle of a 20nm thick Cu layer, in a Py based EBSV sample, to measure the spin flipping properties of the N metal insert. The data for most inserts could be understood as involving an initial decay in $A\Delta R$ due to a growth of AR_N from Section 2.3.2, Equations 2.41 and 2.42, with increasing t_N due to the growing interfaces between the insert N and the bounding Cu, followed by a slower decay due to a finite ${\ell_{sf}}^N$.

For FeMn, however, the initial decay was too rapid to be so explained. It was attributed instead to strong spin flipping in the developing interface. After $t_N \sim$1nm, the decay appeared to slow down, but the values of $A\Delta R$ were so small and the uncertainty so large, that the presence of slowing in the bulk was not absolutely sure.

Motivated by their results, we decided to start with the same N insert technique for another popular antiferromagnet IrMn. The expectation of seeing an initial rapid decay at the IrMn/Cu interfaces followed by a slower decay in the bulk of IrMn led us to start with

experiments with inserts up to an IrMn insert thickness, t_{IrMn}=5nm.

Figure 5.3 shows log AΔR versus t_{IrMn} for our IrMn samples up to t_{IrMn}=5nm. For comparison, the open inverted triangles are the Park data for FeMn inserts. We expect sputtered interfaces to be mixed to about 3-4 monolayers [64], which implies that till an IrMn insert thickness of $\sim$1nm, the two interfaces of IrMn/Cu are still forming. Within the growing interface thickness, there is a disordered mixture/alloy of IrMn and Cu. Therefore bulk IrMn, without any Cu mixture, should begin to form only after $\sim$1nm. In Figure 5.3, the data for t_{IrMn} = 0nm show AΔR for a simple FeMn(8)/Py(24)/Cu(20)/Py(24) EBSV structure, which is consistent with the previously obtained value of about $\sim$2 $f\Omega m^2$ for a Py EBSV structure by Park et al [63].

If we concentrate on the data for IrMn till t_{IrMn} $\sim$1nm, the fall-off of AΔR with increasing t_{IrMn} is much faster than expected from the growing interface contribution due to $\frac{1}{AR_0 + AR_N}$. So we attribute it to a strong contribution due to $exp(-\frac{2t_N}{2t_I}(\frac{2t_I}{{\ell_{sf}}^I})$ which dominates up to $t_N \sim t_I$. We estimated the spin diffusion length of the interface, using the slope of the line that passes through the data till t_{IrMn}=1.2nm in Figure 5.3. If we choose the t_I=0.6nm, the maximum t for which a single straight line can be fit to the log(AΔR) versus t_N data, then from $exp(-\frac{2t_N}{2t_I}(\frac{2t_I}{{\ell_{sf}}^I})$ we find ${\ell_{sf}}^I$=0.24nm, and from the relation $\delta = t_I/{\ell_{sf}}^I$ we find δ=2.5.

We see in Figure 5.3 that the AΔR values for IrMn inserts (filled squares) are larger than those for FeMn (open inverted triangles), and that the decay in AΔR is slower in IrMn than the decay in FeMn (from Park et al), after the formation of the interfaces. This behavior in IrMn, in comparison with FeMn, let us study thicker inserts of IrMn as compared to FeMn. With the data extended to t_{IrMn}=5nm, we did a complete analysis by fitting the Valet Fert

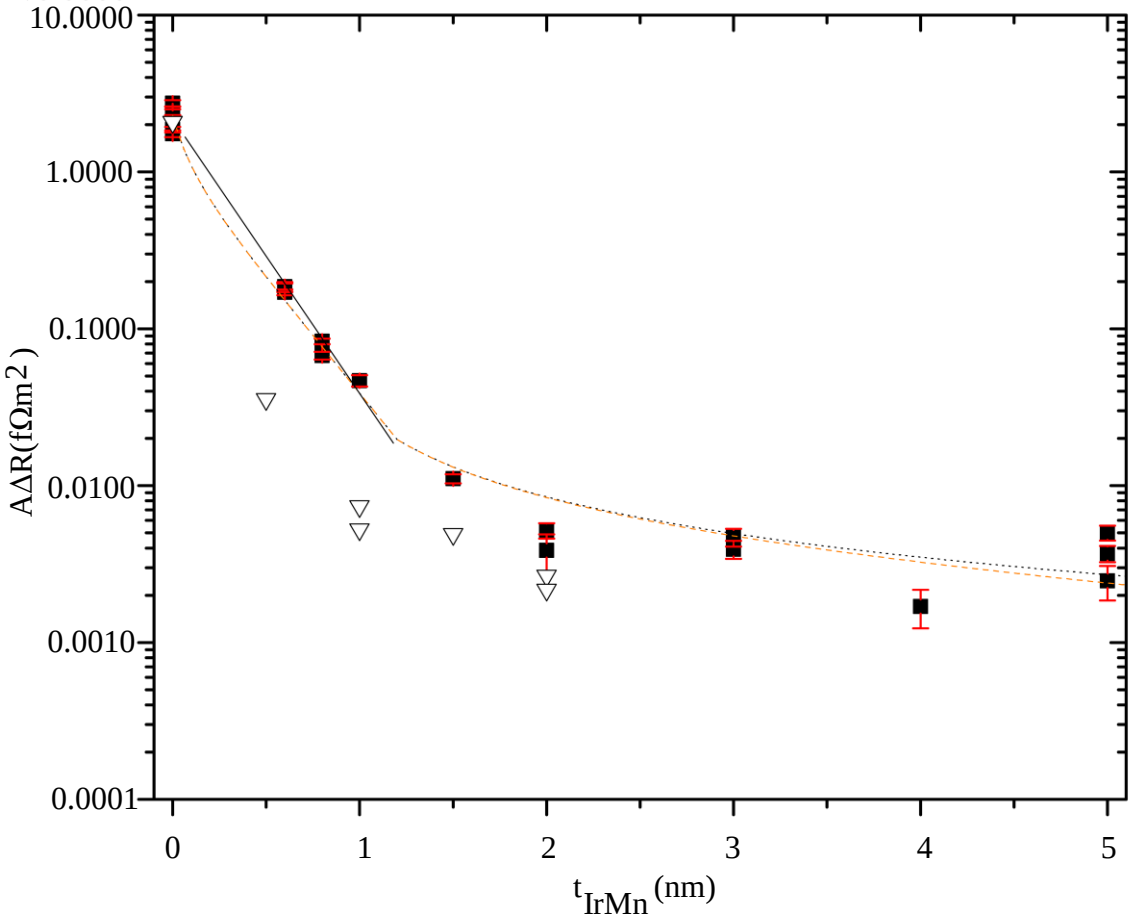

Figure 5.3: AΔR versus t_{IrMn} shown by filled black squares. Open triangles show the FeMn data from Park et al [63]. The slope of the solid line till $t_{IrMn} = 1.2$nm which corresponds to $2t_I$ gives a spin diffusion length = 0.24nm for the interface. The dotted curve fit gives a ${\ell_{sf}}^{IrMn} = \infty$. The dashed curve fit gives a ${\ell_{sf}}^{IrMn}$=5nm. For both fits ${\ell_{sf}}^{I} = 0.295$nm

model (Section 2.2) using a bulk IrMn resistivity obtained from VdP measurements of IrMn films (Section 3.3.3). From the fit to the VF model, we found a slightly larger ${\ell_{sf}}^{IrMn/Cu}$ $\sim$ 0.295nm for the IrMn/Cu interface. The bulk, however, could be fit with a wide range of bulk spin diffusion lengths.

Figure 5.3 shows VF fits with assumed $t_I = 0.6$nm, interface spin diffusion length ${\ell_{sf}}^{I}$=0.295nm, and bulk spin diffusion lengths ${\ell_{sf}}^{IrMn}$=5nm (dashed curve) and ${\ell_{sf}}^{IrMn} = \infty$ (dotted curve). The two fits to the bulk data up to t_{IrMn}=5nm are essentially indistinguishable within the uncertainty of the data. Thus we needed to extend our study to thicker IrMn to clarify the spin flipping behavior in the bulk of IrMn.

5.4.2 N= IrMn for t_{IrMn} upto 30nm

From Figure 5.3, we concluded that the fit to the data for IrMn up to t_{IrMn}=5nm is insensitive to the spin diffusion length in the bulk of IrMn. Thus, to try to determine the bulk spin diffusion length, we extended our studies to t_{IrMn}=30nm.

The resulting values of AR(AP) and AΔR versus t_{IrMn} are shown in Figures 5.4 and 5.5. From the slope of the plot of AR(AP) versus t_{IrMn} in Figure 5.4, we obtain a resistivity for IrMn of 1260$\pm$70 nΩm, compatible with the value of 1500$\pm$110 nΩm obtained from VdP measurements (Section 3.3.3) on separately sputtered IrMn films.

From Equation 2.42 for $t_{IrMn} > {\ell_{sf}}^{IrMn}$, we would expect A$\Delta$R to decrease approximately exponentially with t_{IrMn} as illustrated by the dotted or dashed curve in Figure 5.5 for ${\ell_{sf}}^{IrMn} = \infty$ or ${\ell_{sf}}^{IrMn}$=5nm. Instead, AΔR becomes approximately constant at 0.0037$\pm$0.0002 $f\Omega m^2$ for $t_{IrMn} \leq$5nm. We will see in Section 5.5 that this constant

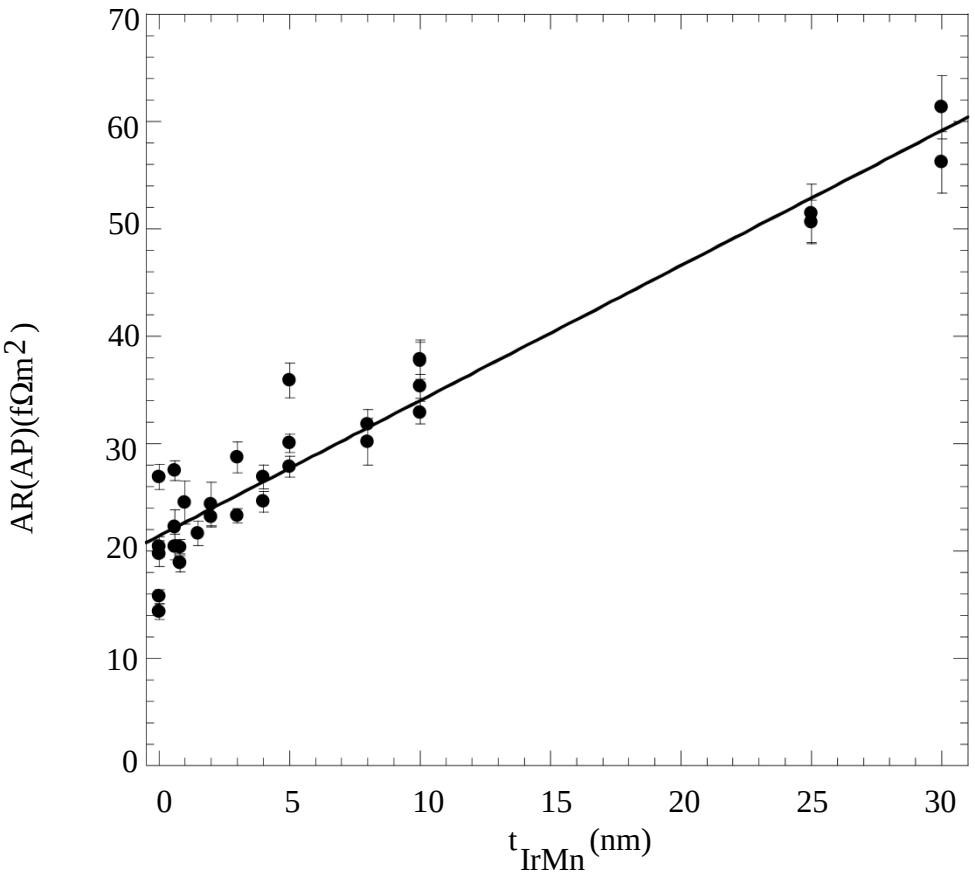

Figure 5.4: AR(AP) versus t_{IrMn}. The slope of the line through the data gives the resistivity of IrMn. Slope = 1260±70 nΩm. This value is consistent with the 1500±110 nΩm obtained using VdP measurements of resistivity on IrMn sputtered films.

value/background is unrelated to IrMn. The uncertainty in this constant background limits our aility to constrain ${\ell_{sf}}^{IrMn}$. The dot-dash curve in Figure 5.5 indicates a fit to the entire data set, combining the constant background with spin diffusion lengths of 0.295nm for both the interface IrMn/Cu and bulk IrMn.

Clearly the data are consistent with a short bulk ${\ell_{sf}}^{IrMn}$. However uncertainties in both the interface δ and the background make it impossible to constrain the bulk ${\ell_{sf}}^{IrMn}$ very

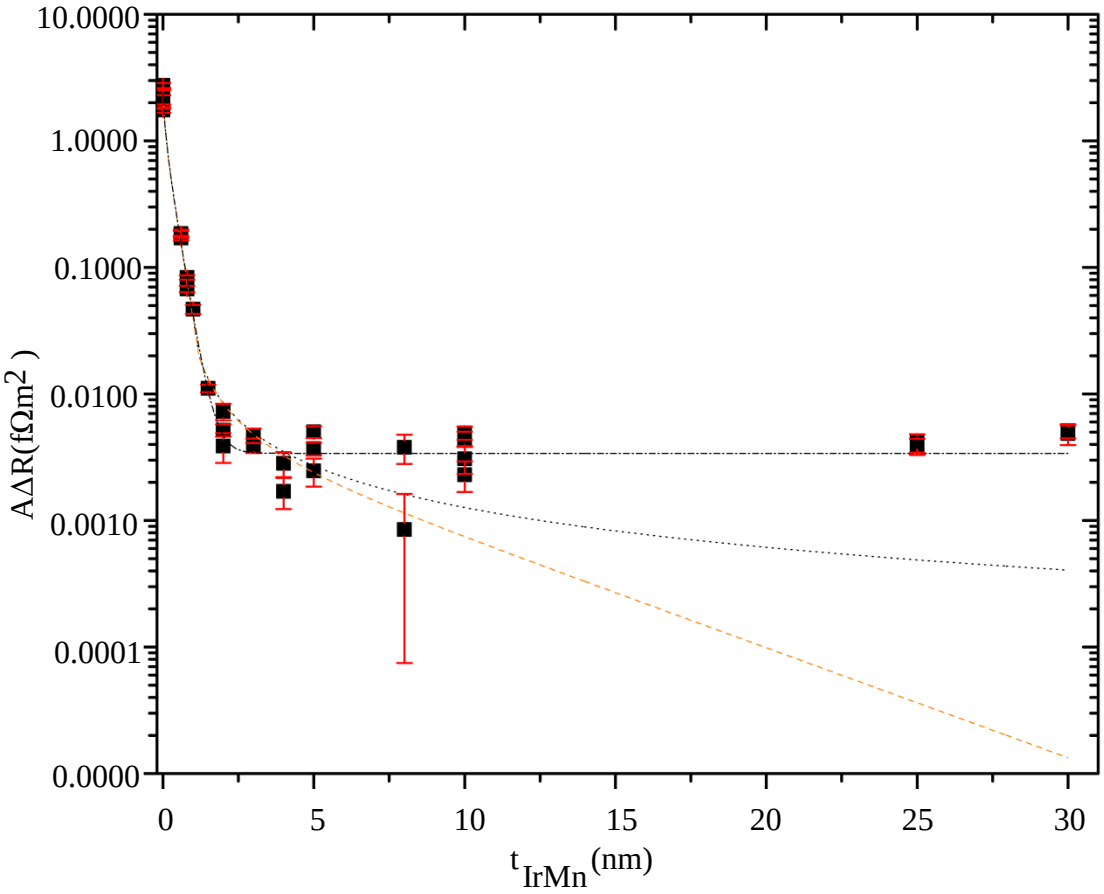

Figure 5.5: AΔR versus t_{IrMn}. The filled squares are the AΔR values for varying thickness. The dotted curve is a fit to the data with ${\ell_{sf}}^{IrMn} = \infty$ for the bulk IrMn. The dashed curve is fit to the data with ${\ell_{sf}}^{IrMn}$=5nm. For both the dotted and the dashed curve fits, the IrMn/Cu interface spin diffusion length = 0.295nm. The dot dashed curve is a fit to the entire data with a constant background of 0.0037 ± 0.0002 $f\Omega m^2$ and ${\ell_{sf}}^{IrMn} = 0.295$nm for both the IrMn/Cu interface and IrMn bulk.

well. It is, however, most likely to be short, probably of the order of 1nm or less.

5.5 Test for the source of the constant background:

At this point we needed to understand the origin of this constant value of AΔR , and whether it was related to CPP GMR. To do so, we remeasured some of our samples with $t_{IrMn} \leq$ 1.5nm at magnetic fields -300 Oe, -50 Oe, 50 Oe and 300 Oe. This procedure was used for the following reasons:

1) We should get a well defined P state at -300 Oe and 300 Oe when both the free and pinned Py layers are aligned parallel to each other.

2) The free Py layer switches, opposite to the pinned Py layer direction, by +20 Oe to give the AP state. The pinned Py switches at $\sim$ 180 Oe opposite to the pinning direction. Therefore the AP state should be well defined at + 50 Oe.

3) The Py layers should still be aligned parallel to each other at -50 Oe, so if there is a usual CPP-GMR, we should expect AR(-50 Oe) to be similar, within uncertainty, to AR(-300 Oe) and AR(+300 Oe).

In Figure 5.6, we compare AR versus H (Oe) for two samples of t_{IrMn} =30nm. In both samples, AR(-50 Oe) is closer to AR(+50 Oe) than to AR(-300 Oe) and AR(+300 Oe). A higher AR value at -50 Oe should not be considered a CPP GMR signal. Also, the difference between AR (-50 Oe) and the average AR_P (average of AR(-300 Oe) and AR(+300 Oe) were $\sim$ 0.004- 0.005 $f\Omega m^2$, comparable to the increase in AR(+ 50 Oe).

Having clarified that the source of the constant value is not a CPP GMR signal, we explored

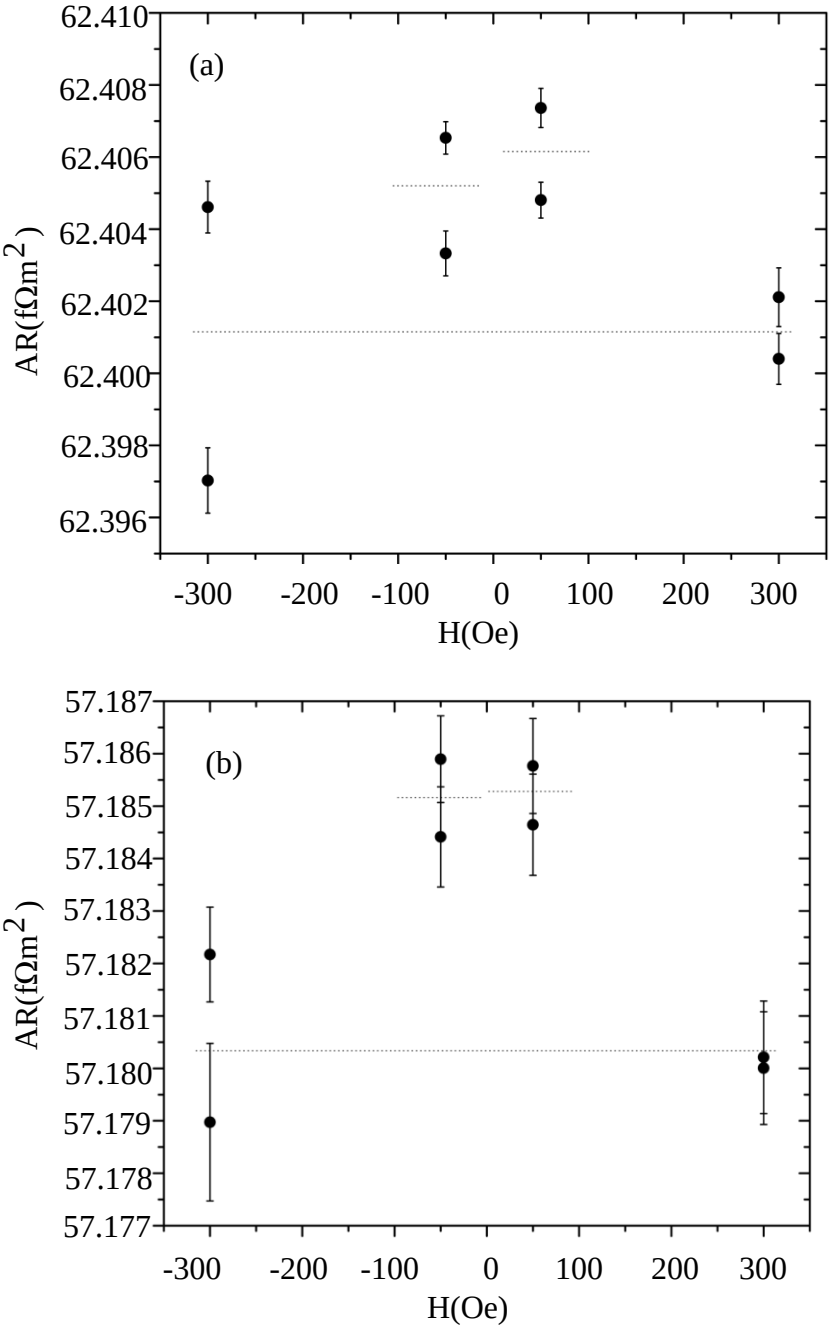

Figure 5.6: (a) and (b) show two t_{IrMn}= 30nm samples with AR(-50 Oe) closer to AR(+50 Oe) than to AR(-300 Oe) and AR(+300 Oe).[93]

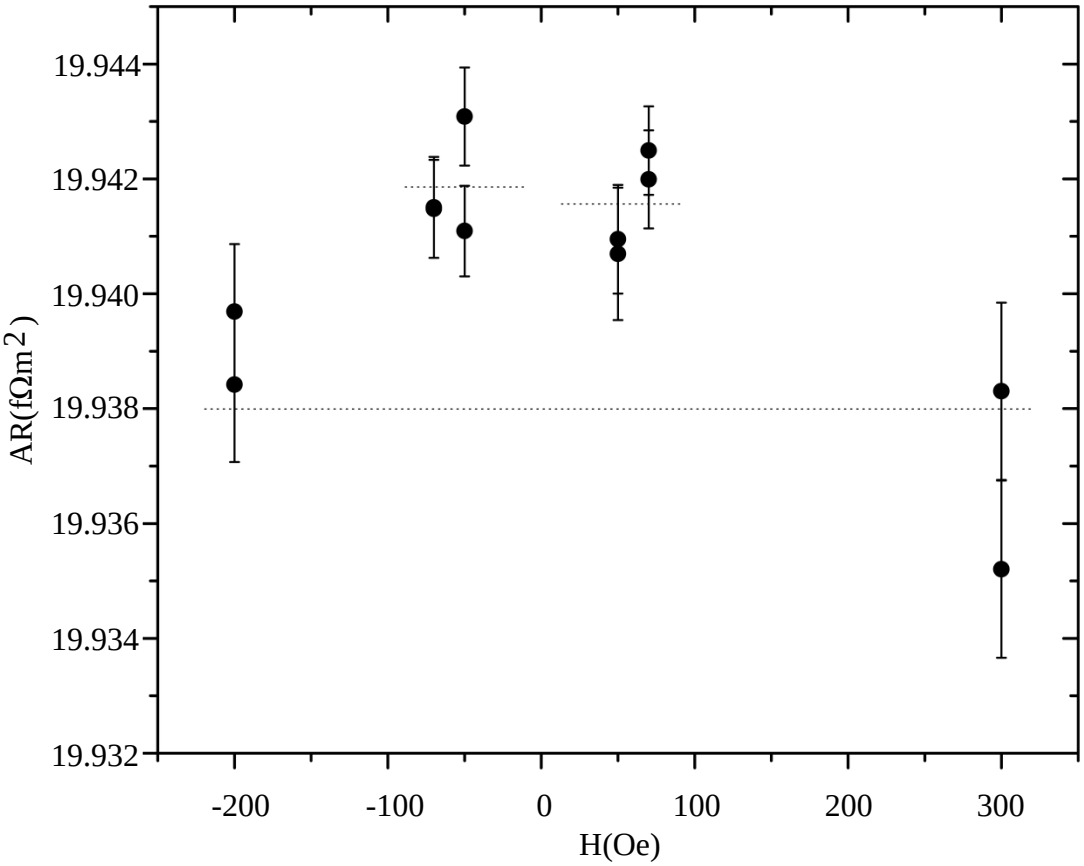

Figure 5.7: AR versus H for FeMn(8nm)/Py(24nm) sample.

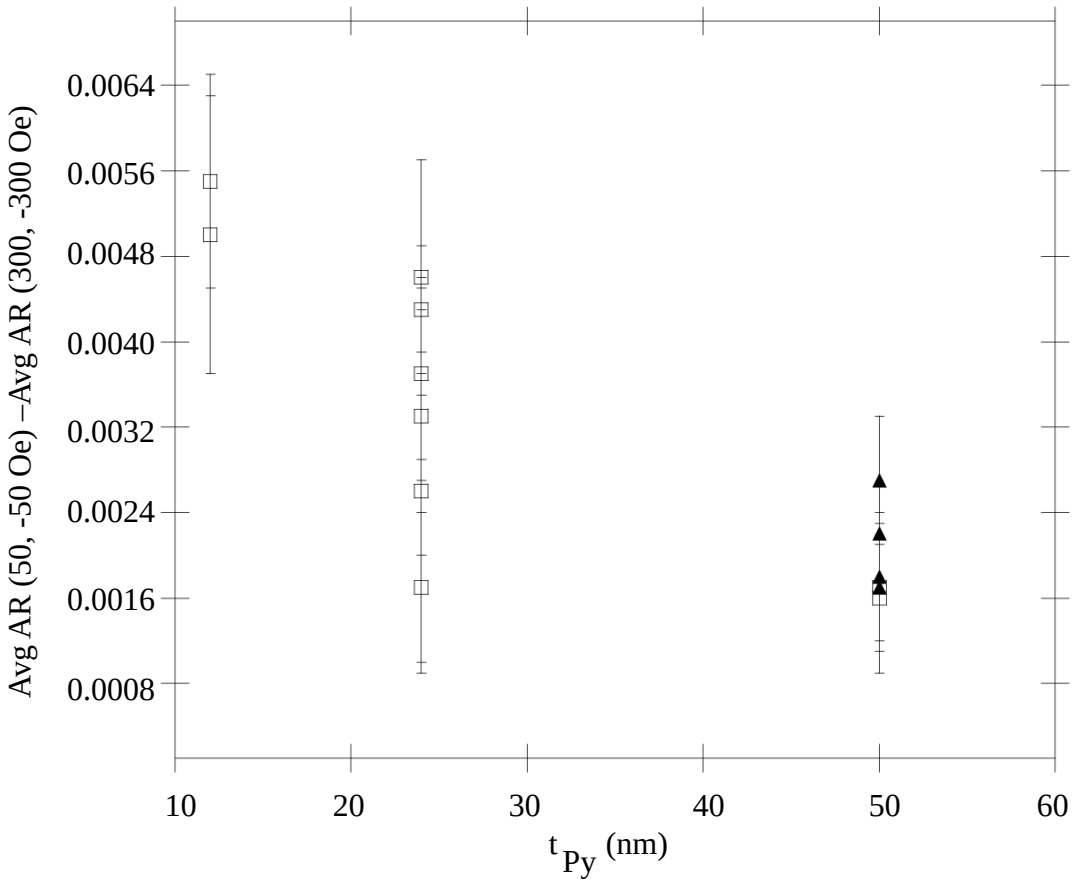

Figure 5.8: AΔR versus t(nm) of Py. Filled triangles show the variation of AR for single Py layers. Open squares show the variation of AR for Py grown adjacent to FeMn.

the possibility of the source being a part of the multilayer other than the IrMn insert. The next attempt was to see if it was associated with the Py in the multilayer structure. We made samples with the following CPP S structures:

1) Cu(5)/Py(50)/Cu(5)

2) FeMn(8)/Py(t) or Py(t)/FeMn(8) with t =50,24 and 12nm.

We measured type (b) samples both with and without field pinning. We measured AR of these samples at -200 Oe, -70 Oe, -50 Oe,+50 Oe, +70 Oe and +300 Oe and then repeated the sequence. Figure 5.7 shows AR versus H for a FeMn(8)/Py(24) sample at these different fields. The average AR at -70 and -50 Oe is larger than the average AR at -200 and 300 Oe and is comparable to the average AR at 50 and 70 Oe. This difference of average AR at -70 and -50 Oe with respect to the average AR at -200 and 300 Oe was not sensitive to pinning but grew modestly with decreasing t as shown in Figure 5.8. This growth is not yet understood. The overall average of $A\Delta R\,(Py) = 0.003\pm0.001\ f\Omega m^2$, is comparable to the constant value observed in our $A\Delta R$ signals for $t_{IrMn}\geq$4nm.
Therefore we conclude that the constant term most likely arises from some new effect associated with just the Py layers.

5.6 N=FeMn insert for t_{FeMn} up to 30nm:

The unexpected results for $t_{IrMn}\geq$5nm motivated us to extend similar measurements to FeMn inserts of thicknesses greater than 5nm. Park et al[63] had already shown a rapid decay in spin polarization at FeMn/Cu interfaces. However, as mentioned before, the behavior

in the bulk was inconclusive since the AΔR signal was very small and comparable with the uncertainty. As an extension to their study, we introduced an N = FeMn insert in the CPP S sample structure FeMn(8)/Py(24nm)/Cu(10nm)/[N=FeMn (t_{FeMn})]/Cu(10nm)/Py(24nm) up to t_{FeMn}=30nm.

First we plot AR(AP) versus t_{FeMn} (Figure 5.9) whose slope gives the resistivity of FeMn, $\rho_{FeMn} = 680 \pm 30 n\Omega m$. Although this value of FeMn resistivity is close to the previously measured VdP value of 875±50 nΩm[40] for FeMn, within experimental uncertainty, it is not quite consistent with the measured VdP of our FeMn sputtered films. Our sputtered FeMn films from a 2.25" target, gave a much larger resistivity of 1230±130 nΩm, and from 1" target gave a resistivity of 1000±220 nΩm. The two values obtained from our sputtered films from the small and the large targets and the previous value of of 875±50 nΩm [40] are all comparable, but only overlap in pairs, within their uncertainties.

Figure 5.10 shows a plot of AΔR versus t_{FeMn} for $t_{FeMn} \leq$30nm using filled circles for our new data. The initial drop in AΔR is slower and the AΔR values are larger, than the Park et al[63] data shown as inverted open triangles. Our larger values of AΔR let us extend our studies beyond the t_{FeMn}=2nm thickness studied by Park. Similar to our results for IrMn, AΔR becomes approximately constant, at 0.003±0.001 $f\Omega m^2$. We fit our data to the VF model. The resulting fits are shown in Figure 5.10. The choice of the interface thickness is again based on the 'knee' in the plot where the round off from the interface formation to the bulk behavior begins. t_I=0.8nm is consistent with the observed 3-4ML of sputtered interface thicknesses [64]. The solid curve in Figure 5.10 represents the fit to the entire data including the constant background, with ${\ell_{lsf}}^{FeMn/Cu} = 0.34$nm and ${\ell_{lsf}}^{FeMn}$=0.6nm. The

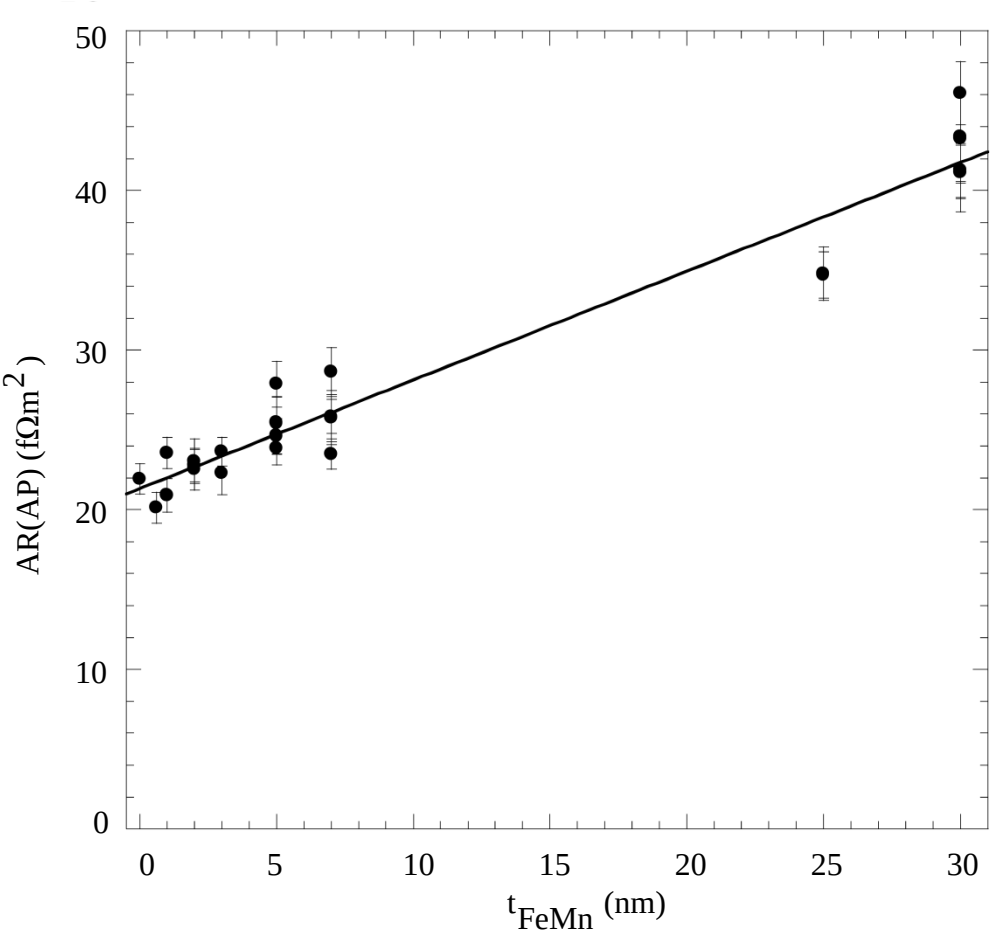

Figure 5.9: AR(AP) versus t_{FeMn}. The slope of the line gives the resistivity of FeMn. The slope = 680±30 nΩm.

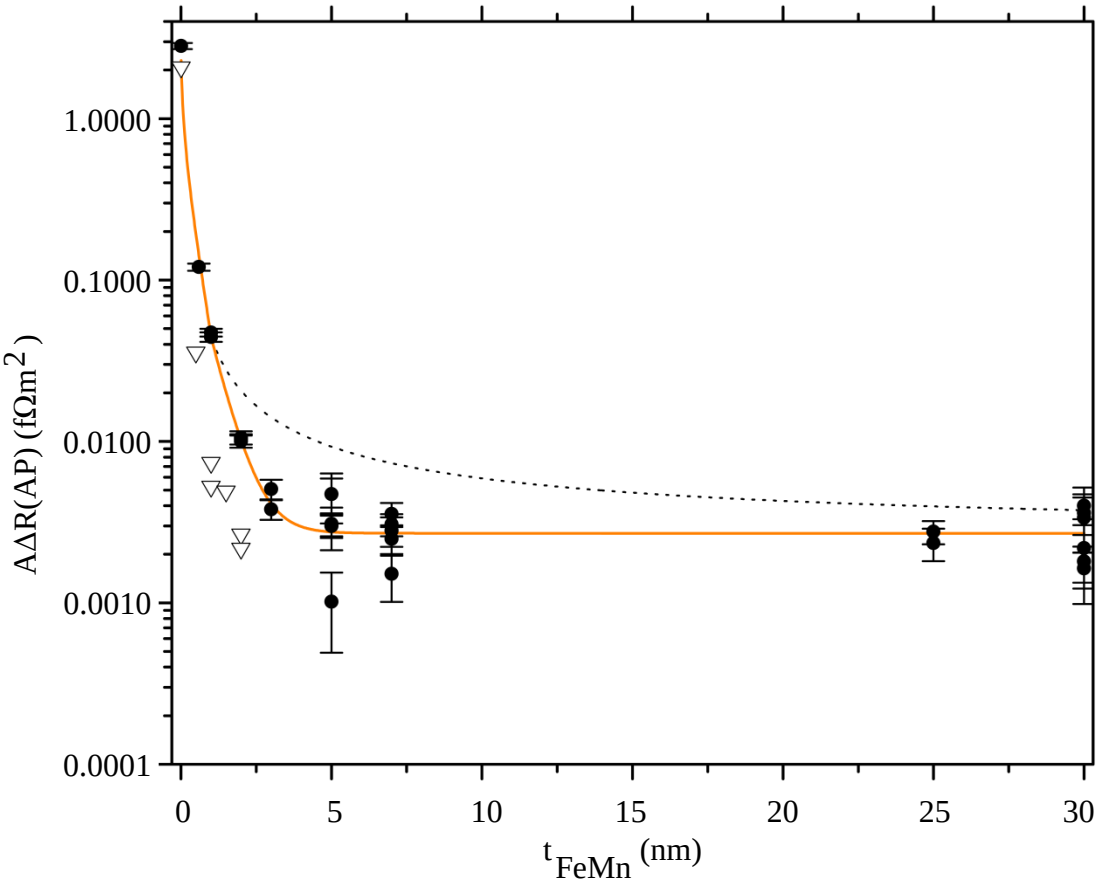

Figure 5.10: AΔR versus t_{FeMn}.The solid curve fit in Figure 5.10 represents the fit to the entire data including the constant background, and ${\ell_{lsf}}^{FeMn/Cu} = 0.34$nm and ${\ell_{lsf}}^{FeMn}$=0.6nm. The dashed curve represents the same case except with ${\ell_{lsf}}^{FeMn} = \infty$.

dashed curve represents the same case except with ${\ell_{sf}}^{FeMn} = \infty$. Similar to IrMn, there is strong spin flipping at the FeMn/Cu interfaces and we are unable to put a tight bound on the ${\ell_{sf}}^{FeMn}$ in the bulk of FeMn. However, given the lack of excess AΔR over the constant background, it is most likely short, probably of the order of 1nm.

5.7 Modification of spin-flipping at the interface with Cu

From our observation of the spin flipping behavior of FeMn and IrMn it is clear that there is strong spin flipping at their interfaces with Cu. By the time the electrons cross the AF/Cu interfaces, the signal strength is greatly reduced, making it difficult to distinguish the effects of the bulk. The next step was to see if we could reduce spin flipping at AF/Cu interfaces to better observe spin flipping behavior in the bulk of the AF. If the interface spin flipping is dominated by "loose" Mn moments mixed in Cu, then maybe replacing Cu would give larger AΔR due to weaker interface spin flipping. From studies of the Kondo Effect[96], we chose Nb and Ru inserts between Cu and IrMn (FeMn). Kondo effect studies suggest that Mn should not have loose moments in Nb or Ru. Hence such inserts should most likely be able to reduce the spin flipping at the interface.

We introduced 1-5nm of Nb and Ru between IrMn and Cu. Figure 5.11 shows our original data along with the measurements done on samples with the inserts. Although we found a few cases of larger AΔR , we also found as many or even more cases with smaller AΔR than the original data without the Nb or Ru inserts. On remeasuring one of the samples with

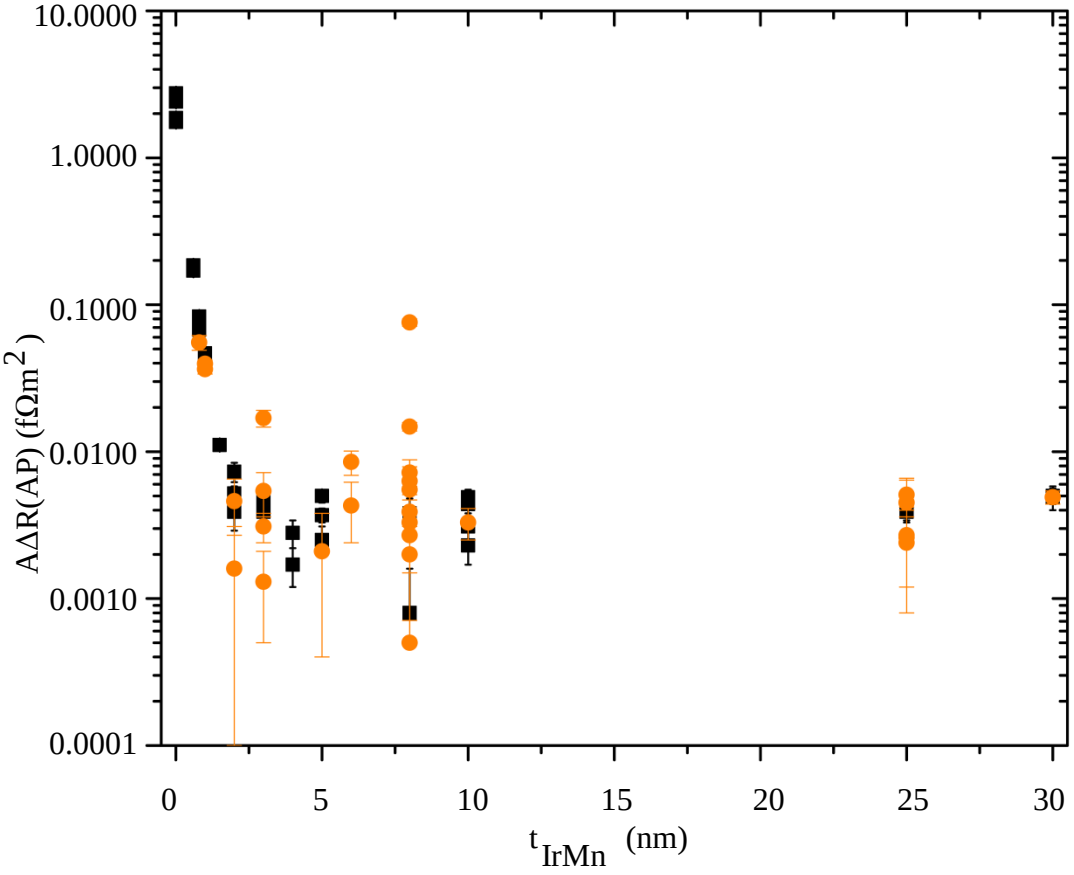

Figure 5.11: AΔR versus t_{IrMn} with the filled squares showing our data without any Nb or Ru inserts. Filled orange circles are data with 1-5nm of Nb and Ru inserts.

large AΔR (#1919-7, measured a year later) with t_{IrMn}=8nm and Nb insert of 1nm, the AΔR shifted to a lower value similar to the data without any Nb or Ru inserts at IrMn/Cu interfaces. Therefore, on an average, there is no systematic variation in the signal over the original. Hence we can conclude that the loose moments of Mn in Cu are probably not the source of the strong spin flipping at the IrMn/Cu interface.

5.8 Conclusion:

Using CPP MR measurements, of Py based EBSV with an insert N with varying thickness, we studied the spin flipping behavior in antiferromagnet inserts N= IrMn and N=FeMn and their interfaces with Cu. The decay in the AΔR signal with increasing t_N provides information about the spin diffusion lengths at the N/Cu interfaces and bulk N using the Valet Fert model. Our initial study of IrMn to thickness $t_{IrMn} \leq$5nm showed rapid decay in the AΔR signal till $t_{IrMn} \sim$2nm and a slower decay thereafter. This study indicated a strong spin flipping at the IrMn/Cu interface and the possibility of a longer spin diffusion length in the bulk of IrMn. To gain more information on the bulk IrMn spin flipping behavior, we extended the study to thicker IrMn inserts with t_{IrMn} up to 30nm. Instead of an additional decay in AΔR , the signal became approximately a constant at $0.0037 \pm 0.0002\ f\Omega m^2$. Similar behavior was observed with N=FeMn inserts. We summarize our results as follows:

1) There is strong spin flipping at IrMn/Cu interfaces and the spin diffusion length in the bulk of IrMn is most likely short, probably of the order of a 1nm.

2) There is similar spin flipping behavior observed in FeMn with strong spin flipping at the FeMn/Cu interfaces and a spin diffusion length probably of the order of a 1nm in the bulk of FeMn.

3) Studies to discover the origin of the constant signal showed that it is unrelated to a CPP GMR, and linked it to a field dependence of AR in Py.

4) Through attempts to reduce spin flipping at the IrMn/Cu interfaces, we were able to show that the spin flipping at the interfaces is probably not due to loose Mn moments in

Cu.

Chapter 6

Growth of epitaxial CFAS (Co_2Fe $Al_{0.5}Si_{0.5}$) Heusler alloy to observe CPP MR properties using CFAS based spin valves.

6.1 Introduction and Motivation

Because of their potential ability to produce 100% spin-polarization of transport elecrons, compounds that approximate half-metals are exciting a lot of interest in the field of Magnetoresistance [99]. A half-metal is a metal with mobile electronic states at the Fermi Energy, E_F, only for electrons with one moment orientation (majority), but not for those with the opposite moment orientation (minority). A schematic of the expected difference between

the band structures of minority and majority moment-electrons in a half metal is shown in Figure 6.1. For majority electrons, the Fermi Energy, E_F, falls within the conduction band, as usual for metals. For minority electrons, in contrast, E_F lies in the middle of an energy gap, as usual for semi-conductors. If unpolarized electrons are sent into such a half-metal, the majority band electrons should pass through, whereas the minority band electrons should be completely reflected. An ideal half metal should thus give bulk asymmetry parameter $\beta = 1$, and generate a very large CPP-MR, of great interest for magnetoresistive devices.

The possibility of half metallicity was first raised in 1983 by de Groot and collaborators [100], through first principles electronic structure calculations on the compound, NiMnSb. Such an XYZ compound, where X and Y are transition metals and Z is not, is called a half-Heusler compound, after Heusler who discovered that alloys of the form X_2YZ, called (full) Heusler alloys after him, are ferromagnetic, even when some of the composites are non-ferromagnetic. As we will explain below, full Heusler alloys are predicted to be half-metallic. Among various oxides and alloys that are expected to be half metallic, full Heusler alloys are especially stable against disorder, with a high Curie temperature and high magnetization (lower than Half Heusler alloys). Half Heusler alloys (XYZ) crystallize in a $C1_b$ structure with two interpenetrating FCC sublattices with a void on one of the sites. In half Heusler alloys, the minority band gap at E_F occurs as a consequence of hybridization between the X and Y transition metals. However in a full Heusler alloy, the Y transition metal does not serve to create the band gap for minority electrons at E_F. The gap occurs as a consequence of self hybridization of the X transition metal atoms, which is predicted to be much stronger than the XY hybridization. Hence full Heusler alloys are expected to be more stable. However the stability and strength of a full Heusler alloy gap is subtle and depends on the alloy

under consideration.

In 2006, Inomata et al[101] published studies on Magnetic Tunnel Junctions.with (001) ordered $Co_2Fe(AlSi)_{0.5}$ = CFAS Heusler alloys as the ferromagnets separated by the tunneling barrier. The CFAS alloys were sputtered at room temperature and then converted into epitaxial form by post-deposition annealing at 500^oC. In 2010, Nakatani et al[102] studied the bulk and interfacial scattering properties of CFAS via CPP-MR measurements of CFAS-based multilayers also sputtered at room temperature and then annealed at 500^oC. Their samples were in the form of pseudo spin valve nanopillars with a CFAS/Ag/CFAS structure on a MgO substrate with Cr/Ag underlayers . They reported GMR signals a large as $\sim 80\%$ at 14K and 34% at 290K. Both Inomata and Nakatani found larger MRs when the CFAS layers had the B2 structure in which F and the AS atoms are disordered than when they had the $L2_1$ structure without disorder.

We decided to extend these studies to epitaxial grown CPP micropillar structures with superconducting Nb leads for two reasons: (a) to eliminate the finite lead resistances that Nakatani et al[102] had to compensate for in their samples, and (b) in hopes that epitaxial growth would give better CFAS then standard sputtering plus high temperature annealing.

In the rest of this chapter, we first discuss in more detail the structure of a half metallic full Heusler alloy of the form X_2YZ and the origin of its half metallicity and magnetism. We then discuss our attempts to grow epitaxial CFAS and optimizing the methods using different spacer and under layers to the spin valve structure, to obtain the highest $A\Delta R$.

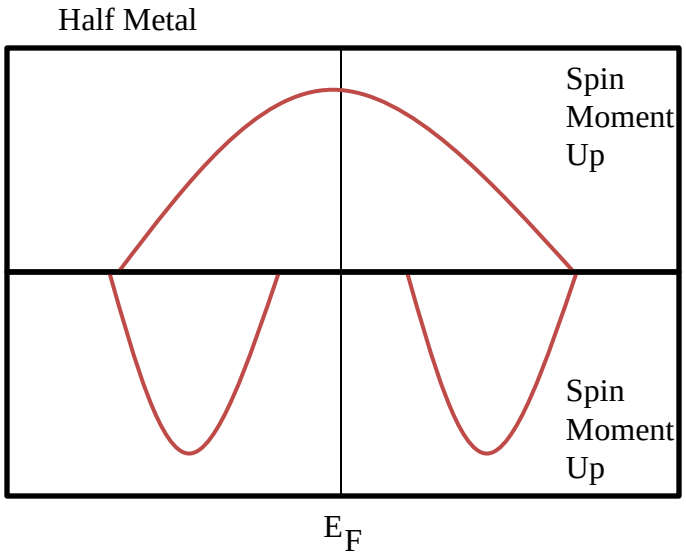

Figure 6.1: Schematic of a half metal at E_F [After [99]]

6.2 Half metallic Full Heusler Alloys

A full Heusler alloy of the form X_2YZ has a crystal structure best described as four interpenetrating FCC sublattices, or the $L2_1$ crystal structure (Figure 6.2a). Using first principle calculations, deGroot [100] has shown that $L2_1$ ordered full Heusler alloys are half metallic. From Figure 6.2a, the atomic positions are X(0,0,0), Y(1/4,1/4,1/4), X(1/2,1/2,1/2) and Z(3/4,/3/4,3/4). A fully ordered $L2_1$ crystal growing with its (100) (hkl) planes parallel to the surface of the film has a non zero structure factor for h,k and l all odd. Figure 6.2b shows a disordered state known as B2 where the body centered atom has disorder between Y and Z. Non-zero structure factors of a B2 fully-disordered state have all the h, k, l even. B2 fully disordered CFAS crystal structures have been shown to be half metallic by TMR experiments by Tezuka et al[101]. This experimental observation is supported by density of states calculations by Kota et al[103] for $L2_1$ ordered and B2 fully disordered crystal structures of

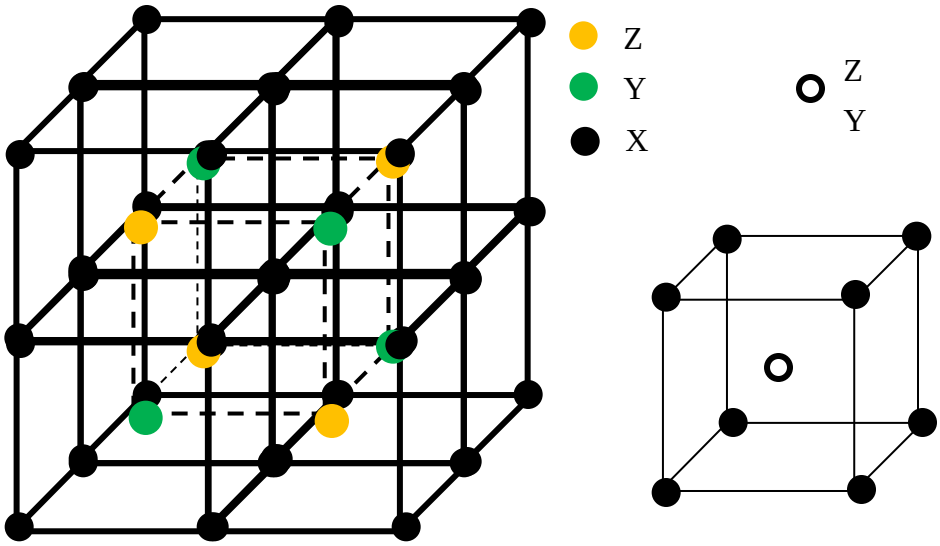

Figure 6.2: X_2YZ crystal structure. (a) $L2_1$ structure: The atomic positions are X(0,0,0), Y(1/4,1/4,1/4), X(1/2,1/2,1/2) and Z(3/4,/3/4,3/4). Structure factors are all odd. (b) B2 disordered structure is when the body centered atom within a single cube is either Y or Z atom. Structure factors are all even. [After [99]]

CFAS. There is another kind of disorder that can occur in the $L2_1$ structure between all the atomic constituents in the X_2YZ full Heusler alloys. Such a disorder is called A2 disorder. Density of states calculations of A2 disordered crystal structures of full Heusler alloys, by Kota et al[103], show that half metallicity is destroyed in the alloys for such a disorder.

The origin of the half metallicity of a full Heusler alloy of the X_2YZ form was shown by first principle calculations by deGroot [99]. Calculations produced continuous density of states across the Fermi energy for the majority electrons and a gap, whose size depends on the hybridizations of the transition metal d bands, for the minority electrons. The

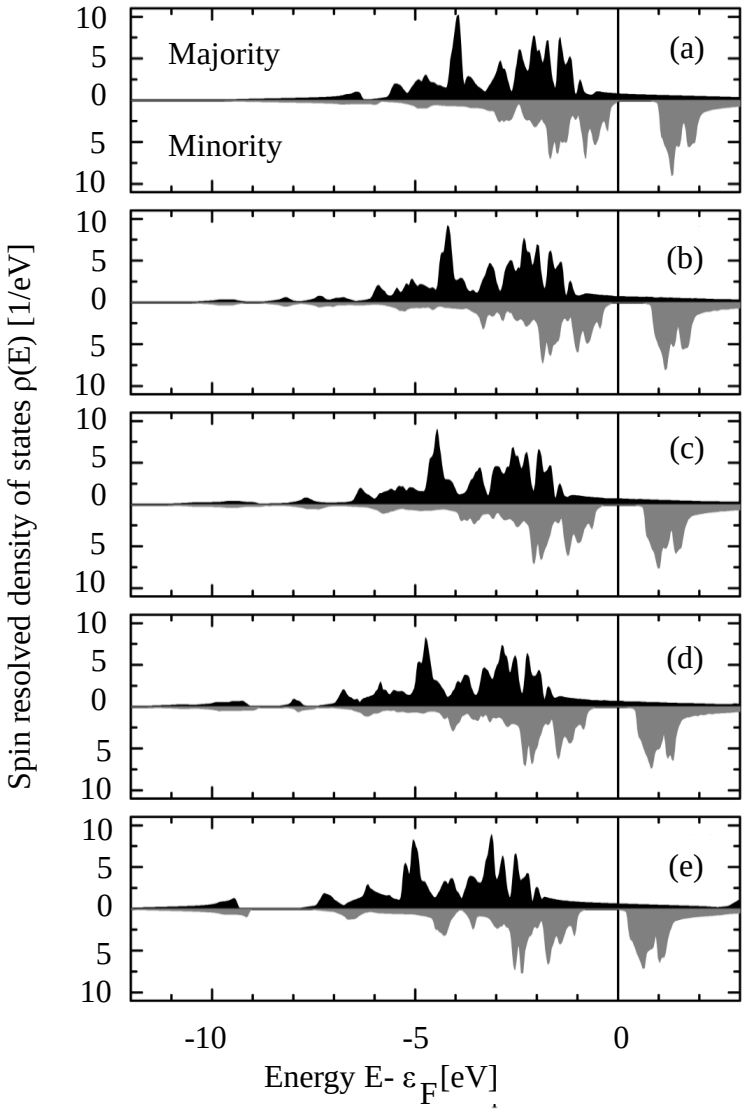

Figure 6.3: Local Density Approximation calculations with exchange correlation of Density of States for different compositions of quarternary CFAS alloy. Figures (a, ... , e) show the DOS with increasing amount of Si for x = 0, 0.25, 0.5, 0.75, and 1. Clearly with Si=0.5, in (c), the EF lies in the middle of the band gap making it the most stable. [104]

placement of the E_F in the minority band gap is tuned by the Z (main group element) electrons. Quarternary Huesler alloys, such as CFAS, where the Z atom position per unit cell is shared between two main group elements, Al and Si, provide more stability to its half metallic character by tuning the Fermi level to the middle of the gap by altering the number of valence electrons. Such tuning is shown in Figure 6.3 [104], where the position of the Fermi energy is compared over the range between the two full Huesler alloys Co_2FeAl and Co_2FeSi that bracket the quarternary Huesler alloy $Co_2FeAl_{0.5}Si_{0.5}$. In Co_2FeSi, E_F lies closer to the top of the minority gap, while in Co_2FeSi it lies closer to the bottom of the minority gap. Providing some support for this argument, as mentioned above, Tezuka et al[101] found that TMR obtained using CFAS crystallized in the B2 structure, a disordered structure between atoms Y and Z (in a quarternary Heusler alloy Z being either of the main group elements) atoms (Figure 6.2b) was much higher than the TMR obtained for the $L2_1$ structures Co_2FeAl and Co_2FeSi.

6.3 Overview of our Experiment

Our experiment is aimed at growing epitaxial CFAS using High Temperature sputtering and fabricating micrometer sized spin valve samples of CFAS(t)/N(25nm)/Py(24nm) where N=Ag or Cu. The motivation is to obtain values of spin diffusion length and bulk asymmetry parameters for CFAS and compare the results with those obtained by [102][105] and [106] from the University of Tsukuba. In this section we will do the following:

6.3.1 Predict a value for $A\Delta R$ for our sample structure using a simplified VF equation for

AΔR for spin valves of the form CFAS/Cu/Py with t$\gg \ell_{sf}$. The CPP MR parameters for Py for our CFAS/Cu/Py sample will be taken from our previous studies. Those for CFAS will be taken from [102][105] and [106]. Having done that, we will then extend the calculations to the sample structure CFAS(t)/Ag(5nm)/CFAS(t) in [102] to check whether the simple VF equation gives AΔR close to their measured values of AΔR .

6.3.2 Explain the steps taken towards achieving epitaxial growth of CFAS using Nb as the bottom electrodes of our CPP S samples.

6.3.3 Describe various sample structures with varying under layers and spacer layers to obtain a significant MR and AΔR as predicted in Section 6.3.1.

6.3.1 Checking our VF model

Earlier studies on bulk and interfacial properties of CFAS were done by Nakatani et al [102] [105][106] using pseudo spin valves of the form CFAS(t)/Ag(5nm)/CFAS(t). They grew their chips, of the form Cr(10nm)/Ag(100nm)/CFAS(t)/Ag(5nm)/CFAS(t)/Ag(5nm)/Ru(8nm), at room temperature. The Cr/Ag underlayers were first grown and annealed at 300^0C to improve the surface for further deposition of CFAS/Ag/CFAS which was then annealed at 500^0C in the presence of 5kOe field for 30 minutes. Pseudo spin valve samples were fabricated by patterning 0.07 X 0.14 μm^2 to 0.2 X 0.4 μm^2 sized elliptical pillars. The Ag acted as the electrodes with a finite resistance of $\sim$0.13Ω at 14K, their low temperature measurement. The two sputtered CFAS thicknesses are the same and the two CFAS layers were claimed to be antiferromagnetically coupled by magnetostatics. If so, it is not clear why the MR curve [102] of a sample t_{CFAS} = 2.5nm, does not show maximum resistance at zero applied field,

and why the measurement at 14K show asymmetric hysteresis curves for two CFAS layers with nominally the same thickness. Perhaps the structure of the two CFAS layers are not identical.

We chose our sample structure as a spin valve with F_1= CFAS and F_2=Py with a thick enough N layer (either Cu or Ag) to magnetically decouple them. The H_C (Coercive field) of Py =24nm($\sim$20 Oe), should be well below the H_C of all of the CFAS samples, even the thickest ($\sim$20nm), where sometimes H_c was as low as $\sim$80 Oe. The other advantages of using Py instead of a second layer of CFAS as the F_2, are that Py needn't be grown epitaxially and we know its parameters from our prior studies. The chosen thickness of Py (24nm) also removes any sample to sample variation and should maximize the value of $A\Delta R$.

We expect $A\Delta R$ for our CFAS/N/Py samples to be smaller than those of CFAS/N/CFAS samples because $\rho_{CFAS}\sim 7\rho_{Py}$.

We will use the values of bulk ${\ell_{sf}}^{CFAS}$,β, $\gamma_{CFAS/Ag}$ and ${AR^*}_{CFAS/Ag}$, determined by Nakatani and company, to estimate $A\Delta R$ for both our CFAS(t)/Cu(25nm)/Py(24nm) spin valve samples and the CFAS(t)/Ag(5nm)/CFAS(t) pseudo spin valve samples made by them. The parameters used for Py will be taken from our previous studies [26] and we will assume that the CFAS CPP MR parameters for the interface of CFAS/Ag, derived by Nakatani and company, are similar to the interfacial properties of CFAS and Cu.

Equation 2.5 represents $A\Delta R$ for the 2CSR model for two identical F layers. Generalizing it to the case with different F layers gives the following,

$$A\Delta R = 4\frac{(\gamma {AR^*}_{F_1/N} + \beta_{F_1}{\rho_{F_1}}^* t_{F_1})(\gamma {AR^*}_{F_2/N} + \beta_{F_2}{\rho_{F_2}}^* t_{F_2})}{(AR_{Nb/F_1} + {\rho_{F_1}}^* t_{F_1} + {AR_{F_1/N}}^* + {\rho_{F_2}}^* t_{F_2} + {AR_{F_2/N}}^* + \rho_N t_N + AR_{Nb/F_2})}. \tag{6.1}$$

The assumption in Equation 6.1 is that the thicknesses of the individual layers are smaller than the respective spin diffusion lengths. In the more general VF model, when $t_F \gg {\ell_{sf}}^F$ with $t_N \ll {\ell_{sf}}^N$, the numerator becomes a constant and the denominator represents the total AR for just the "active" part of the sample. The equation modifies as follows,

$$A\Delta R = 4\frac{(\gamma {AR^*}_{F_1/N} + \beta_{F_1}{\rho_{F_1}}^* {\ell_{sf}}^{F_1})(\gamma {AR^*}_{F_2/N} + \beta_{F_2}{\rho_{F_2}}^* {\ell_{sf}}^{F_2})}{({\rho_{F_1}}^* {\ell_{sf}}^{F_1} + {AR_{F_1/N}}^* + {\rho_{F_2}}^* {\ell_{sf}}^{F_2} + {AR_{F_2/N}}^* + \rho_N t_N)} \tag{6.2}$$

The CPP MR parameter values used for the calculations are:

${\ell_{sf}}^{CFAS}$=3nm [102], β_{CFAS}=0.86 [106], ${\rho^*}_{CFAS}$=2700nΩm, $\gamma_{CFAS/Ag}$=$\gamma_{CFAS/Cu}$=0.93 and ${\rm AR^*}_{CFAS/Ag}$ =${\rm AR^*}_{CFAS/Cu}$=0.62fΩm^2. The interfacial values are from [105]. The corresponding values for Py are ${\ell_{sf}}^{Py}$=5.5nm , β_{Py}=0.76, ${\rho^*}_{Py}$=290nΩm [33], $\gamma_{Py/Cu}$=0.77 and ${\rm AR^*}_{Py/Cu}$=0.5fΩm^2 [26]

1)For our CFAS(t)/Cu(25nm/Py(24nm) sample with t_{CFAS}=8nm, we obtain a value of ${\rm A\Delta R}_{Pred.} \sim 4.5$ fΩm^2.

We will compare this value with our measurements in Section 6.9.

2)For Nakatani's sample structure, CFAS(t)/Ag(5nm)/CFAS(t), we obtain a value of

Using the above values in Equation 6.2, we obtain a value of

$A\Delta R_{Pred.} \sim 15$ fΩm^2.

The experimental value of $A\Delta R_{Exp.}$ obtained by [102] for t_{CFAS}=8nm is $\sim$ 16fΩm^2. Hence the model works for Nakatani et al's results.

6.3.2 Overview of Experiments to obtain CFAS based Spin Valves

In section 6.5, we will describe the various different conditions of growth of CFAS that we attempted to obtain epitaxial growth of CFAS. The two most important requirements for epitaxial growth are

(a) High temperature growth conditions that allow ample mobility for depositing atoms to rearrange and nucleate on an underlying crystal structure.

(b)Having an under layer with similar crystal structure, and the surface layer of the underlying metal to have atoms separated by a length comparable to the lattice parameter of the growing layer in the desired orientation. That is, layers can grow epitaxially by rotating to align to matched atomic lengths of the surface atoms. For example the atoms along the [320] direction of Cu(100) are separated by l=5.7Å, which is comparable to the CFAS(100) lattice parameter, a=5.69 Å.

We chose MgO as the substrate, as MgO has a basic Cubic crystal structure which aids in the growth of epitaxial Nb of the desired orientation to hopefully lead to epitaxial CFAS with the desired orientation. However CFAS itself has an FCC structure while Nb has a BCC structure. Hence we first decided to buffer the difference in CFAS and Nb crystal structures by growing a Cu layer in between, since Cu grows in an FCC structure. The first spin valves we made used Cu under CFAS, and for simplicity, Cu as the spacer layer between CFAS and

Py. Since the Nakatani group had determined Ag spacer layers between CFAS layers to be the most suitable to achieve low interface roughness, we later tried making spin valves with Ag spacer layers. The best results with both Cu and Ag spacers were nominally the same.

For the next step, we tried growing CFAS epitaxial layers with Ag as the underlayer. Films made with Ag as the underlayer to CFAS didn't give desirable B2 epitaxy of CFAS. Hence we next tried to grow epitaxial CFAS films directly on Nb. Such films seemed to be growing with B2 epitaxy, and spin valves made from such samples with both Cu or Ag spacer layers gave similar best values of $A\Delta R$. Finally we also tried growing CFAS with Nb/Cu/Ag underlayers to facilitate good growing conditions with lower interface roughness. Such spin valves gave similar best case results as Nb/Cu/CFAS and Nb/CFAS samples.

6.4 Chemical Analysis

The stoichiometry of the components of the CFAS alloy plays an important role in determining its half metallicity. As discussed in [104], the Fermi level position is sensitive to the total number of valence electrons. We used Electron Dispersive Spectroscopy (EDS) (Section 3.3.5) to determine the composition of our CFAS target and the deposited films. An EDS analysis of our target purchased from Kurt J. Lesker is shown in Figure 6.3. The atomic weight percentages of Co, Fe, Al and Si are as expected for Co=2,Fe=1, Al=Si=0.5. In contrast, the composition of the deposited films showed consistently low Si and Fe composition (Table 6.1). To try to get films with better stoichometry, we purchased a second target (vacuum melted) with a higher Si composition (target stoichiometry of $Co_2FeAl_{0.5}Si_{0.6}$).

The EDS of the new target (Target2) and the samples made using the new target are

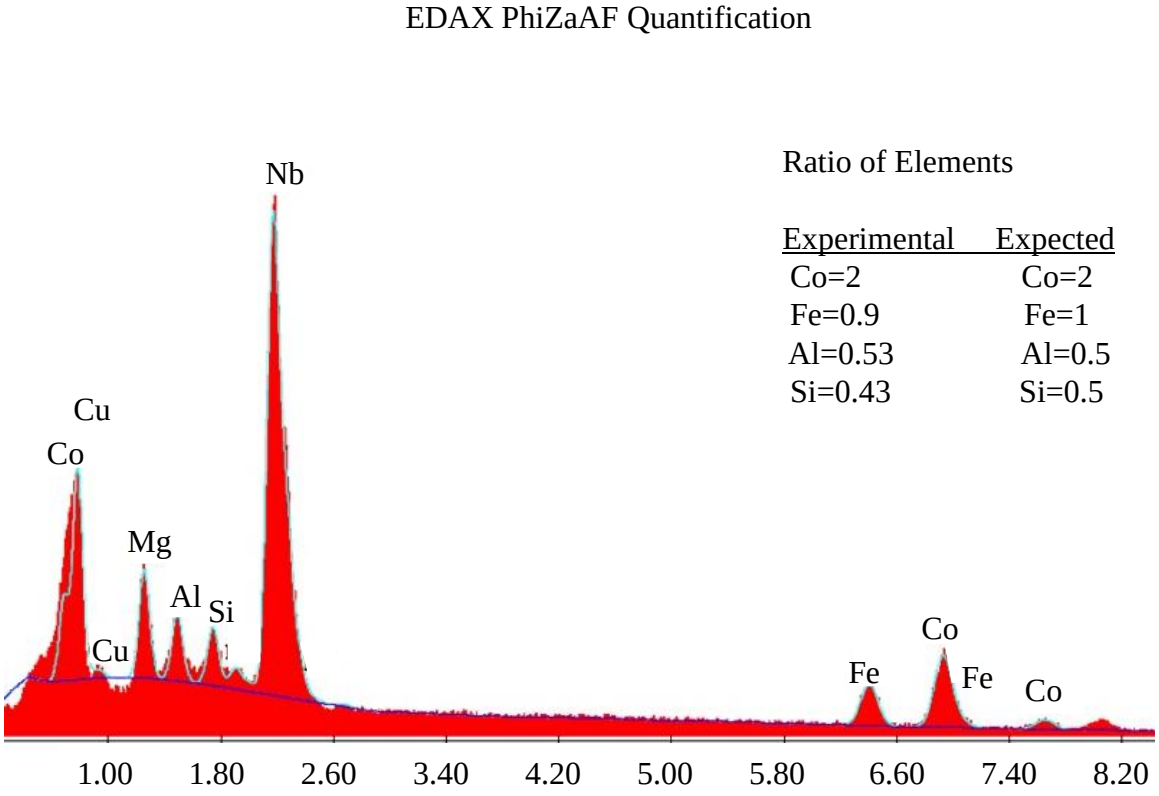

Figure 6.4: EDS measurement on Target1 with composition $Co_2Fe(Al\ Si)_{0.5}$

shown in Table 6.2. The Si ratio improved considerably in the samples made with the new target, but the Fe composition was still low. However for maintaining half metallicity of the alloy, the correct Si and Al compositions are more crucial than the high valence transition metal, as the s and p orbitals from the main group elements serve to provide the empty states for accommodating electrons from the transition metals [104].

Ratio of elements of CFAS constituted in films deposited using sputtering				
Sample	Co	Fe	Al	Si
1969-8	2.00	0.90	0.51	0.44
1993-b-7	2.00	0.93	0.49	0.40
1993-b-8	2.00	0.92	0.62	0.50
1993-b-9	2.00	0.92	0.53	0.40
1992-7	2.00	0.88	0.44	0.39
2019-6b	2.00	0.0.90	0.44	0.36
1943-1	2.00	0.90	0.50	0.41
2019-6a	2.00	0.90	0.44	0.38

Table 6.1: EDS measurements on films deposited using Target1 and measured at 5kX Magnification in the Hitachi SEM.

6.5 Epitaxial growth of CFAS

From our discussion above, it is clear that the interaction of the X Y and Z atoms in a Full Heusler alloy plays a crucial role in determining its half metallicity. Hence the ideal of growing CFAS films epitaxially follows naturally from that discussion. We attempt to grow epitaxial CFAS films in the (100) orientation where the CFAS (100) crystal plane is parallel to the substrate. The lattice parameter of CFAS is 5.69Å obtained using Vegard's rule. As mentioned before, an $L2_1$ structure is identified by the observation of all odd *hkl* peaks in the X Ray diffraction (XRD) patterns of epitaxially deposited films. In contrast, a B2 structure is identified by the observation of all even *hkl* peaks in the XRD patterns of epitaxially deposited films. Hence the presence of (200) or (400) peaks indicate mostly B2 crystal structure. In the following section, we will show the steps we took to achieve epitaxial growth of CFAS. We were unable to perform quantitative analysis to determine how much of the volume of our samples are actually single crystal. However we are able to claim that any single crystal volume in our epitaxially grown films has a B2 ordered crystal structure.

Ratio of elements of CFAS constituted in films deposited using sputtering				
Sample	Co	Fe	Al	Si
Target2	2.00	0.98	0.49	0.47
2049-3	2.00	0.85	0.54	0.51
2049-2	2.00	0.82	0.47	0.54

Table 6.2: EDS measurement of Target2 showing close to the stoichiometric atomic composition of CFAS. The two films of CFAS 100nm each were measured to show considerably higher Si composition. The Fe composition is still low.

The method of growing epitaxial layers of metals using High Temperature sputtering is described in Section 3.2.2. Our need for multilayers sandwiched between superconducting leads to provide uniform current required us to use Nb as our bottom electrode. Hence we aimed to find the best possible growing condition of CFAS with a base layer of Nb. We had to first find a substrate on which to grow the desired epitaxial (001) Nb. The substrate was required to have a cubic structure to aid in the epitaxial growth of layers on top of it. MgO has a Halite structure (cubic) with a lattice parameter of 4.13Å. As a check we also grew some films on a Sapphire substrate which was shown previously [82] to make Nb grow in the (110) orientation. We obtained Nb(001) XRD peaks for films grown on MgO, but not on Sapphire. We, thus, limited ourselves to MgO, on which we found, from x-rays, that we could grow sequentially (001) Nb (best growth T = 650^0C)), (001) Cu (best growth T $\sim$ 200^0C) and B2 ordered (200) CFAS (best growth temperature = 500^0C). The next few subsections will describe attempts to optimize the growth conditions to give the best possible epitaxy of CFAS in the (200) crystal growth orientation.

6.5.1 Nb/Cu/CFAS on MgO

We started our tests for the conditions of epitaxial growth of CFAS on MgO substrates with Nb and Cu underlayers. Nb is used as an electrode for low temperature measurements as discussed in the beginning of this section. Nb has a BCC structure while CFAS is essentially an FCC structure. To use as a buffer growing layer with an FCC structure, we chose Cu with a lattice parameter of 3.61Å. As discussed before, CFAS can grow epitaxially if the length between any two surface atoms of the Cu layer is close to the lattice parameter of CFAS. The CFAS then grows in the (100) orientation and is simply rotated with respect to the epitaxial Cu planes.

Figure 6.5 shows X Ray evidence of B2 ordered CFAS films made with MgO substrates and Nb and Cu underlayers using the basic high temperature sputtering process described in Section 3.2.2. In Figure 6.5, we also show X Ray spectra of CFAS layers grown at different temperatures. We find that the presence of (400) and (200) peaks for CFAS grown at LT=17V (See Table 3.2) indicates that the CFAS grows in a B2 crystal structure. The presence of (200) Cu and (100) Nb (grown at HT=23V) peaks for those films indicate that the underlayers grow with a (100) orientation as well. The next section will describe the results of AΔR results obtained from devices made using this epitaxial growth recipe. The lattice structure and parameters of the substrate and the underlayers are:

1) MgO= 4.13Å with a Halite Crystal structure.

2) Nb= 3.3Åwith a BCC structure.

3) Cu=3.61Å with an FCC structure.

4) CFAS=5.69Å with a B2 structure.

The XRD pattern showing (100) peaks for each individual layer can be best described as the following interplanar growth relations MgO(100)[110]||Nb(100)[100], Nb(100)[100]|| Cu(100)[100], Cu(100)[320]||CFAS(100)[100].

With this recipe to grow epitaxial B2 disordered CFAS, we made CPP MR spin valve samples (Section 6.7) and obtained a maximum AΔR $\sim$ 1.6 fΩm^2, for thick layers (t$_{CFAS}$ >8nm). This maximum AΔR is about 35% of what we predicted in Section 6.3.1. Some of the samples gave much lower AΔR $\sim$ 0.1-0.5 fΩm^2. Hence we attempted to try to grow epitaxial CFAS using different underlayers and temperatures to obtain a higher AΔR .

6.5.2 Nb/Ag/CFAS on MgO

To try to increase AΔR over the results obtained with Cu on Nb, we tried to grow CFAS with an underlayer of Ag, which [102] found to be better than Cu for minimizing interface roughness. The XRD plots for Ag grown straight on Nb are shown in Figure 6.6. Unfortunately, Ag grows on Nb in a (220) orientation. The growth can be described as Nb(100)[[110]||Ag(110)[100]. The Ag(110) plane has one edge of length 5.78 Å, along the face diagonal of the FCC Ag lattice,and the other edge along the lattice parameter 4.09Å. The side with the lattice parameter 4.09Å aligns with the face diagonal of Nb (lattice parameter 3.3Å). The lattice mismatch between Ag and Nb is $\sim$14%. A lattice mismatch of $\sim$14% could be significant in causing strain between the layers which propagates through the layers. We then grew CFAS on the Ag. XRD spectra of Ag/CFAS grown on Nb are shown in Figure 6.7. Figure 6.7 shows that growing conditions of Nb(150nm) at 23V for the High temperature heater, Ag(100nm) at 14V for the Low Temperature heater, and CFAS at 17V

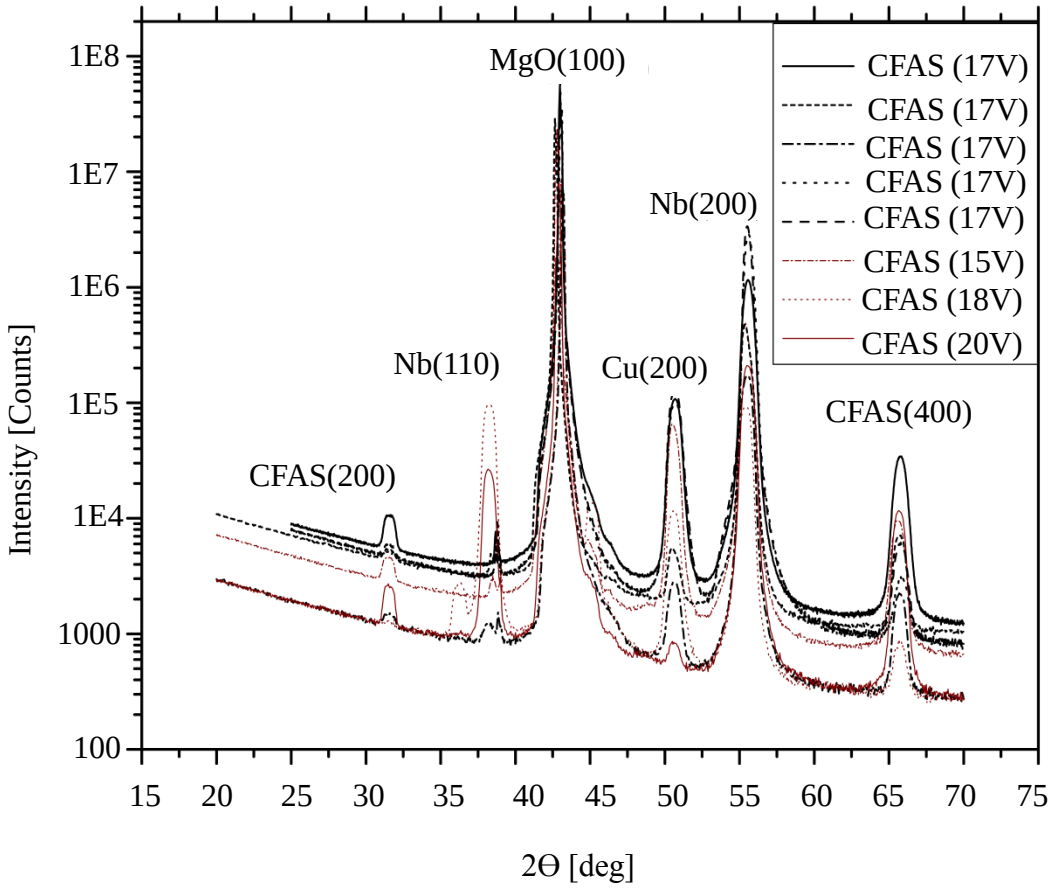

Figure 6.5: Various attempts at growing CFAS on Nb/Cu at different temperatures calibrated with the Low T heater power supply. 15V heats the heater to $\sim 450^0$C, 17V heats the heater to $\sim 500^0$C, 18V heats the heater to $\sim 600^0$C and 20V to $\sim 700^0$C. As is evident from the various plots, the ones where CFAS was grown at 17V gave the highest intensity (400) and (200) CFAS peaks.

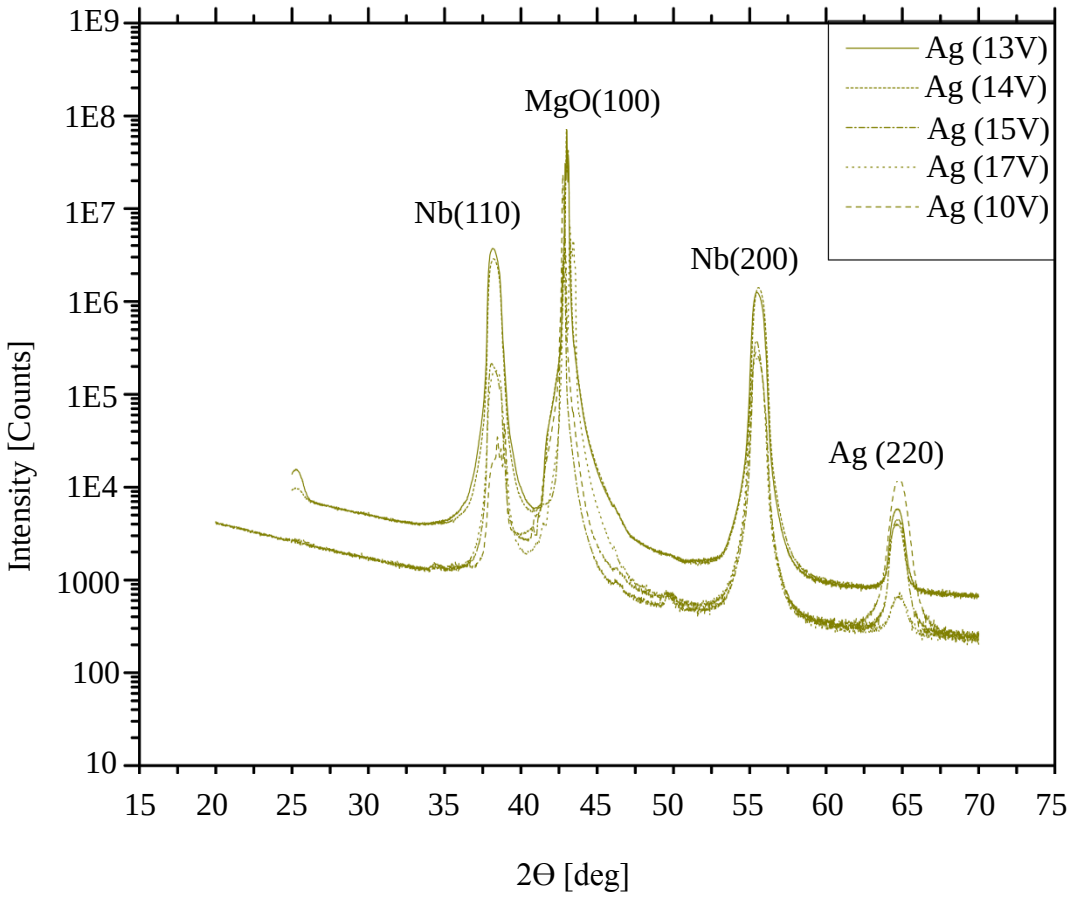

Figure 6.6: Nb/Ag showing Ag growing in the (110) orientation.

for the Low Temperature heater, gave the best possible conditions for B2 disordered CFAS. The orientation is best described as Ag(110)[111]||CFAS(100)[100] with the plane side of Ag with length 5.78Å aligned with the lattice parameter of 5.69Å for CFAS.

6.5.3 Nb/CFAS on MgO

Next, we tried to grow CFAS directly on Nb with the growing conditions similar to those above −i.e., Nb grown at 23V High T heater and CFAS at 17V Low T heater. The resulting

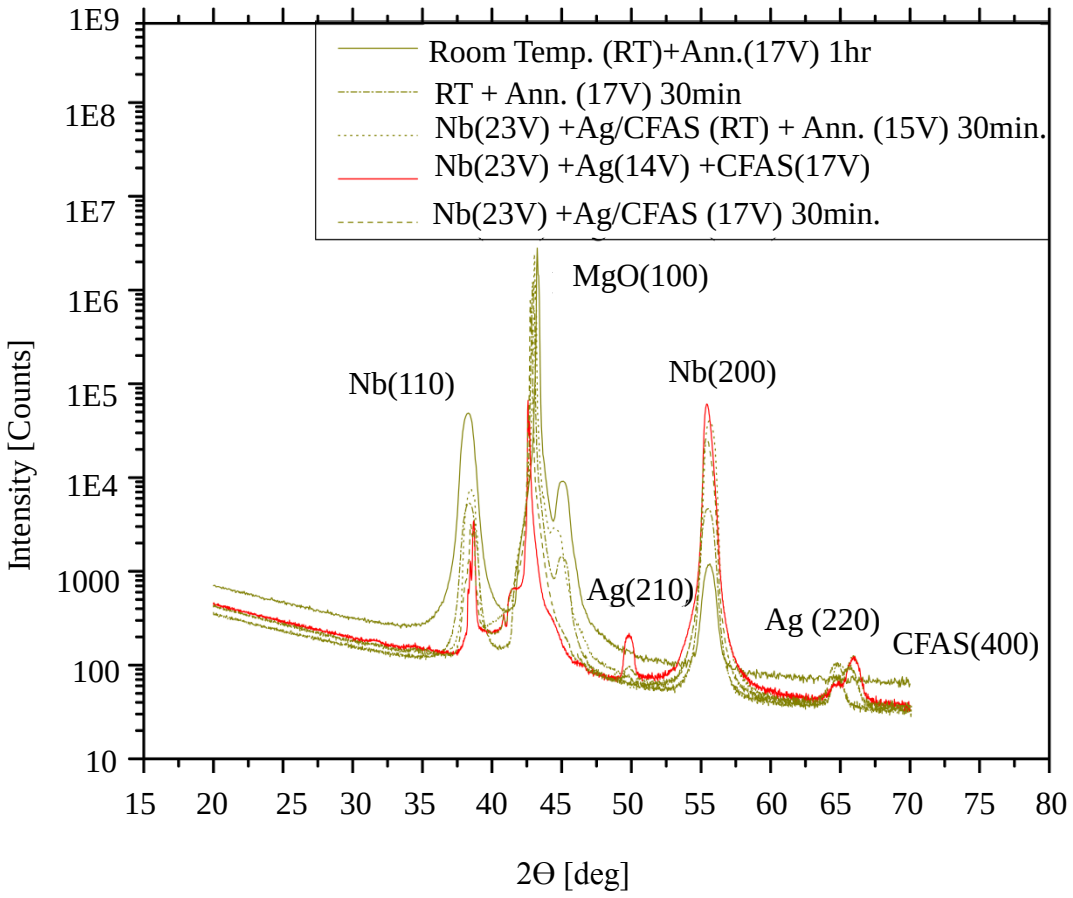

Figure 6.7: Nb/Ag/CFAS. The plot in red is when Nb was grown at 23V, Ag at 14V and CFAS at 17V, giving the largest intensity of the (400) CFAS peaks of them all.

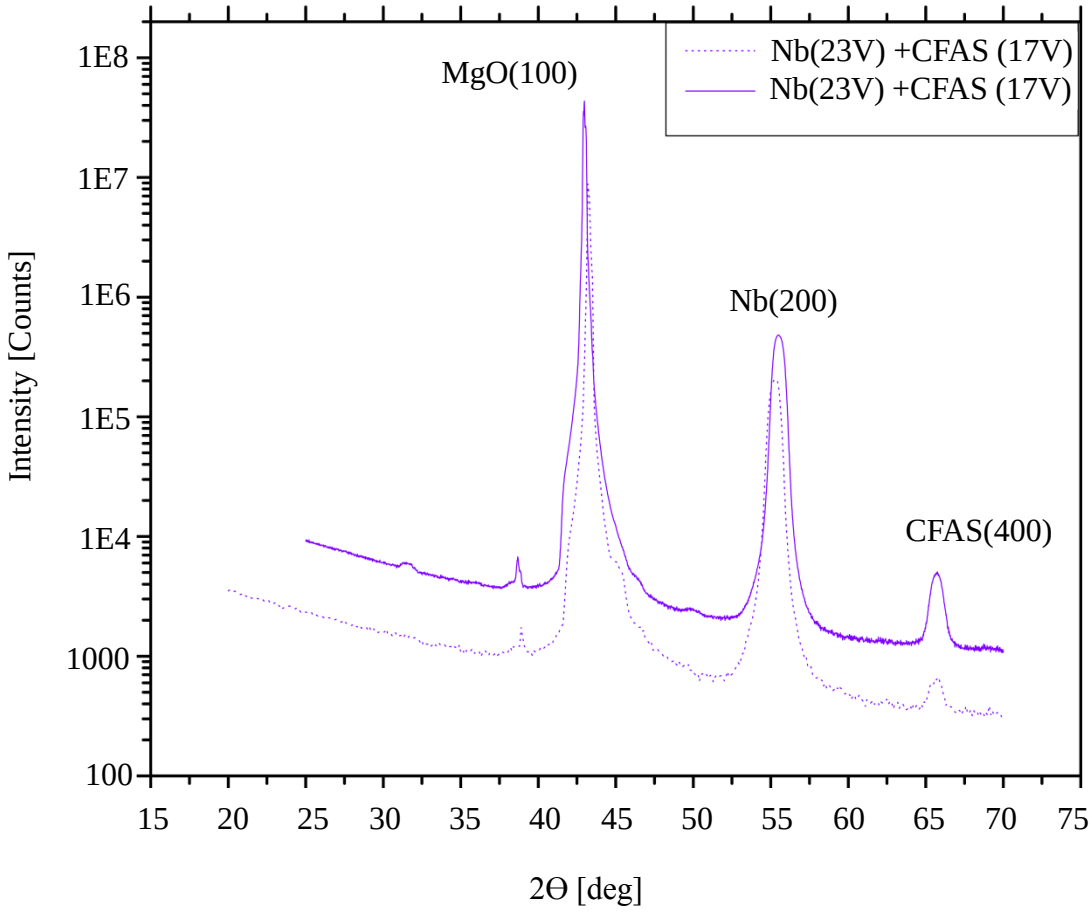

Figure 6.8: Nb/CFAS showing (400) CFAS peaks.

X-Ray diffraction plots are shown in Figure 6.8. Again, the CFAS grew in the B2 disordered state. The orientation can be described as Nb(100)[200]||CFAS(100)[100], with Nb(100)[200] of length 6.6Å aligned with CFAS(100)[100] of length 5.69Å, with a lattice mismatch of ∼14%.

6.5.4 Nb/Cu/Ag/CFAS on MgO

Lastly, because of the success that Nakatani[102] had with CFAS grown in Ag, we tried growing Nb/Cu and then Ag to overcome the ∼14% lattice mismatch that occurs between (110) Ag planes and (100) Nb. We grew Nb at 23V High T heater. After depositing the Nb, we waited 5 minutes before depositing Cu, and followed the Cu deposition by lowering the Low T heater onto the substrate and setting it at 14V. Ag was deposited after waiting for ∼10 minutes. The voltage on the Low T heater was then increased to 17V and maintained on top of the substrate for about 6 minutes before beginning to deposit CFAS. Figure 6.9 shows the X Ray spectra of CFAS grown with Nb/Cu/Ag underlayers. Ag grown on Cu should grow in the (110) orientation with much less strain as compared to Ag grown directly on Nb. The orientation of the layers could be described as Cu(100)[320]||Ag(110)[111] with the lattice mismatch between the [320] Cu edge (5.7Å) and [111] Ag edge (5.78Å) now being only ∼1.4% and hence causing significantly less strain as compared to Nb/Ag layers.

6.6 Magnetization Measurements

In the X_2YZ full Heusler alloy structure, the Z main group atom has low energy s and p orbitals that lie well below the Fermi energy. Therefore including the hybridized states and the s and p orbitals, there are 12 occupied states below the Fermi energy (1 from s, 3 from p and 8 from hybridized d orbitals). There are 7 unoccupied d states above the Fermi energy. Hence there can be a total number of 12 minority states occupied per unit cell below the Fermi energy. In a unit cell with total N number of valence electrons, the remaining states occupy the N-12 majority electrons. The magnetization per unit cell is then given as the

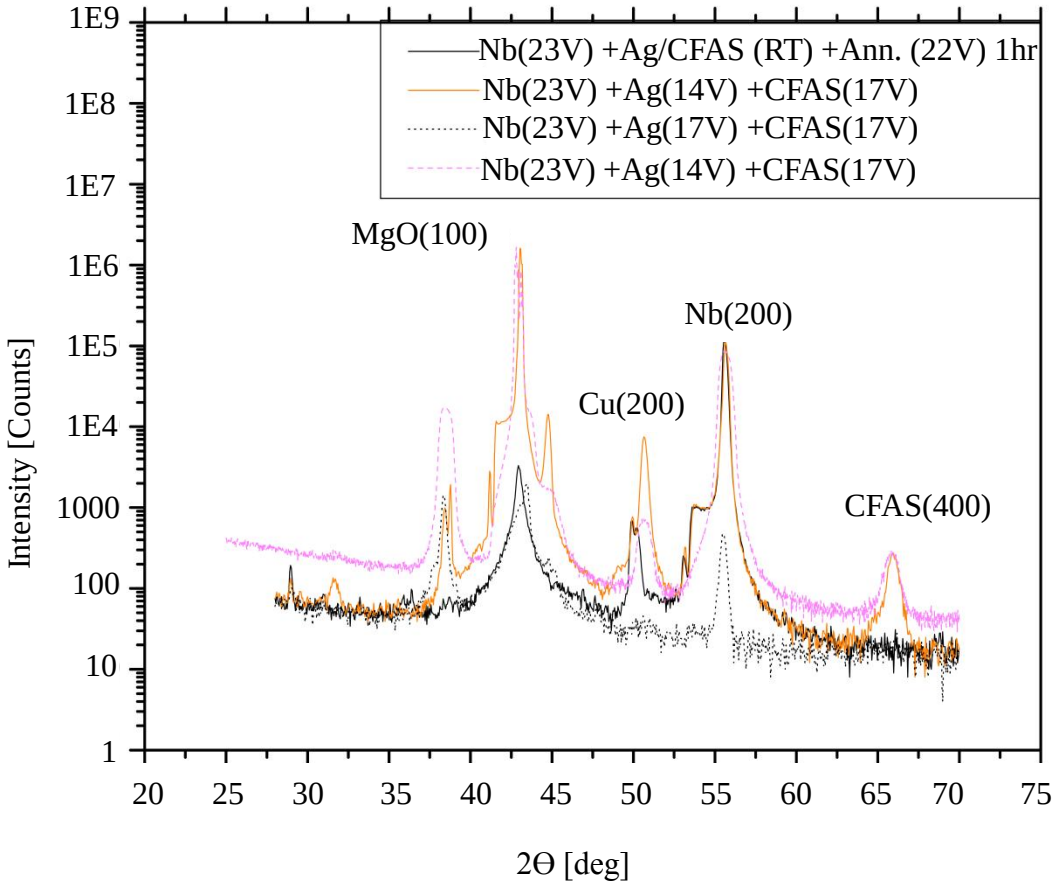

Figure 6.9: CFAS films grown with Nb,Cu, and Ag underlayers at different conditions. The best (200) and (400) peaks were observed for Ag grown at 14V and CFAS at 17V

number of unpaired electrons times the Bohr magneton μB. With the number of majority electrons being N-12, and number of minority electrons being 12, the magnetization M= ((N-12)-12) μ_B gives M = (N-24) μ_B . This is the famous Slater Pauling relationship of Magnetization M with respect to the valence electrons for full Huesler alloys. The saturation magnetization of Co_2FeSi is expected to be 6 μ_B using the Slater Pauling behavior. The partial substitution of Si with Al is expected to make the magnetization deviate from the Slater Pauling behavior giving the largest expected saturation magnetization to be about 5.5μ_B per unit cell [104]. From the magnetization measurements on our films prepared using the growth processes described in Section 6.5, we obtained the largest in-plane saturation magnetization of 5.0μ_B/cell for films grown with the Nb/Cu/Ag/CFAS structure, 4.0μ_B/cell for films grown with Nb/Cu/CFAS and 4.5μ_B/cell for the Nb/CFAS structure. For films grown with the Nb/Ag/CFAS structure, the saturation magnetization was about 3.7μ_B/cell. Figure 6.10 shows the magnetization curves for films made with the different recipes described above. The coercivity of the films varies due to differences in their thickness. Presumably the different saturation magnetizations indicate differences in the quality of the CFAS layers.

6.7 CPP MR using CFAS based spin valves

With the information on how to grow epitaxial CFAS with the various underlayers listed in Section 6.5, we are now ready to describe the spin valve samples using CFAS as an F layer. The procedure of making the micrometer sized samples to obtain the spin valve device sandwiched between two Nb electrodes is described in Section 3.2.2. In this section we

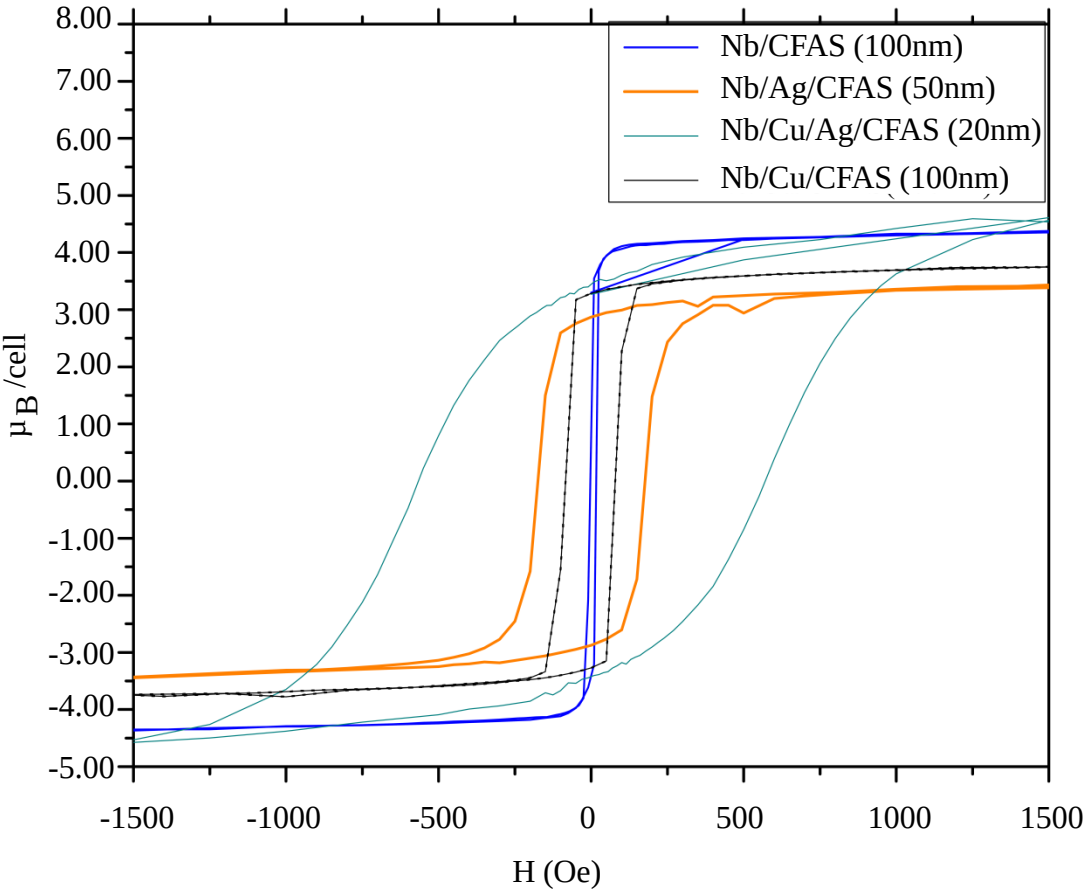

Figure 6.10: Magnetization curves of films made with different recipes.

describe the CPP Magnetoresistance of the various sample layer structures we implemented to try to obtain the highest possible AΔR .

6.7.1 With Nb/Cu as underlayer

With the best growing condition for CFAS in the B2 disordered state known for Nb and Cu underlayers, we made our hybrid spin valve samples with the following structure:
[Nb(150nm)/Cu(10nm)/CFAS(t_{CFAS})]$_i$/[Cu(25nm)/Py(24nm)/
Cu(10nm)/Nb(25nm)/Au(15nm)]$_j$/ [Nb(150nm)/Au(5nm)]$_k$

The square brackets with subscripts i,j and k represent the three stages of sputtering as described in the next paragraph. Py has switching fields varying from of 20-50 Oe whereas the switching field of CFAS varies from $\sim$ 80-400 Oe.

The first bracket, [..]$_i$, represents the high temperature growth of epitaxial Nb, Cu and CFAS layers. At the end of the epitaxial growth the substrate temperature is about 500^0C at which the last CFAS layer is grown epitaxially. If the layers in the second [..]$_j$ are grown directly on top of the hot substrate, the spacer Cu is most likely to diffuse through the CFAS and thereby to cause magnetic coupling between the CFAS and the Py layers. The hysteresis curve of two magnetically decoupled F layers should have steps indicating the different coercive fields of each F layer component. Early on, all the spin valves fabricated with the spacer Cu layer grown directly on top of the hot substrate showed no MR. We measured the magnetization of one such chip (CFAS/Cu/Py) and obtained the result shown in Figure 6.11. The absence of steps indicates the probability of magnetic coupling between CFAS and Py. To address this issue, we waited for about 5 hours to deposit the next set of

layers in the second $[..]_j$. The change in the process led to samples that gave an MR signal, which implies that the F layers are magnetically decoupled. Magnetization measurements on two chips with samples that gave an MR are shown in Appendix B, along with related AR data. These magnetizaions show the expected steps for Py and CFAS, but with an unexpected transition region which will be discussed in Appendix B. The third bracket $[..]_k$ represents the top electrode for the samples.

We also tried waiting for a period of about 1 hr between the CFAS deposition and the spacer layer deposition to reduce the amount of contaminants between the CFAS and the spacer Cu layer. The substrate plate temperature at the end of an hour read $\sim 60^0$C. $A\Delta R$ signals in such samples were not very different from the ones where we waited for $\sim$5hrs. The chamber was kept cooled with liquid N_2 to keep the pressure low and the chamber devoid of water vapor. The subsequent layers were grown,after waiting for $\sim$ 5 hrs, when the substrate plate temperature read $\sim 10^0$C. The chip was processed as described in Section 3.2.2. In the beginning the chips were being milled till the middle of the Cu spacer layer. Subsequently the process was altered to mill only through about 4nm of Py, as that was enough to define the area in the specific resistance AR. The sample diameter is about 50μm and the maximum thickness of all the layers combined is about 80nm, three orders of magnitude smaller than the width. The superconducting Nb leads ensure uniform current and the sample thickness $\ll$ width ensures that the fringing of current towards the edges is minimal.

Most of the samples made with the CFAS/Cu/Py structure gave an $A\Delta R$ in the range of 0.1-1fΩm^2 with a maximum $A\Delta R$ of about 1.6fΩm^2 for t_{CFAS}=8nm, less than the expected $A\Delta R$ =4.5fΩm^2 for the same thickness. The reason for the variation is not known but we

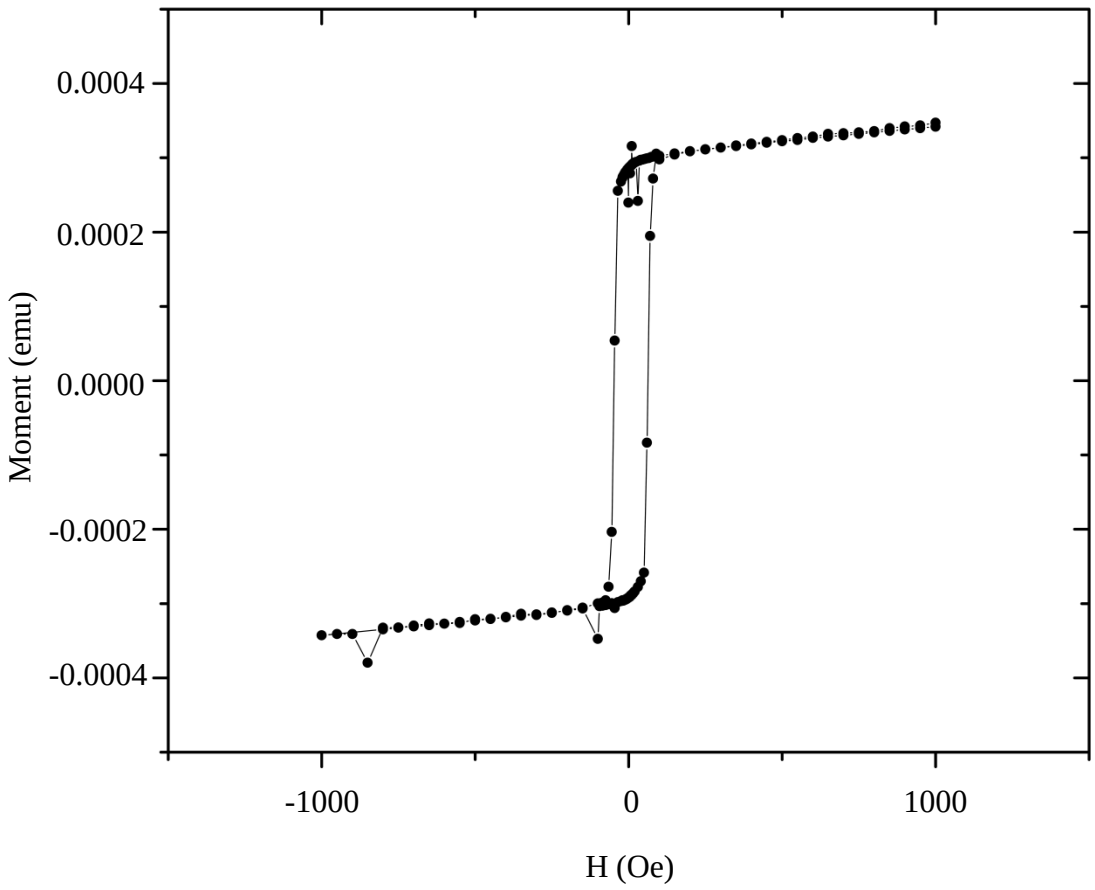

Figure 6.11: Hysteresis curve of a chip grown with Cu spacer grown directly on top of hot CFAS. The magnetization curve of two magnetically decoupled F layers should show a step in the hysteresis corresponding to the saturation magnetizations of the two F layers. The lack step in the curve indicates magnetic coupling between the F layers.

speculate that given our inability to quantitatively determine the fraction of oriented single crystal CFAS in our samples, it likely varies from sample to sample. It is also possible that the apparent AP state in some of our samples is only a lower bound to an actual AP state. See Appendix B for further description. As can be seen in Figure 6.12b, some samples show a rising shoulder at higher fields. The epitaxial, probably single crystal, Nb may have a lower H_{C2} (Type II Superconducting Critical Field) due to lower defect content, which may lead to flux penetration resistance at high enough fields. Figure 6.12a and c also show that the AP state is quite sharp. A sharp AP state is an indication that it is not well defined. A well defined AP state should require some significant change in field to make the layer magnetizations align parallel to achieve the P state. The very quick, sharp change implies that we might only be seeing an intermediate state, and not the actual AP state. We also varied the sample structure to substitute the Cu as a spacer layer with 20nm of Ag. The best results obtained by both Cu and Ag spacer layers were similar.

6.7.2 With Nb as underlayer

With Nb as the underlayer, grown similarly as above at 650^0C (23V on High T heater) followed by CFAS at 500^0C (17V Low T heater), we had samples with Ag or Cu spacer layers between the CFAS and Py.

(a)[Nb(150nm)/CFAS(t_{CFAS})]$_i$/[Ag(20nm)/Py(24nm)/
Ag(10nm)/Nb(25nm)/Au(15nm)]$_j$/[Nb(150nm)/Au(5nm)]$_k$

(b)[Nb(150nm)/CFAS(t_{CFAS})]$_i$/[Cu(25nm)/Py(24nm)/
Cu(10nm)/Nb(25nm)/Au(15nm)]$_j$/[Nb(150nm)/Au(5nm)]$_k$

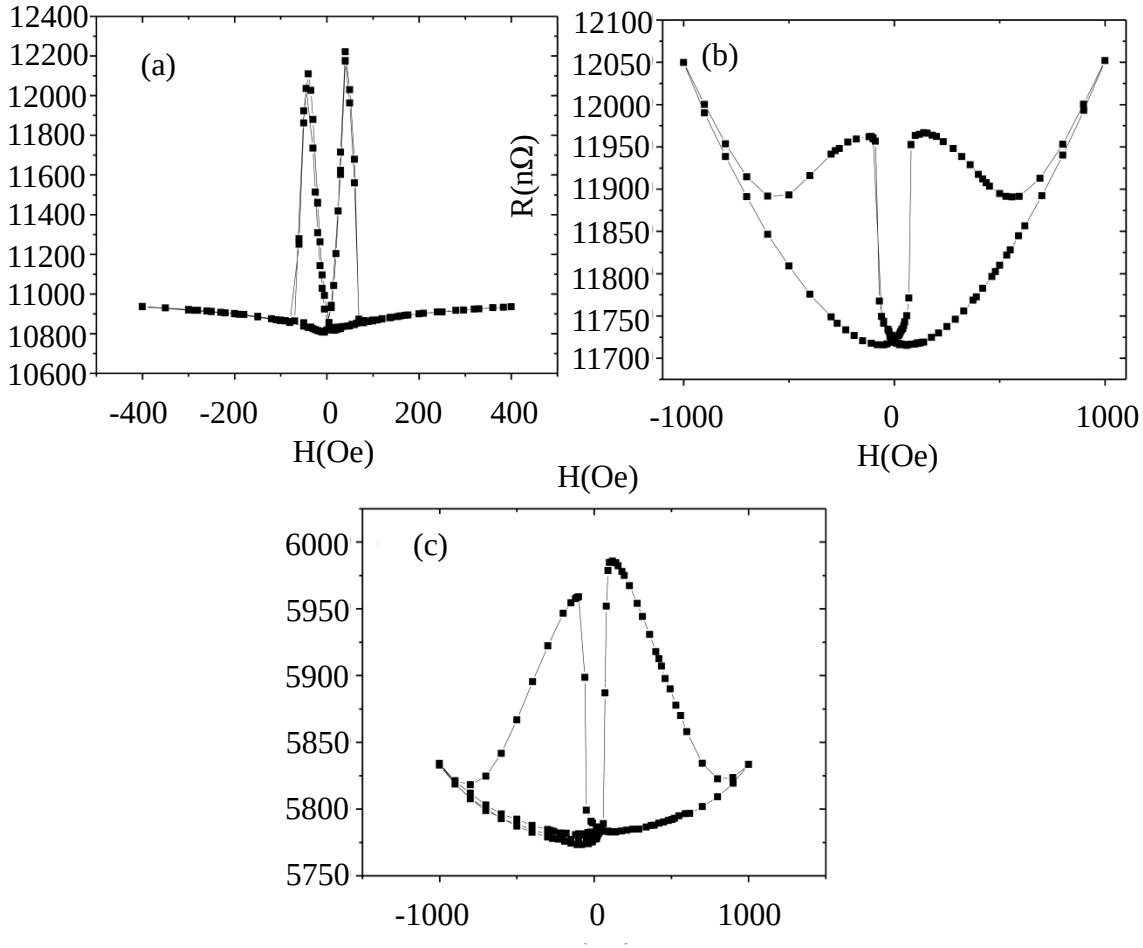

Figure 6.12: MR curves for samples grown with Nb and Cu underlayers for CFAS thickness from (a)15nm, (b)20nm to (c) 8nm. (a) and (c)show sharp AP states while (b) shows rising shoulders at high fields due to possible flux flow resistance in epitaxial Nb. The apparent AP state is probably a lower bound to the true AP state.

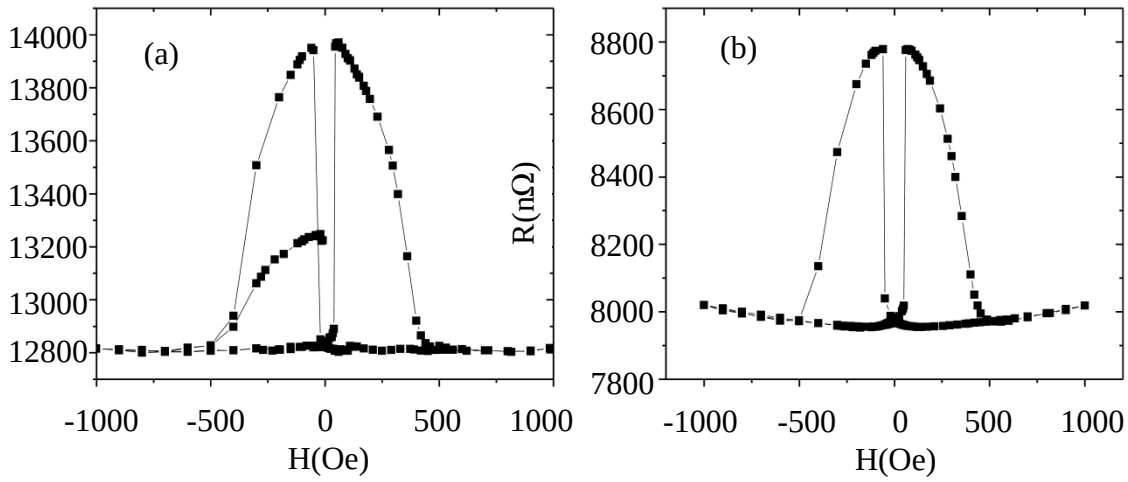

Figure 6.13: MR curves for samples grown with (a) Nb as underlayer and (b)Nb,Cu, and Ag as underlayers for CFAS thickness =20nm. (a) and (b)show sharp AP states. The apparent AP state is probably a lower bound to the true AP state.

The process of patterning was the same, involving patterning 50 μm pillars on the film strip and milling through 4nm of Py before depositing the top Nb(150nm)/Au(5nm) layers. Notice the lack of a well defined flat AP state, which again leads us to believe that what we see is a lower bound to the true AP state. Figure 6.13a shows an MR curve for Nb/CFAS(20nm). Again for t_{CFAS}=8nm, we obtained a maximum AΔR of $\sim$ 1.8fΩm^2, about 40% of the predicted 4.5fΩm^2, with several samples giving much smaller AΔR of $\sim$0.2-1 fΩm^2.

6.7.3 With Nb/Cu/Ag underlayer

In this sample structure, the Nb was grown at 650^{0}C (23V High T heater), Cu at $\sim$ 100^{0}C, Ag at 14V Low T heater, and CFAS at 17V Low T heater. The sample structure is

[Nb(150nm)/Cu(10nm)/Ag(10nm)/CFAS(t_{CFAS})]$_i$/[Ag(20nm)/Py(24nm)/
Ag(10nm)/Nb(25nm)/Au(15nm)]$_j$/ [Nb(150nm)/Au(5nm)]$_k$

Again the patterning process remained the same,but with a Ag spacer layer between the CFAS and the Py. Figure 6.13b shows an MR curve for Nb/Cu/Ag/CFAS(20nm)with a sharp AP state, probably a lower bound to the true AP state. The largest AΔR for t_{CFAS}=20nm is $\sim$1.7fΩm^2, whereas what we obtained in Section 6.3.1 for t_{CFAS}=8nm was $\sim$4.5fΩm^2. The predicted AΔR for t_{CFAS}=8nm should be the same as that for t_{CFAS}=20nm since both t_{CFAS} =8nm and 20nm are thicker than ${\ell_{sf}}^{FAS}$=3nm [102] and Equation 6.2 is the same for both. Therefore even with Nb/Cu/Ag underlayers, our highest AΔR is only about 40% of the predicted AΔR .

6.8 Sample structures that failed to give an MR signal

Aside from the samples described in Section 6.7, we also tried other structures in an attempt to get a larger AΔR . These attempts were unsuccessful. The different structures are listed below:

1) Nb/Cu/CFAS(t_1)/Cu/CFAS(t_2)

The inability to grow two epitaxial layers at high temperature at the cost of the quality of the spacer layer, caused such samples to not work.

2)Nb/Cu/CFAS(t)/Cu/Py(6nm)/FeMn(8nm)

We tried making EBSV samples with the Py layer pinned with an adjacent AF=FeMn layer. None of those samples gave any MR. It is possible that heating the chips while "pinning" the Py contaminates the samples.

3)CFAS(t)/N/CFAS(t) layers grown at room temperature followed by high temperature annealing.

It is possible that the annealing process for CFAS grown on Nb leads, doesn't lead to epitaxy. It is also possible that these chips got contaminated during the annealing process. The only samples that gave any MR with annealing were with a sample structure of Nb/Ag/CFAS/Ag/Py/Ag/Nb. However AΔR of these samples were much lower than our best results.

6.9 Analysis

Figure 6.14 shows average AR(AP), where the average is over the sample pillars on each chip, versus t_{CFAS} for samples made with the structure Nb/Cu/CFAS/Cu/Py/Cu/Nb. The slope of the graph should rise linearly with increasing thickness of CFAS, all other parameters remaining constant. The slope gives an estimate of the ρ_{CFAS} =720$\pm$200 nΩm, which is consistent with the ρ_{CFAS} obtained by Nakatani in [102] = 640nΩm. The other sample structures didn't have enough variations in CFAS thickness to obtain a reasonable slope to give us the CFAS resistivity. But, the cross and plus in Figure 6.14 show that averages of AR(AP)over pillars on a single chip, each of Nb/Cu/Ag/CFAS/Ag/Py and Nb/CFAS/Ag/Py, gave values consistent with the others in Figure 6.14.

With all the samples made with the various recipes listed above, the final graph of AΔR versus t_{CFAS} for all of the various sample structures is shown in Figure 6.15. Figures 6.16 and 6.17 show AΔR for just the two different sample structures, Nb/CFAS/Cu(or Ag)/Py and

Nb/Cu/CFAS/Cu/Py.

The $A\Delta R_{Pred.}$ for our sample structure of CFAS(8nm)/Cu(25nm)/Py(24nm) from the discussion in Section 6.3.1 was $A\Delta R_{Pred.}$=4.5 fΩm^2 for t_{CFAS}=8nm.

The best estimates of our experimental results were

1)$A\Delta R_{Best\,Exp.}$=1.6 fΩm^2 for the sample structure CFAS(8nm)/Cu(25nm)/Py(24nm) with Nb/Cu underlayers.

2)$A\Delta R_{Best\,Exp.}$ = 1.8 fΩm^2 for CFAS(8nm)/Ag(20nm)/Py(24nm) with Nb underlayer.

3)$A\Delta R_{Best\,Exp.}$ = 1.7 fΩm^2 for CFAS(20nm)/Ag(20nm)/Py(24nm) with Nb/Cu/Ag underlayers. For data of 2) and 3), see Appendix B.

Hence the experimental best estimates of $A\Delta R$ are about 40% of the $A\Delta R_{Pred.}$, indicating that the CPP MR parameters for our CFAS, are probably in the range of the ones obtained by Nakatani et al [102].

6.10 Summary and Future Work

We have been able to grow epitaxial B2 ordered CFAS, in the (100) orientation, using high temperature sputtering. The expected value of $A\Delta R \sim 4.5 f\Omega m^2$ from spin valves with t_{CFAS}=8nm of such epitaxially grown CFAS as F1 and t_{Py}=24nm as F2 in an F1/N/F2 is higher than our experimental best estimate of $A\Delta R \sim 1.8$ fΩm^2. There are large chip to chip fluctuations in our results, which leads us to speculate about the issues arising from our process:

1) Growing epitaxial CFAS on Nb as a superconducting lead is a constraint that probably doesn't allow us to grow the highest quality single crystal CFAS.

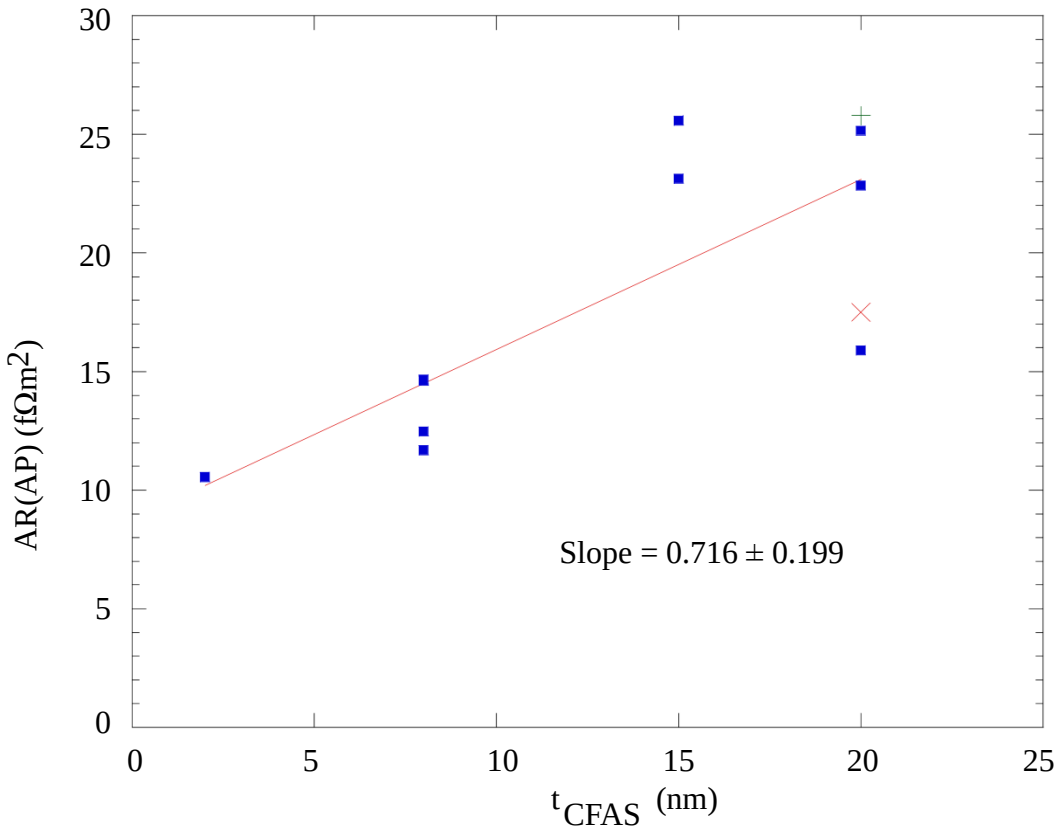

Figure 6.14: Average AR(AP), average of AR(AP) of samples on each chip, versus t_{CFAS} for just the samples with CFAS grown on Nb/Cu. The resistivity of CFAS obtained from the slope of the plot, for samples made with Nb and Cu as underlayers, is $\sim$ 720$\pm$200 nΩm. The 720$\pm$200 nΩm is consistent with that obtained by Nakatani et al (640nΩm)[102]. Red Cross symbol represents AR(AP) for CFAS grown on Nb/Cu/Ag (Chip 2066-2 in Appendix B) while green plus smbol represents AR(AP) for CFAS grown on Nb (Chip 2066-4 in Appendix B).

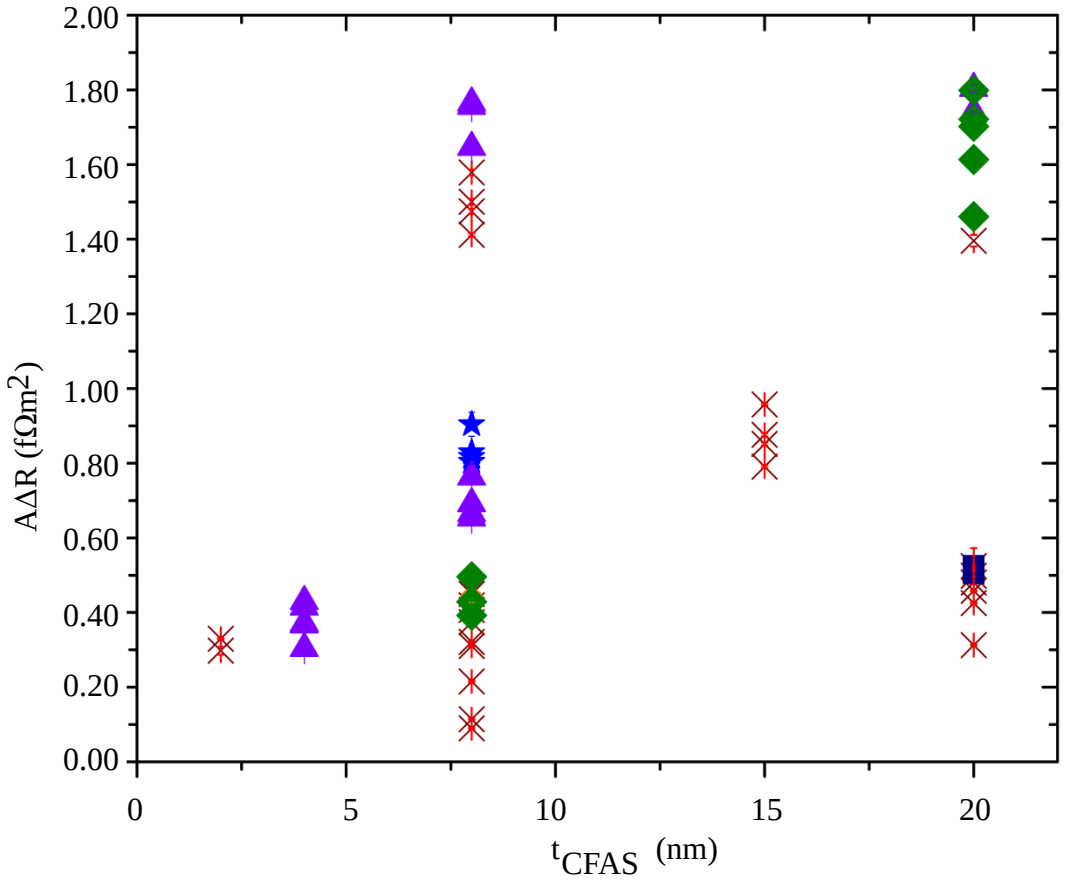

Figure 6.15: A plot of AΔR versus t_{CFAS} for the different sample structures. The different symbols are for the following structures;red cross for Nb and Cu as underlayers and Cu(25nm) as spacer,orange filled circle for Nb and Cu as underlayers with Cu(20nm as spacer, blue filled star for Nb as underlayer with Cu(20nm) as spacer, filled triangle for Nb as underlayer with Ag(20nm) as spacer, green filled rhombus for Nb, Cu and Ag as underlayers with Ag(20nm) as spacer,and blue filled square for Nb and Ag as underlayers and Cu(20nm) as spacer.

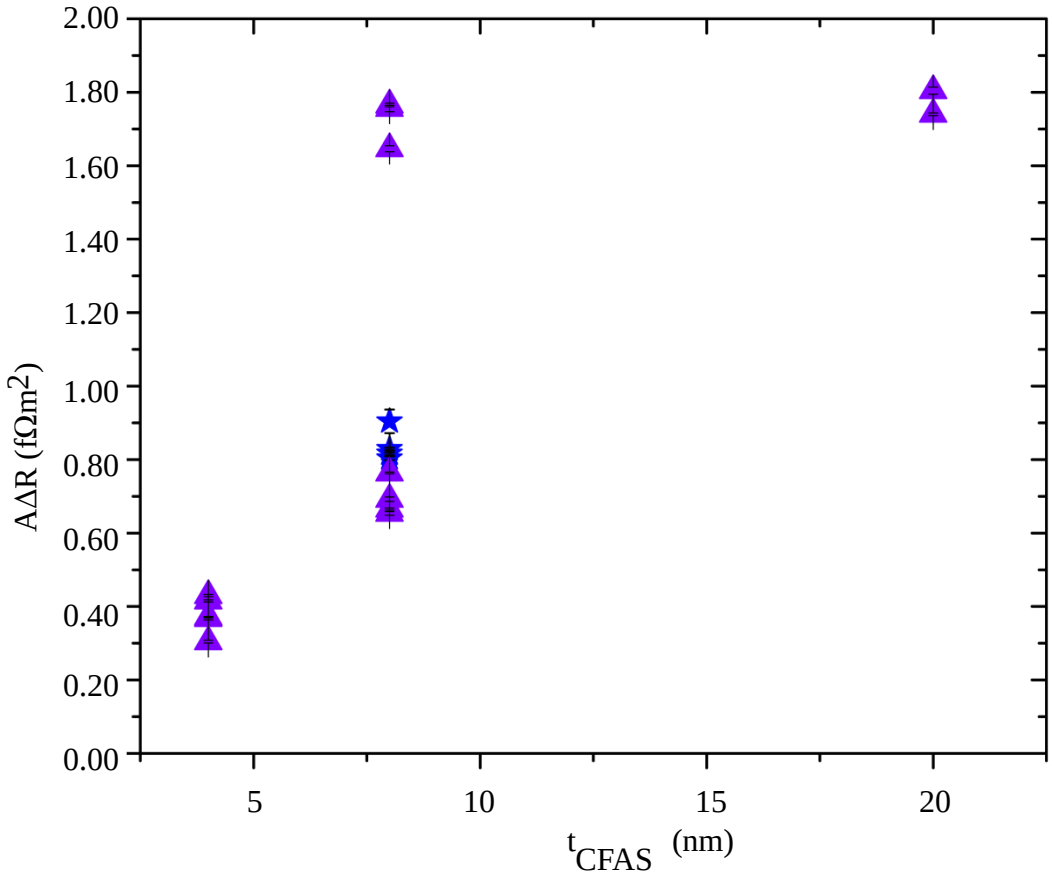

Figure 6.16: AΔR versus t_{CFAS} for spin valves grown with Nb as the underlayer and with The difference in AΔR for Ag and Cu spacer layers between CFAS and Py, is insignificant. The different symbols represent the following structures; blue filled star for blue filled star for Nb as underlayer with Cu(20nm) as spacer and filled triangle for Nb as underlayer with Ag(20nm) as spacer.

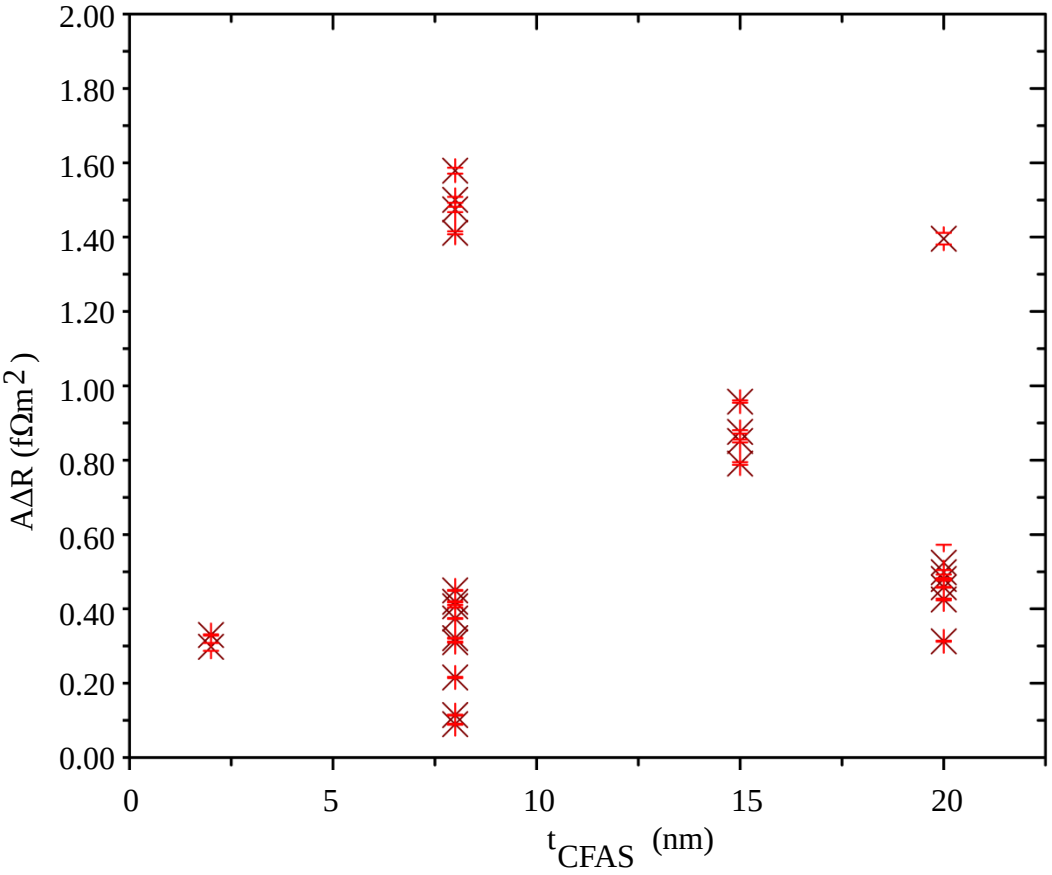

Figure 6.17: AΔR versus t_{CFAS} for spin valves grown with Nb/Cu as the underlayer. The sample structure is Nb and Cu as underlayers and Cu(25nm) as spacer.

2) The sputter process is also limited by the waiting period between the CFAS and the spacer layer growth, due to either contamination from a long wait, or interdiffusion for a short wait.

3) The composition of our films does not follow the exact stoichiometry of the $Co_2Fe(Al\ Si)_{0.5}$ alloy because of the differences in sputtering rates of the different components of the alloy.

4) Sharp MR peak maxima make the nature of our AP state ambiguous. Our $A\Delta R$ is thus probably only a lower bound on the true AP state.

Topics to pursue in the future include:

1) Quantitative analysis of the fraction of single crystal CFAS using the recipes described in this thesis.

2) Alternative ways to obtain a well defined AP state.

3) Determining the effect of interface roughness on $A\Delta R$ for CFAS spin valves.

Chapter 7

Summary

This thesis involves experiments to produce new information from three projects concerning Current Perpendicular to Plane Magnetoresistance (CPP MR): 1) Measuring the Specific Resistance of Ir/Pd interfaces and comparing the result with no-free-parameter calculations; 2) Studies of Spin Flipping in the antiferromagnets IrMn and FeMn and at IrMn/Cu and FeMn/Cu interfaces; and 3) Studies with the Half metallic Heusler alloy Co_2Fe (Al Si)$_{0.5}$ (CFAS).

1) Specific Interface Resistance of Ir/Pd.

Previous studies of lattice matched (nearly identical lattice parameter $\Delta a/a_0 \leq 1\%$ and same crystal structures) metallic pairs, showed agreement between experimental values of 2AR and calculated values with the real band structures and no-free-parameters. For metal pairs with $\Delta a/a_0 \sim 5\% - 10\%$, the experiments and calculations no longer agreed. We chose Ir/Pd with $\Delta a/a_0 \geq 1\% = 1.3\%$ as an intermediate pair to further test the techniques that gave agreement for metal pairs with $\Delta a/a_0 \leq 1\%$. Our double blind study gave agreement

between our experimental value and the calculated value for $2AR_{Ir/Pd}$ with improved band structures, for both perfectly flat and disordered/intermixed (50%-50% of 2ML thick alloy of Ir/Pd) interfaces.

The agreement between the two different interfaces is attributed to the balancing of two factors upon introduction of disorder: (a) a rise in interface resistance due to increased scattering in the disordered interfaces; and (b) a decrease in interface resistance due to additional scattering states available for conduction when the constraint of $\mathbf{k}_{||}$ conservation is removed.

Adding in our results now gives five examples of agreement between measured values of 2AR for lattice matched pairs, and ones calculated with no adjustable parameters. The last two examples, Pt/Pd and Pd/Ir, were both done double-blind. Together these results suggest that the basic physics underlying AR is reasonably well understood.

2) Antiferromagnetic Spin Flipping studies:

Motivated by the desire to obtain experimental information about the spin flipping in the antiferromagnets (AF) IrMn and FeMn, and at their interfaces with Cu, we studied the decay of $A\Delta R$ with the introduction of the desired AF into the middle of the central Cu layer of Py based Exchange Biased Spin Valves (EBSVs). A previous study of the AF FeMn, with FeMn insert thickness up to 2nm by Park et al in 2002, found strong spin flipping at the interface with Cu and a hint of possible weaker spin flipping in the bulk. The inability to establish the nature of bulk behavior was due to signals at 2nm thickness being only comparable to their uncertainties.

Our initial study of IrMn inserts up to a thickness of 5nm, showed similarly strong spin flipping at the IrMn/Cu interfaces and what seemed to be a longer spin diffusion length in

the bulk. However, uncertainties in both the choice of interface thickness, and the data in the bulk, did not let us distinguish between Valet Fert fits with ${\ell_{sf}}^{IrMn} = 5$nm or ∞. When we extended the insert thickness beyond 5nm, we expected a further decay in AΔR due to spin flipping. Instead, for thicknesses between 5 and 30nm of IrMn, AΔR became constant at about 0.003 ± 0.001 fΩm^2. Further tests revealed that this unexpected behavior is a field dependence in the resistance of Py, probably akin to Anisotropic Magnetoresistance in Py. Attempts to reduce spin flipping at the IrMn/Cu interface by introducing Nb and Ru between IrMn and Cu showed no systematic change in AΔR. An extension of the prior study of FeMn to thicker FeMn layers, also revealed a constant AΔR.

We conclude that: (a) spin flipping at both IrMn/Cu and FeMn/Cu interfaces is strong; (b) we have discovered a small constant term in AΔR which we attribute to a new magnetoresistance of Py; and (c) given the uncertainties in the choice of interface thickness,t$_I$, and in the value of the constant, we cannot put a tight bound on ℓ_{sf} for either bulk IrMn and FeMn. However it is probably short, of the order of 1nm or less.

3) CPP-MR studies of CFAS Half Metallic Heusler Alloy:

Half metallic ferromagnets have a metallic band structure for majority elecrons and a semiconducting/insulating band structure for minority electrons. This unique property should produce a large spin-scattering asymmetry that is desirable for enhancing the CPP MR. The motivation for us to grow such a half metallic alloy came from very high Tunnel Magnetoresistance (TMR) signals observed by Tezuka et al in 2008 with epitaxial CFAS Heusler alloys, which have been shown theoretically to be half metallic. They were able to obtain epitaxial CFAS by sputtering at room temperature and then annealing at high temperature after deposition. We expected to be able to grow epitaxial CFAS directly using

our high temperature sputtering facility. In 2010 Nakatani et al published bulk and interfacial studies of CFAS using nanopillar CPP MR spin valves of Ag/CFAS/Ag/CFAS/Ag also sputtered at room temperature and subsequently annealed. At 14K, they obtained a high MR=80%.

We attempted to grow a CFAS/N/Py hybrid spin valve (N=Cu or Ag) expecting to obtain a well defined AP state due to the low coercivity of Py compared to that of CFAS. We were constrained to sandwich our spin valves between Nb electrodes that would become superconducting at 4.2K (measurement temperature), thereby removing any lead resistance from bulk Nb. Our process was simpler than the Nakatani et al sample since Py was not required to grow epitaxially. Using Valet Fert theory for CFAS with Nakatani's properties and for Py with our previously determined properties, we estimated $A\Delta R \sim 4.5 f\Omega m^2$. We checked this procedure by calculating $A\Delta R$ for Nakatani's samples, obtaining 15 $f\Omega m^2$, close to their experimental value of 16 $f\Omega m^2$. In practice, our largest values of $A\Delta R$ were $\sim$ 1.8 $f\Omega m^2$, about 40% of the expected. Possible reasons for this lower value include: (a) our apparent AP state is lower than the correct AP state, both because the AR hysteresis peaks are too sharp (See Figures 6.13, 6.14, B.2, and B.3) and because of complications associated with the transition behavior in magnetization at H $\sim$ 100 Oe shown in Figure B.1; (b) our CFAS layers are not perfect B2, but rather a mix of B2 and more disordered states such as A2 or even partly polycrystalline, which are not half metallic; and (c) our CFAS layers are also disordered due to non-stoichiometry produced by imperfect sputtering.

Appendices

Appendix A

Study of outliers in measurement

In some of our samples, one or two out of the 600 data points were classified as outliers, and not included in the final calculations. To justify this exclusion, we checked the raw data sweep for each sample. Figure A.1 shows the raw data for one such sample with (a) all the data included, and (b)the outlier removed. Omitting the outlier, the spread of data in these plots is about 0.04 $f\Omega\text{m}^2$. We took the difference of the outlier from the average of the data for the field at which it occurred. Table A.1 lists all of the samples for which such outliers were removed. It lists the difference, d=(Value of Outlier)-(Mean of the Resistances for that field). If we divide each d by the Standard Deviation (σ) for that sample at that field, we get n. In a Guassian distribution curve, nearly 99.99% of data are included within 5σ. We can see that the outliers are present at much larger multiples of σ.

If we assume that d_{Min}=0.15 nΩ is the smallest flux jump in the SQUID in our measuring circuit, then all other outliers should be flux jumps of higher orders. If we divide the rest of the d by $\text{d}_{Min.}$ and round to the nearest integer, m, then the set of all the

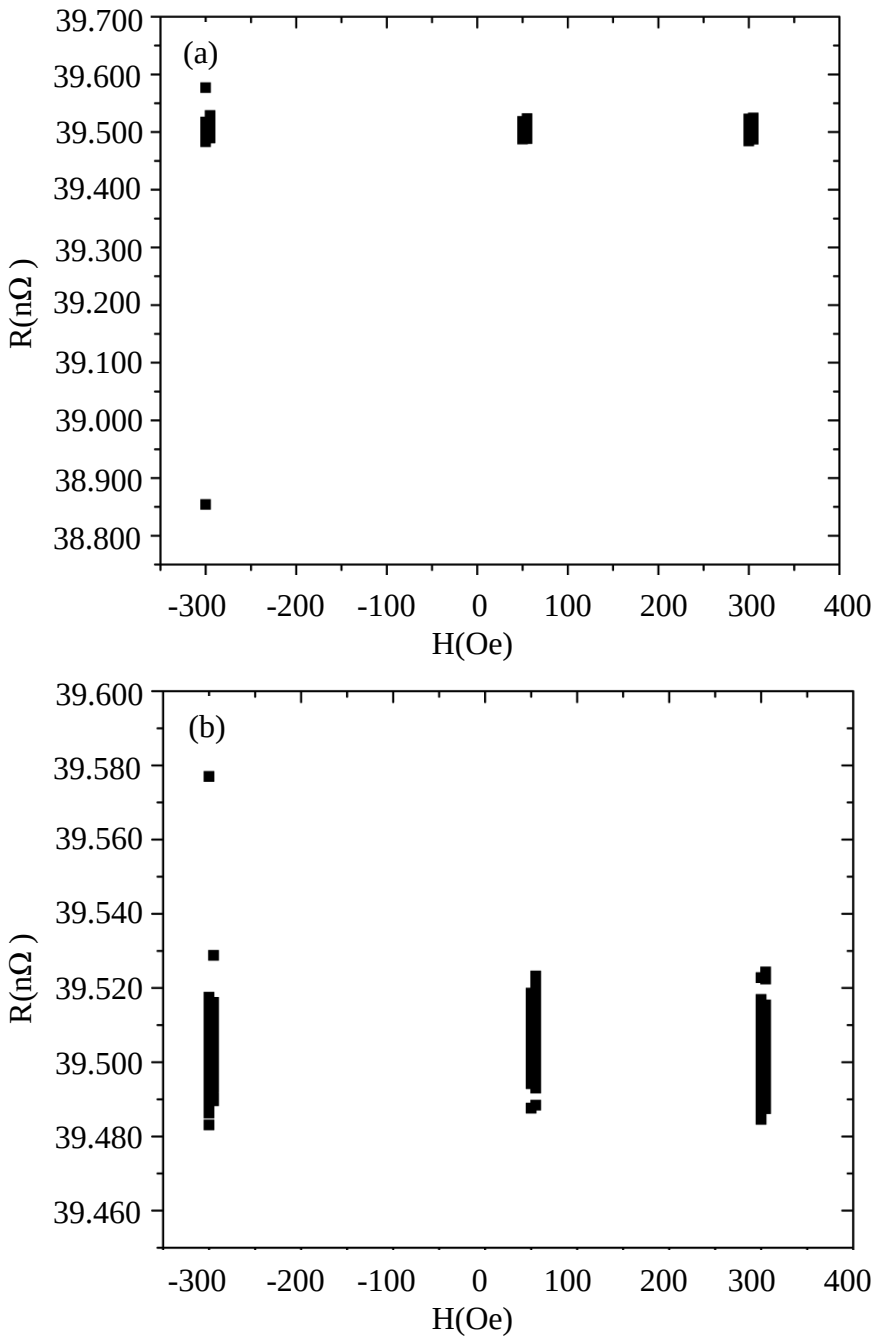

Figure A.1: Raw data for a 30nm Sample # 1937-4 (a) with outlier (b) without outlier

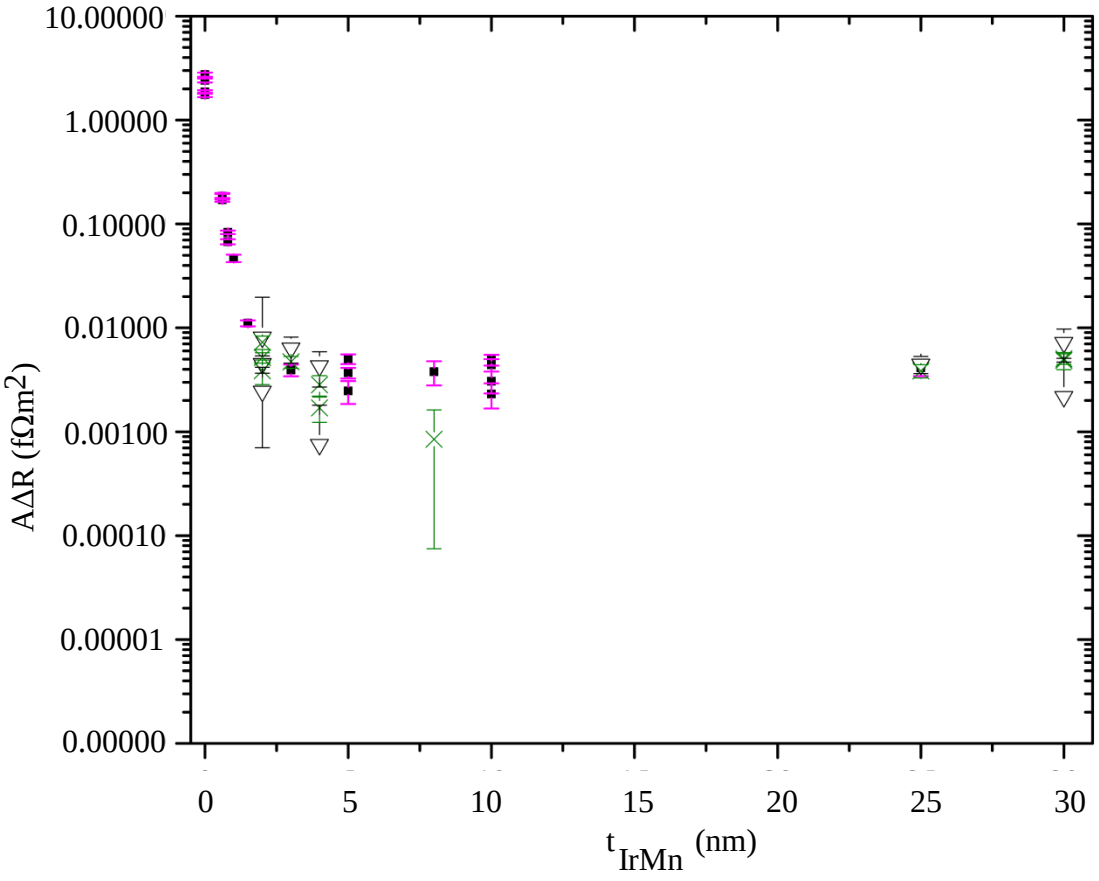

Figure A.2: AΔR versus t_{IrMn}. Filled squares show data with no outliers present during measurement. t_{IrMn}≤1nm show data with single measurements at every field and 1.5nm≤t_{IrMn}≤30nm show data with 2X100 measurements at the chosen fields for P measurements at H (-150 Oe, -200 Oe or -300 Oe) and +H (+300 Oe) fields and AP at +50 Oe. Open triangles show data for $t_{IrMn} \geq$ 1nm with the outliers present. Crosses show data for $t_{IrMn} \geq$ 1nm with the outliers removed.

Sample	t_{IrMn} (nm)	Field (Oe)	(Outlier-Mean) (nΩ)=d	n=d/σ	m=d/0.15 (Rounded)
1811-5	2	-150	0.42	42	3
1811-7	3	-150	0.49	49	3
1812-7	2	-150	0.19	48	1
1828-4	4	-150	0.28	93	2
1919-2	4	-200	0.49	49	3
1919-3	8	-200	0.15	15	1
1919-8	8	-200	0.46	46	3
1936-3	2(#1 Outlier)	-300	2.58	86	17
1936-3	2(#2 Outlier)	-300	2.85	95	19
1936-4	25	-300	0.17	17	1
1937-4	30	-300	0.65	65	4
1937-1	30	300	0.93	93	6

Table A.1: Lists the samples with outliers that were eliminated. The third column represents the field at which the outlier occurred. All except two outliers occurred during the first magnetic field sweep. For 1919-2, it occurred at -200 Oe of the second field sweep while for 1937-1, it occurred at the end of the second field sweep. The fourth column shows the difference in the value of the outlier from the average of the rest of resistances for that particular field. The fifth column shows the value of n, the number of standard deviations away from the average, at which the outlier occurs. Finally the last column gives the rounded value of m assuming the smallest flux jump to be h=0.15nΩ.

differences can be approximated as md_{Min}.

Finally Figure A.2 shows a plot of $A\Delta R$ versus t_{IrMn} with crosses representing the signal calculated by removing the outliers and triangles representing the same signal including the outliers. Data, with no outliers, are shown by filled squares. Interestingly, the error bars are large enough that the data with outliers overlap the corresponding data without outliers. Hence removing the outliers does not qualitatively change our data.

Appendix B

Magnetizations and Resistances for two chips:(a)Nb/CFAS/Ag/Py and (b)Nb/Cu/Ag/CFAS/Ag/Py

Figure B.1 compares magnetizations for cases(a) Chip 2066-2 and (b) Chip 2066-4. Both cases show a rapid change below 100 Oe for Py and the slower change up to 700-800 Oe for CFAS. Both also show an unexpected transitional structure in the vicinity of 100 Oe. The source of this transition is not known, but it might represent a part of the CFAS that is single crystal. Its occurrence in the field region of the maxima in AR (See Figures B.2-B.3) enhances the possibility that this maximum does not represent a true AP state. The general similarities of AR(AP) and AΔR for all of the pillars in Figure B.2-B.4 suggest that the average values of AΔR$\sim$ 1.7-1.8 fΩm^2 most likely represent reproducible properties of these chips and pillars, rather than accidents. If so, why these values are only $\sim$40% of that

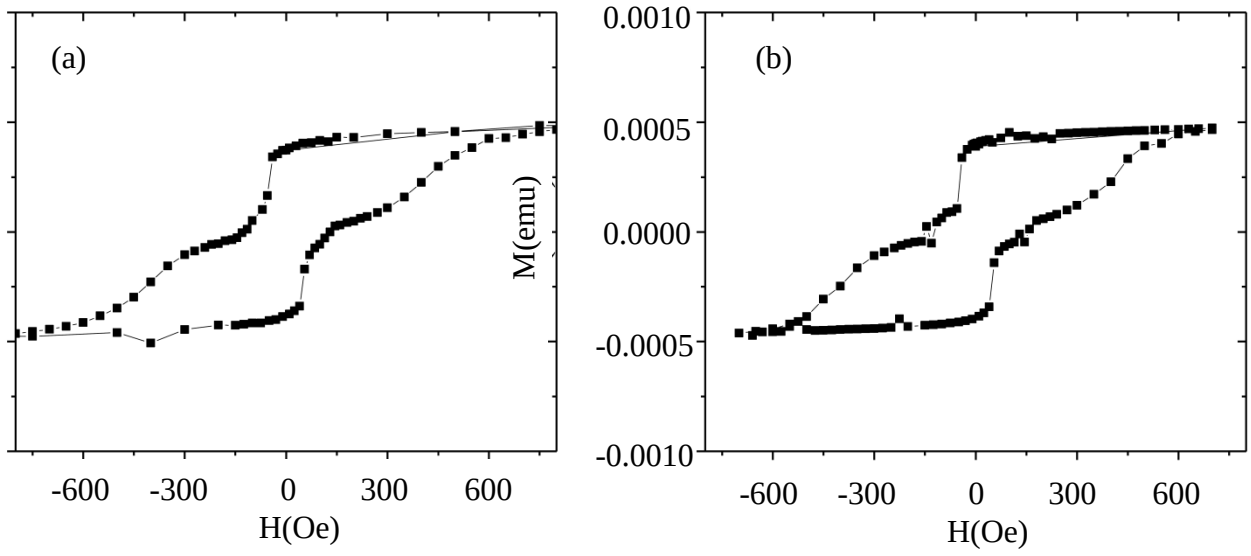

Figure B.1: Magnetization curves of two chips, that showed MR signals, with multilayers (a) Chip 2066-2 (CFAS=20nm) with Nb,Cu, and Ag as underlayers and Ag(20nm)as spacer between CFAS and Py(24nm), and (b) Chip 2066-4 (CFAS=20nm) with Nb as underlayer and Ag(20nm) as spacer between CFAS and Py(24nm). We see separate steps for Py and CFAS. However we also see an unexpected transition state, the source of which is not clear.

expected from the parameters of Nakatani et al remains to be determined.

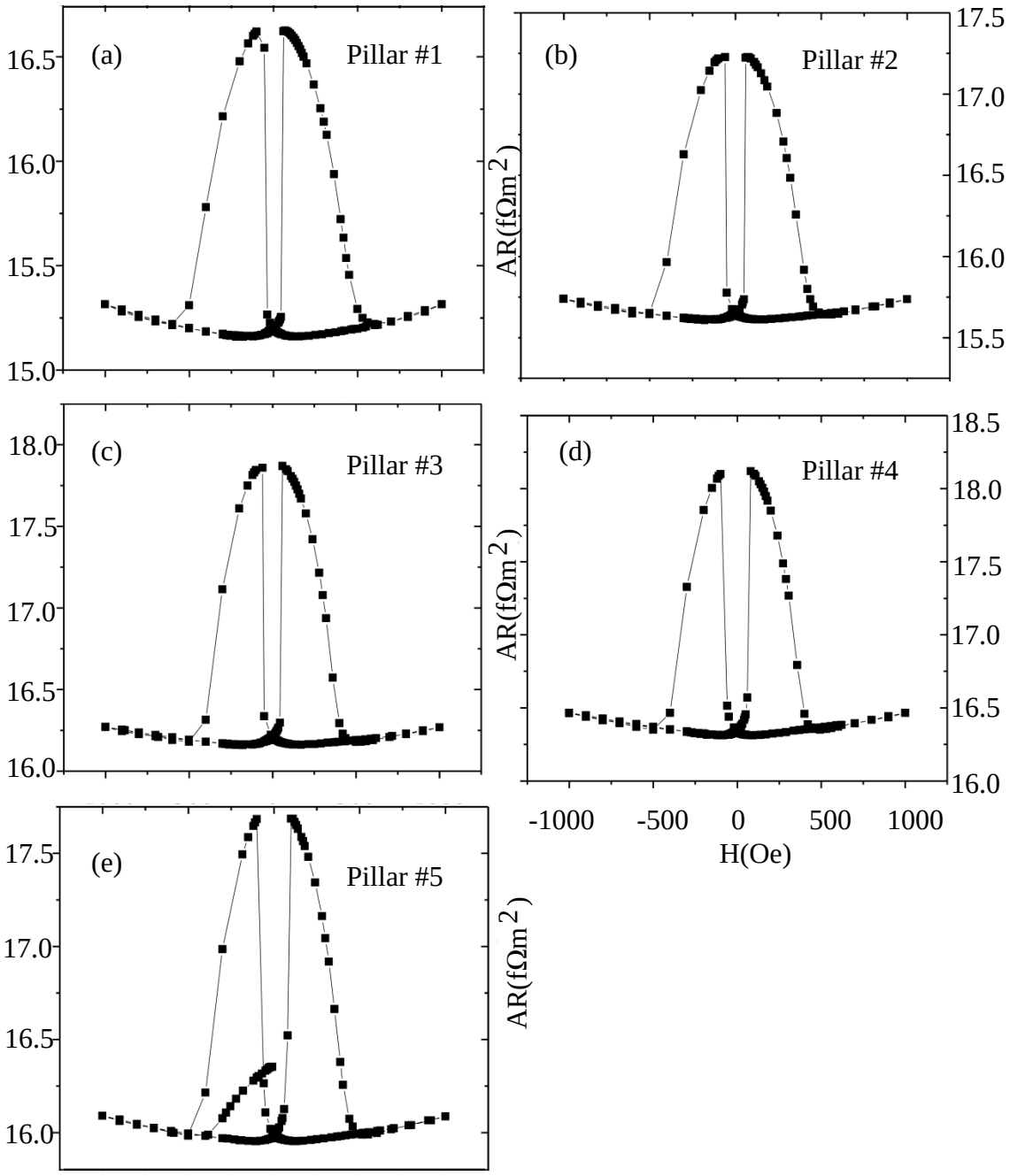

Figure B.2: (a)–(e) show the AR curves of pillars that showed signals on Chip 2066-2 (CFAS=20nm) with multilayer structure of Nb, Cu, and Ag as underlayers and Ag(20nm) as spacer. The values of AR and AΔR of each pillar on the chip are similar to each other.

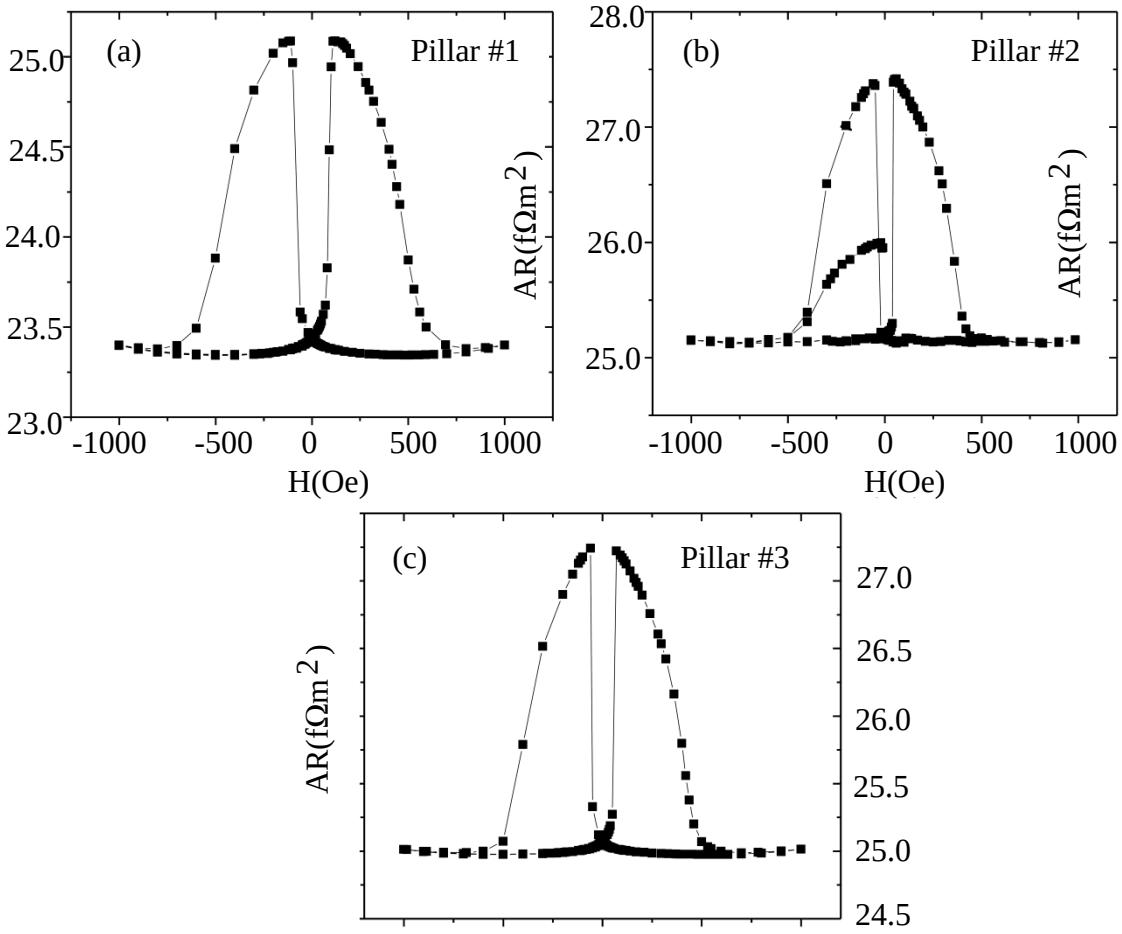

Figure B.3: (a)–(c) show the AR curves of pillars that showed signals on Chip 2066-4(CFAS=20nm) with multilayer structure Nb as underlayer and Ag(20nm) as spacer. The values of AR and AΔR of each pillar on the chip are similar to each other.

Bibliography

Bibliography

[1] S.Maekawa and T.Shinjo, *Spin Dependent Transport in Magnetic Nanostructures*,Advances in Condensed Matter Science, Vol. 3 (2002).

[2] M. N. Baibich, J. M. Broto, A.Fert, F. N. V. Dau, and F. Petroff, Phys. Rev. Lett. **61**, 2472 (1988).

[3] G. Binasch, P. Grunberg, F. Saurenbach, and W. Zinn, Phys. Rev. B **39**, 4828 (1989).

[4] S.Zhang and P.M.Levy,J. Appl. Phys. **69**,4786 (1991).

[5] W. P. Pratt, Jr., S. F. Lee, J. M. Slaughter, R. Loloee, P. A. Schroeder, and J. Bass, Phys. Rev. Lett. **66**, 3060 (1991).

[6] E. Tsymbal and D. Pettifor,in *Solid State Physics*(Academic Press, San Diego,2001),Vol. 56,p.113.

[7] I.Žutić,J.Fabian and S. Das Sarma,Reviews of Modern Physics,Vol **76** (2004).

[8] http://www.magnet.fsu.edu/education/tutorials/magnetacademy/gmr/

[9] http://www.research.ibm.com/research/gmr.html.

[10] T.Kasuya, and A. Yanase,Rev. Mod. Phys. **40**,684 (1968).

[11] E.L.Nagaev, *Physics of Magnetic Semiconductors*(Mir,Moscow)(1983).

[12] L.Esaki, P. Stiles and S. von Molnár,Phys. Rev.Lett. **19**, 852(1967)

[13] R. Meservey,D. Paraskevopoulos and P. M. Tedrow, Phys.Rev. Lett. **37**, 858 (1976)

[14] M.Julliére, Phys. Lett. 54A, 225 (1975)

[15] J. S. Moodera *et al.* Phys. Rev. Lett. **74**,3273 (1995)

[16] Husseyin Kurt, PhD Thesis, Michigan State University (2004)

[17] R.Wood,J. Magn. Magn. Mater. **321**, 555 (2009).

[18] L. Berger, Phys. Rev. B 54, 9353 (1996).

[19] J. C. Slonczewski *et al.*, J. Magn. Magn. Mater. **159**, L1 (1996).

[20] M. Tsoi, A. G. M. Jensen, J. Bass, W. C. Chiang, M. Seck, V. Tsoi, and P. Wyder, Phys. Rev. Lett. **80**, 4281 (1998).

[21] D.C.Ralph and M.D.Stiles,J. Magn. Magn. Mater. **320**, 1190 (2008).

[22] N. W. Ashcroft and N. D. Mermin, Solid State Physics (Harcourt Brace College Publishers, Fort Worth, 1976).

[23] Mizutani and Uchiro, Introduction to Electron theory of Metals (2001)

[24] N. F. Mott, Proceedings of the Royal Society of London. Series A, Mathematical and Physical Sciences 153, 699 (1936).

[25] I. A. Campbell and A. Fert, in Ferromagnetic Materials, edited by E. P. Wolfarth (North-Holland, Amsterdam, 1982), Vol. 3, p. 747.

[26] Amit Sharma, PhD Thesis, Michigan State University (2008).

[27] T. Valet and A. Fert, Phys. Rev. B **48**, 7099 (1993).

[28] C. Fierz, S. F. Lee, J. Bass, W. P. Pratt, and P. A. Schroeder, J. Phys.: Condensed Matter **2**, 9701 (1990).

[29] J. M. Slaughter, W. P. Pratt, Jr., and P. A. Schroeder, Rev. Sci. Instrum. **60**, 127 (1989).

[30] S. F. Lee, Q. Yang, P. Holody, R. Loloee, J. H. Hetherington, S. Mahmood, B.Ikegami, K. Vigen, L. L. Henry, P. A. Schroeder, W. P. Pratt, Jr., and J. Bass,Phys. Rev. B **52**, 15426 (1995).

[31] A. Fert and L. Piraux, J. Magn. Magn. Mater. **200**, 338 (1999).

[32] A. Blondel, B. Doudin, J.P. Ansermet, J. Magn. Magn. Mater. **165** (1997) 34.

[33] J. Bass and W. P. Pratt,Jr., J. Phys.: Condensed Matter **19**, 183201 (2007).

[34] S. S. P. Parkin, N. More, and K. P. Roche, Phys. Rev. Lett. **64**, 2304 (1990).

[35] S. S. P. Parkin, R. Bhadra, and K. P. Roche, Phys. Rev. Lett. **66**, 2152 (1991).

[36] B. Dieny, V. S. Speriosu, S. Metin, S. S. P. Parkin, B. A. Gurney, P. Baumgart, and D. R. Wilhoit, J. Appl. Phys. **69**, 4774 (1991).

[37] A. Chaiken, P. Lubitz, J. J. Krebs, G. A. Prinz, and M. Z. Harford, Appl. Phys. Lett. **59**, 240 (1991).

[38] K.Eid,D.Portner,J.A.Borchers,R.Loloee,M.Al Haj Darwish,M.Tsoi,R.D.Slater,K.V.O $'$Donovan,H.Kurt,W.P.Pratt,Jr. and J. Bass,Phys. Rev. B **65**, 054424(2002).

[39] W. H. Meiklejohn and C. P. Bean, Phys. Rev. **102**, 1413 (1956).

[40] H.Y.T. Nguyen,R. Acharyya, W.P. Pratt Jr., and J. Bass. Conduction Electron Spin-Flipping at Sputtered Co(90)Fe(10)/Cu Interfaces. In Press, J. Appl. Phys. (2011)

[41] B.Dassonneville,R.Acharyya,H.Y.T.Nguyen,R. Loloee, W.P. Pratt Jr.and J.Bass, Appl. Phys. Lett. **96**, 022509 (2010).

[42] H.Y.T. Nguyen, R. Acharyya, E. Huey, B. Richard, R. Loloee, W.P. Pratt Jr.,and J.Bass, Phys. Rev. B **82**, 220401 (2010).

[43] A. Sharma, N. Theodoropoulou, T. Haillard,R. Acharyya, R. Loloee, W. P. Pratt, Jr., and J. Bass.J. Zhang and M. A. Crimp, Phys.Rev. B **77**, 224438 (2008).

[44] D.K.Kim,Y.S.Lee,H.Y.T.Nguyen,R.Acharyya,R.Loloee,K.H.Shin,Y.K.Kim,B.C.Min,W.P.Pratt Jr. and J.Bass,IEEE Trans. on Magn. Vol.**46**, 1374 (2010).

[45] B. Dassonneville,H.Y.T. Nguyen,R. Acharyya, R. Loloee, W.P. Pratt Jr. and J. Bass, IEEE Trans. on Magn. Vol. **46**, 1405 (2010).

[46] M.A.M.Gijs and G.E.Bauer,Adv. in Phys. **46**,285 (1997).

[47] P. M. Levy, in Solid State Physics, edited by H. Ehrenreich and D. Turnbull (Academic Press, Cambridge MA, 1994), Vol. 47, Chap. Giant magnetoresis- tance in magnetic layered and granular materials, pp. 367-462.

[48] S.K.J.Lenczowski,PhD Thesis,Eindhoven University of Technology (1995).

[49] S. F. Lee, W. P. Pratt, Jr., Q. Yang, P. Holody, R. Loloee, P. A. Schroeder, and J. Bass, J. Magn. Magn. Mater. **118**, L1 (1993).

[50] Q.Yang,P.Holody,S.F.Lee,L.L.Henry,R.Loloee,P.A.Schroeder,W.P.Pratt,Jr.and J.Bass,Phys. Rev. Lett.**72**,3274(1994).

[51] J.Bass,P.A.Schroeder,W.P.Pratt,Jr.,S.F.Lee,Q.Yang,P.Holody,L.L.Henry and R.Loloee, Mater. Sci. Eng.B **31**,77(1995).

[52] L.Piraux,S.Dubois,A.Fert and L.Belliard,Eur. Phys. J. B **4**,413(1998).

[53] F.J.Jedema,A.T.Filip and B.J. van Wees,Nature **410**,345(2001).

[54] F.J.Jedema,M.S.Nijboer,A.T.Filip and B.J.van Wees,Phys. Rev. B **67**,085319(2003).

[55] P.C. Van Son, H. Van Kempen and P. Wyder, Phys. Rev. Lett. **58**, 2271 (1987).

[56] M.Johnson and R.H.Silsbee, Phys. Rev.B **35**,4959(1987).

[57] M.Johnson and R.H.Silsbee,Phys. Rev. Lett. **60**, 377(1988).

[58] D.R.Penn and M.D.Stiles,Phys. Rev. B **72**, 212410 (2005).

[59] J.Bass and W.P.Pratt Jr.,J. Magn. Magn. Mat. **200**, 274 (1999).

[60] R.Acharyya,H.Y.T.Nguyen,R.Loloee,W.P.Pratt,Jr., J.Bass,S.Wang and K.Xia, Appl. Phys. Lett. **94**,02212(2009).

[61] Q. Yang,*et al.*, Phys. Rev. B **51**, 3226(1995).

[62] S. K. Olson, R. Loloee, N. Theodoropoulou, W.P. Pratt Jr., J. Bass, P.X. Xu, and K. Xia, Appl. Phys. Lett. 87, 252508 (2005).

[63] W.Park,D.V.Baxter,S.Steenwyk,I.Moraru,W.P.Pratt,Jr. and J.Bass, Phys. Rev. B **62**, 1178 (2000).

[64] L.L. Henry, *et al.*, Phys. Rev. B **54**, 12336 (1996).

[65] N.J.List, *et al.*, J. Magn. Magn. Mat. **148**, 342 (1995).

[66] L.Piraux, *et al.*, J. Magn. Magn. Mt. **156**, 317 (1996)

[67] B. Doudin, *et al.*, J. Appl. Phys. **79**, 6090 (1996).

[68] A.Zambano, *et al.*, J. Magn. Magn. Mat. **253**, 51 (2002).

[69] H.Kurt,*et al.*, Appl. Phys. Lett. **81**, 4787 (2002).

[70] C.Galinon,*et al.*, Appl. Phys. Lett. **86**, 182502 (2005).

[71] N. Theodoropoulou,*et al.*, J. Appl. Phys. **99**, 08G502 (2006).

[72] N. Theodoropoulou,*et al.*, IEEE Trans. On Magn. **43**, 2860 (2007).

[73] A. Sharma,*et al.*, J. Appl. Phys. **102**, 113916 (2007).

[74] K.M. Schep,*et al.*, Phys. Rev. B **56**, 10805 (1997).

[75] G.E.W. Bauer,*et al.*, J. Phys. D. **35**, 2410 (2002).

[76] M.D. Stiles and D.R. Penn, Phys. Rev. B **61**, 3200 (2000).

[77] P. X. Xu, K. Xia, M. Zwierzycki, M. Talanana, and P. J. Kelly, Phys. Rev.Lett. **96**, 176602 (2006).

[78] K. Xia, P. J. Kelly, G. E. W. Bauer, I. Turek, J. Kudrnovsky, and V. Drchal, Phys. Rev. B **63**, 064407 (2001).

[79] K. Xia, M. Zwierzycki, M. Talanana, and P. J. Kelly, Phys. Rev. B **73**, 064420 (2006).

[80] Mazin Khashnaweh, PhD Thesis,Michigan State University (2010).

[81] Trupti Khaire,PhD Thesis,Michigan State University(2010).

[82] Reza Loloee,PhD Thesis,Michigan State University (2002).

[83] D. M. Edmunds, W. P. Pratt, Jr., and J. A. Rowlands,Rev. Sci.Inst., Vol. **51**, 1516(1980).

[84] L. J. van der Pauw, Philips Tech. Rev. **20**, 220 (1958).

[85] J. Bass, in Metals: Electronic Transport Phenomena, Vol. 15a of Landolt- Bornstein New Series Group III, edited by K. H. Hellwege and J. L. Olsen (Springer, Berlin, 1982).

[86] W. P. Pratt, Jr., S. D. Steenwyk, S. Y. Hsu, W.-C. Chiang, A. C. Schaefer, R. Loloee, and J. Bass, IEEE Trans. Magn. **33**, 3505 (1997).

[87] S. Steenwyk,*et al.*, J. Magn. Magn. Mater. **170**, L1 (1997).

[88] P.X.Xu and K.Xia, Phys. Rev. B **74**, 184206 (2006).

[89] *Constitution of Binary Alloys*, 2nd ed., edited by M. Hanson (McGraw hill, New York, 1958), p. 585.

[90] K. Schroeder, *Handbook of Electrical Resistivities of Binary Metallic Alloys* (CRC, Boca Raton, FL, 1983).

[91] O.K. Anderson,*et al.*, Phys. Rev. B **2**, 883 (1970).

[92] R. Acharyya, H.Y.T. Nguyen, W.P. Pratt Jr., and J. Bass,IEEE Trans. On Magn. Vol. **46**, No. 6 (2010).

[93] R. Acharyya, H.Y.T. Nguyen, W.P. Pratt Jr., and J. Bass, J. of Appl. Phys. **109**, 07C503 (2011).

[94] Z. Wei, A. Sharma, A. S. Nunez, P. M. Haney, R. A. Duine, J. Bass, A. H. MacDonald, and M. Tsoi, Phys. Rev. Lett. **98**, 116603 (2007).

[95] S. Urazhdin and N. Anthony, Phys. Rev. Lett. **99**, 046602 (2007).

[96] A.S. Nunez, R.A. Duine, P. Haney, and A.H. MacDonald, Phys.Rev. B **73**, 214426 (2006).

[97] A.H.MacDonald and M.Tsoi, *Phil. Trans. R. Soc. A*, **369**,3098-3114 (2011).

[98] K.H. Fischer, *Kondo and Spin Fluctuation Systems, Spin Glasses*, Landolt-Bornstein Tables, New Series, Gruppe III, Vol. 15a, Pg. 289, K.H. Hellwege and J.L. Olsen, Eds., Springer-Verlag, Berlin (1982).

[99] I.Galanakis and P.H.Dederichs, *Half-Metallic Alloys*, Lect. Notes Phys. 676 ,Springer, Berlin Heidelberg (2005).

[100] R.A.de Groot, H.M.Mueller, P.G.van Engen, and K.H.J.Buschow, Phys. Rev. Lett. **50**, 2024 (1983).

[101] N.Tezuka,N.Ikeda,N.Sugimoto,and K.Inomata, App. Phys. Lett. **89**, 112514 (2006).

[102] T.M.Nakatani,T.Furubayashi,S.Kasai,H.Sukegawa,Y.K.Takahashi,S.Mitani, and K.Hono, App. Phys. Lett. **96**, 212501 (2010).

[103] Y.Kota and A.Sakuma,Journal of Physics, Conference Series **266** 012094 (2011).

[104] G.H.Fecher and C.Felser, J. Phys. D Appl. Phys. **40**, 1582 (2007).

[105] T.M.Nakatani, T.Furubayashi, and K.Hono, J.Appl. Phys. **109**, 07B724 (2011).

[106] T.Taniguchi, H.Imamura,T.M.Nakatani, and K.Hono, Appl. Phys. Lett. **98**, 042503 (2011).